SOLVING ADVANCED MICROMACHINING PROBLEMS FOR ULTRA-RAPID AND ULTRA-HIGH RESOLUTION ON-CHIP LIQUID CHROMATOGRAPHY

WIM DE MALSCHE

Committee members Twente University

Prof. dr. ing. Matthias Wessling	(Chairman)	University of Twente
Prof. dr. Han Gardeniers	(Promotor)	University of Twente
Prof. dr. ir. Gert Desmet	(Co-promotor)	Vrije Universiteit Brussel
Prof. dr. Frieder Mugele		University of Twente
Prof. dr. Miko C. Elwenspoek		University of Twente
Prof. dr. ir. Albert van den Berg		University of Twente
Prof. dr. Sabeth M.J. Verpoorte		University of Groningen
Prof. dr. Jörg. P. Kutter		Technical University of Denmark

Dit proefschrift is goedgekeurd door de promotoren:

Prof. dr. J.G.E. Gardeniers

Prof. dr. ir. G. Desmet

SOLVING ADVANCED MICROMACHINING PROBLEMS FOR ULTRA-RAPID AND
ULTRA-HIGH RESOLUTION ON-CHIP LIQUID CHROMATOGRAPHY

DISSERTATION

to obtain
the degree of doctor at the University of Twente,
on the authority of the rector magnificus,
prof. dr. W.H.M. Zijm,
on account of the decision of the graduation committee,
to be publicly defended
on Friday the 30th of May 2008 at 13.15

by

Wim De Malsche

born on the 14th of September 1978

in Hamme, Belgium

This dissertation has been defended in private at the Vrije Universiteit Brussel at April 15th 2008 and has been approved by a Promotion Committee appointed by the Vrije Universiteit Brussel.

Committee Members Vrije Universiteit Brussel

Prof. dr. R. Willem	(Chairman)	Vrije Universiteit Brussel
Prof. dr. ir. R. Pintelon	(Co-chairman)	Vrije Universiteit Brussel
Prof. dr. ir. H. Verelst	(Secretary)	Vrije Universiteit Brussel
Prof. dr. ir. G. Desmet	(Promotor)	Vrije Universiteit Brussel
Prof. dr. J.G.E Gardeniers	(Promotor)	University of Twente
dr. D. Mangelings		Vrije Universiteit Brussel
Prof. dr. E.M.J. Verpoorte		University of Groningen
Prof. dr. J.P. Kutter		Technical University of Denmark

Promotors

Prof. dr. J.G.E. Gardeniers
Mesoscale Chemical Systems (TNW)
Twente University
Enschede
The Netherlands

Prof. dr. ir. Gert Desmet
Department of Chemical Engineering (CHIS)
Vrije Universiteit Brussel
Brussels
Belgium

Voor Sofie

Chapter 1: Introduction

1.1 Project aim

Liquid chromatography (LC) is perhaps the most widespread and universal analytical separation tool, indispensable in environmental monitoring, clinical diagnostics, food quality and safety inspection, biological and pharmaceutical research, the chemical process industry,… and constituting worldwide a multi-billion Euro economy.

In high-performance liquid chromatography, the science and art of packing columns has known an intense development during the last decades. It seems however that the packing and coating procedures have been fully optimized and that the chromatographic performance in this system is reaching a steady level because the fundamental and theoretical limits are approached. Because the separation power of the currently available LC columns is no longer sufficient to solve the timely separation problems of the industries and research institutes involved in drug discovery, proteomics research and clinical diagnostics, a transition towards new materials and completely new formats is natural.

It is known for many years that packing homogeneity is a very important parameter to increase the separation power of a given chromatographic system.[1] In 1998 Fred Regnier introduced and validated the concept of 'collocated monolithic support structures' [2-4] using micro-fabrication technology to generate support structures in a highly organized fashion. This prompted Desmet and co-workers to perform in-depth theoretical analysis and computational fluid dynamics simulation to predict the advantages and limitations.[5-8] In collaboration with prof. Schoenmakers of the University of Amsterdam and prof. Gardeniers of Twente University, a first device was produced and characterized.[9] The results were in perfect agreement with the simulations, but the used pillars were not studied under retentive conditions and the practical implications and advantages were hence still not adressed.

In the current study, the focus is on the separation behaviour of the pillar array. In a first stage, non-porous pillar arrays were coated and their dispersion behaviour was investigated under retentive conditions using fluorescent dyes. Then, in order to allow the performance of more relevant separations and to allow the detection of non-fluorescent dyes, the feasibility of an on-chip UV-vis absorption detection system is studied. Finally, a process has been developed to produce porous silicon pillars and the separation characteristics were analysed.

1.2 Thesis outline

The devices that have been characterized and tested throughout this work have almost all been fabricated at MESA+ Institute for Nanotechnology (The Netherlands). The device presented in chapter 5 was fabricated by Klaus Mogensen at the Technical University of Denmark. The deep-UV chips described in chapter 8 have been produced by Deniz Tezcan at the Interuniversity Micro-electronics Centre (Imec, Belgium).

Chapter 2

In this chapter, the history and some elementary theoretical background of liquid chromatography is discussed. Emphasis is put on the different available column formats and on the possible extension to chip-formats. For this purpose, also some elementary micro-fabrication principles are introduced to get more insight in the limitations from material engineering side.

Chapter 3

Shear-driven chromatography is theoretically the best possible LC operation mode, because it allows to establish mobile phase velocities without any pressure-drop limitation. One of the major obstacles to successfully put this technique into practice however is the absence of a reliable injection system. Chapter 3 describes the fabrication and development of an automated injection system. A theoretical consideration is also made to understand the time-evolution of the peaks and to predict the size limitation of the achievable peak widths.

Chapter 4

In this chapter, the first pressure-driven reversed-phase liquid chromatography separations in a pillar array column are described. The results are compared with the currently available column formats in the literature in terms of plate height and separation impedances. A thorough kinetic analysis is carried out to allow the overall interpretation of the combined effect of the above mentioned characteristics.

Chapter 5

As it has been predicted in the literature that small deviations between the dimensions on the photolithographic mask and the etched pillars (this is especially important at the sidewall region with respect to the 'magical distance') will partially mask the true chromatographic potential of the pillar array format, [10] the pillar arrays used throughout this thesis had wide

aspect ratios to anticipate this problem (typically 10 μm deep and 1 mm wide). This allows the evaluation of the separation performance of the pillar array by only observing the central part of the channel. Another argument to use wide channels was to gain experience in the use of channels that exhibit long path lengths when light would be coupled in the channel in a sideways fashion. In chapter 5, chips that have been produced by the μTAS group of the Technical University of Denmark have been tested and the peak shapes and their evolution during the passage through the channel was studied. The importance of the sidewall effect is addressed and also the effect of tapering of the pillars.

Chapter 6

The pillars used in chapters 3-5 consist of non-porous silicon or are covered with a layer of silicon oxide. Because of the non-porous nature, a very limited specific surface area is therefore available. This puts restraints on the achievable retention factors and hence also on the separation capacity. When a sample with a low abundant analyte needs to be separated, sometimes the working conditions will be such that a high abundant analyte will be present in very high concentrations. When not enough available surface is present, the separation will not be optimal because the lack of interaction surface will lead to overloading. To anticipate both issues, a microfabrication method was developed to allow the production of porous shell pillars using an anodisation technique in hydrogen fluoride. In chapter 6, the first ever sealed channel configuration is obtained that can withstand relevant pressures (tested up to 70 bar) and the homogeneity of the porous layers is confirmed.

Chapter 7

In this chapter, the dispersion characteristics of porous shell pillars are studied under both retentive and non-retentive conditions. To interpret the measurements, a model describing the band broadening as a function of porous shell thickness has first been developed. Using measurements under non-retaining conditions, the parameters of the model could be determined. Furthermore, a relation between the mobile phase strength and the retention capacity was established. Finally, a 4 component separation was demonstrated.

Chapter 8

To convert the pillar array column to a well established system that can replace the contemporary HPLC systems, some more research is needed. A number of critical issues that

still need to be resolved are discussed in this chapter, together with a number of potential solution strategies.

References

1.   Giddings, J.C., Dynamics of Chromatography Part 1, Marcel Dekker, New York, 1965.
2.   He, B.; Tait, N.; Regnier , F.E., *Anal. Chem.* **1998**, *70*, 3790-3797.
3.   Regnier, F.E.; *J. High Resol. Chromatogr.* **2000**, *23*, 19-26.
4.   Slentz, B.E.; Penner, N.A.; Regnier, F., *J. Sep. Sci.* **2002**, 25, 1011-1018.
5.   Gzil, P.; Vervoort, N.; Baron G.V.; Gert Desmet, *Anal. Chem.* **2004**, *76*, 6707-6718.
6.   J. De Smet, P. Gzil, N.; Vervoort, G.V.; Baron, G. Desmet, *Anal. Chem.* **2004**, *76*, 3716-3726.
7.   Billen, J. Gzil, P.; Vervoort, N.; Baron, G. V.; Desmet, G., *J. Chromatogr., A* **2005**, *1073*, 53-61.
8.   Billen, J.; Gzil, P.; Baron, G.V.; Desmet, G. *J. Chromatogr. A*, **2005**, *1077*, 28-36
9.   De Pra, M.; Kok, W.Th.; Gardeniers, J.G.E.; Desmet, G.; Eeltink, S.; van Nieuwekasteele, J.W.; Schoenmakers, P.J., *Anal.Chem.* **2006**, *78*, 6519-6525.
10.   Vervoort, N.; Billen, J.; Gzil, P.; Baron, G.V.; Desmet, G. Anal. Chem. **2004**, *76*, 4501-4507.

Chapter 2: Liquid chromatography and fabrication technology

2.1 The lab-on-chip

2.1.1 History and first principles

In the last decade, microfabrication techniques developed for the micro-electronics industry have found well their way to the microfluidics world. This field has undergone a huge transition towards miniaturization as the benefits involved with miniaturization are immense.

The pharmaceutical industry and the different –omics fields have welcomed the ability to work with smaller volumes in the nano- and picoliter range with great enthousiasm. Not only are less organic solvents or cultures required, for many applications there is just not a lot of sample available, as for example in single cell analysis. Besides these more practical reasons, more fundamental characteristics come into play. In smaller channels with concomitant smaller diffusion distances, the time for a molecule or particle to diffuse from wall to wall scales inversely with the square root of the distance.[1] This leads to lower dispersion due to the efficient averaging of the typical parabolic flow profile in closed channels working in pressure-driven mode, allowing faster and higher resolution chromatographic separations. Higher surface to volume ratios allow more efficient cooling and heating as compared to large scale configurations, giving the possibility to regulate the temperature very efficiently with minimal energy losses. Because of the higher efficiencies, smaller amounts of reactor supports and catalysts are required, complete plants can possibly be replaced by a room of a couple of square meters stacked with microreactors.[2]

The idea of an integrated silicon chromatograph was born in 1979, when Terry proposed a gas chromatograph integrated on a 2" silicon substrate.[3] The miniaturized silicon based device was capable of separating a complex mixture of compounds in a few seconds. At the same time, the development of the ink jet printer was going on at IBM.[4] Despite the remarkable properties of these two devices, research towards integrated microfluidics remained dormant for more than a decade. In the second half of the eighties research activities were increased in single components as pumps, valves and sensors.[4-7] The ultimate goal would appear to be a progression towards a μ-total-analysis system (μTAS), where injection, sample preparation (derivatization, concentration, etc.), separation and detection all occur in the same micro-scale

substrate. This was initiated by Manz et al., who reported on a device that consisted of a on-chip open-tubular column and a conductometric detector with a 1.2 pL volume detection cell.[8-9]

Even though the first μTAS device was designed for pressure-driven LC, the subsequent development concerned mostly electrokinetic separation methods such as capillary electrophoresis (CE), capillary electro-chromatography (CEC) and micelar electrokinetic chromatography (MEKC).

The initial optimism has dropped during the last years along with the realization that many practical hurdles exist inherent to the completely different format and materials that are proposed. Apart from some success stories,[10-12] few systems have been fully integrated so far. Interfacing and clogging appear to be a major issue when it comes to reproducibility and the shelf-life of a system. For example, a field such as HPLC has needed decades to establish satisfactory coating protocols on silica to provide the required coverage of adsorbing groups and also to provide large pH resistances. This research was namely typically carried out on materials that cannot be so easily integrated on chips, not to speak of the harsh conditions of many of the required treatments.[13]

2.1.2 Microfabrication technology

2.1.2.1 General concepts

Micromachining technologies are primarily silicon-based, due to both the traditional role of this semiconductor in microelectronics technology and its excellent mechanical properties. A typical process involves combinations and repetitions of: patterning a photosensitive polymer (photolithography), removing material of the exposed substrate surface (etching) and depositing new material on the substrate. The latter is mostly a gaseous phase deposition, the required energy to overcome the activation energy of the reaction is either provided by a plasma and/or thermally and/or chemically. Most used processes are low pressure chemical vapour deposition (LPCVD) and plasma enhanced chemical vapour deposition (PECVD).[14-15]

2.1.2.2 Lithography

When 3D features are required (as in most applications), a pattern has to be transferred. To accomplish this, typically a photoresist is applied on a substrate (by spinning or spray-coating). The polymer is then illuminated through a photomask, making it either soluble or

non-soluble during the subsequent development step (respectively positive and negative resist). Due to light dispersion effects, the feature dimensions can be subject to changes depending mainly on the applied wavelength and the distance between the mask and the substrate.

The imaging performance of optical-lithography is described by the Rayleigh resolution criterion, developed more than 100 years ago to describe the diffraction limits of astronomical telescopes. It describes the ability of an imaging system to resolve two closely spaced objects, and in the field of lithography effectively defines the smallest half-pitch of a feature on an integrated circuit. The critical dimension (CD) is equal to:[16-17]

$$CD = \frac{\kappa \lambda}{NA},$$ (1)

with λ the wavelength, NA the numerical aperture of the imaging system and κ a value between 0.25 and 1 depending on the configuration of the illumination system and the optical response of the resist. In the case of the value $\kappa=1$ a complete intensity null is present between two well resolved features, whereas a value $\kappa=0.6$ corresponds to a 20 % intensity dip between two diffraction limited spots for incoherent illumination conditions (what appears to be the practical limit for conventional lithography). Various resolution enhancement techniques have been developed to extend κ towards the fundamental limit of 0.25.[17] These strategies imply reducing κ and λ or increasing NA.

The photomask can by produced by either laser lithography or electron-beam lithography (EBL), the latter technique has produced lines as small as 10 nm. EBL can also be used to directly pattern a wafer, but this ends up very expensive and time consuming.

The wavelength of optical lithography used in chip manufacture has progressed from 432 nm (the G-line of Hg) to the current value of 193 nm (ArF excimer laser). Each shift has been accompanied by an extensive and expensive effort in developing appropriate optical sources and illumination imaging optics.

The next logical step is 157 nm, but there are several issues concerning the lens materials at this wavelength and development is temporarily on hold. There is also ongoing work on

developing extreme ultraviolet (EUV) technology at 13 nm, but this is a huge jump in wavelength that will require a complete overhaul of lithography equipment.

At the same time, there has been much improvement in the NAs of lithography lenses with values increasing from 0.1 to today's figure of around 0.9. In immersion lithography a liquid is added between the lens and the wafer in order to alter the NA. This technique increases the NA of the imaging system by a factor that is equal to the refractive index of the liquid and will lead to NAs greater than unity. NAs of ~1.3 are feasible with water immersion at 193 nm, and there is an active search under way for higher index fluids to increase the resolution further.

Another strategy for reducing the CD is decreasing the value of κ by using so-called resolution-enhancement techniques (RETs). However, decreasing κ also reduces the allowable variation in optical exposure across the image, so tighter process control is required. Adding sub-resolution structures to the mask to introduce phase-shifts (optical proximity correction) can be a valuable strategy. Illumination-based RETs include off-axis illumination and imaging interferometric lithography. Combining all these techniques can produce κ_1 values nearing the theoretical limit of 0.25.With all of these improvements in NA, wavelength and κ_1, the imaging limit of optical lithography extends to a CD of ~ 40 nm.

Most research institutes use mid-UV-light, in practice allowing minimal line widths of about 2 μm (for example MESA+ Institute for Nanotechnology). Better results can be obtained with deep-UV, but the equipment is extremely expensive going up to tens of millions of €.

Extreme UV lithography has even higher potential, but so far only prototypes have been produced and the expected prices are excessive.

Laser interference techniques are interesting when periodic spatially coherent patterns are desired. In this process, two coherent beams interfere to produce a standing wave, which is recorded on a photoresist. As the spatial period can be as low as half the wavelength of the interfering light, structures of the order of 100 nm are possible using mid-UV wavelengths. Using a DUV ArF laser, features as small as 30 nm have been patterned.

An alternative means to pattern a polymer is by physical imprinting. The expensive lenses are hence omitted and resolution is about equal to the template size.

In hot embossing, a thermoplastic polymer is heated above the glass transition temperature and pressed to the template at elevated pressures, allowing the polymer to fill the spaces in between the features of the template.[18] Then the polymer is cooled down and withdrawn from the template in rigid form. Next, the imprinted polymer is etched without masking to remove a residual layer. A major disadvantage of this technique is the pattern density dependence of the residual layer, imposing a limit on the design.[19] Another issue is that the template, the substrate and the substrate material need to have a similar thermal expansion coefficient and should be sufficiently thermally conductive. This excludes glass as a substrate, making it difficult to align different masks with a reasonable accuracy.

Step and flash imprint lithography[20-22] uses a low viscosity photo-curable monomer that fills the accesible space in the template mainly by capillary force (the used pressures are typically 0.1 bar). At the end of this filling process the solution is hardened using UV-light. The technique is not dependant on the loading (the feature density) and uses quartz templates (allowing aligning).

The latter technique is relatively unknown but has probably the highest potential in terms of resolution.

In this thesis we have mainly used the mid-UV-light photolithography option. Some work was done in collaboration with Imec on deep-UV, and in the last chapter of this thesis also some preliminary results obtained with SFIL will be discussed.

2.1.2.3 Etching

Etching in silicon can occur in 4 ways: wet anisotropic, wet isotropic, dry anisotropic and dry isotropic. For wet anisotropic etching, aqueous KOH solutions are typically used. The anisotropic nature of this kind of etching is due to the low etch rate of the (111) crystallographic planes, allowing different combinations dependent on the orientation of the dicing surface.[14]

Dry etching requires a plasma and etching gasses, depending on the conditions the shape can vary from perfectly vertical to positive or negatively tapered to even isotropically shaped.

A gas glow discharge is used to dissociate and ionize relatively stable molecules, so that chemically reactive and ionic species are formed. These will then react with the solid being etched, what results in the formation of volatile species.

Depending on the dry etch mechanism, different varieties of plasma etching are conceivable. The most frequently used process is reactive ion etching (RIE), where reactive species are generated in the plasma from the feed gas (typically SF_6 for silicon as a substrate), these can

etch the surface either chemically (radicals), physically (ions that are accelerated towards the surface to the electrical bias on the substrate surface) or in a combined chemical-physical way.[1] The rf power used to generated the plasma can be either in the planar (capacitive) configuration or in inductively coupled plasma (ICP) configuration. An important advantage of ICP is that no high-voltage sheaths are present in the chamber, avoiding sputtering of the wall. Some tools include an extra internal electrode to develop a DC bias voltage, a high-power can then independently provide a high density of reactive species.[15]

In order to achieve high aspect ratio's, a cyclic process can be implemented so that the supply of passivation gas (typically C_4F_8) and etching gas is alternated. In between these two steps, a short directional bombardment step (typically with argon) exposes the silicon at the bottom of the substrate to allow the etch gas to react. In this so-called Bosch[®] process, the switch frequency is limited by the time needed to change the reactor volume.

Wet isotropic etching in silicon is possible by means of aqueous HF-containing solutions, that also have an oxidant such as HNO_3. The method is thought to be a combination of a silicon oxidation step followed by the removal of the resulting silicon oxide by HF. As opposed to wet anisotropic etching where the etch rate is limited by surface reactions, the mass transfer of active species and reaction product in the solution is the limiting factor here.

In this thesis we have mainly used the Bosch[®] process to etch silicon substrates.

2.1.2.4 Bonding

Wafer bonding refers to the mechanical fixation of two or more wafers to each other. depending on desires and restraints, different approaches are possible.

Silicon fusion bonding (SFB) is a process where two wafers are contacted and annealed in an oxidation furnace at 900-1100 °C. The success of this process is highly dependant on the quality of the wafer surfaces. Wafer curvature and surface roughness are critical, limiting the use of many process steps on the wafer to be bonded because process induced roughening can occur and etched features will give rise to intrinsic stress and the accompanying deformation of the wafer.

Anodic bonding is a process where an electric field is used to accomplish the bonding between a silicon wafer and glass wafer (typically Pyrex or Borofloat). The process occurs at a relatively low temperature (180-500 °C), other advantages compared to SFB include low residual stress, and the less stringent requirements on the surface quality of the wafers (1 µm rms). Typical used voltages are between 200-1000 V. The elevated temperature is required to allow the glass to become a conductive solid electrolyte, so that the positive sodium ions

present in the glass become mobile and can migrate towards the cathode. This generates a depletion region adjacent to the glass-silicon interface. The thermal expansion coefficients of the silicon and the glass should match. A native or thermally grown oxide layer can be present on the silicon, but should not exceed 200 nm to produce a good bonding.[15]

In this thesis anodic bonding was applied on silicon directly, but also with a layer of silicon oxide and silicon nitride deposited on the silicon substrate.

2.1.2.5 Porous Silicon

Doped silicon can be electrochemically etched in fluoride containing solutions. Depending on the current density, different etching regimes exist. For p-type Si, porous silicon is formed at low currents. Increasing the current, the Si becomes electropolished and at even higher currents the etching rates become drastically higher (see Fig. 1). This means that with a simple change of the current, one can alternate between etching and purification, in this way producing sieves as was demonstrated by Tjerkstra et al.[23-25] The electrochemical dissolution of silicon requires electronic holes (the lattice has a lack of electrones) at the surface. The holes are already present in p-type silicon, whereas in n-type silicon the holes can be generated by illuminating the substrate with photons that have more energy than the band gap (1.1 eV). The holes are further continuously forced to the surface by applying a potential across the wafer.

Plotting the current versus the applied potential, a characteristic curve is obtained for a certain substrate and HF concentration. Three regimes are distinguished: the cathodic range, the porous silicon range and the electropolishing range. The cathodic range is associated with a negative potential and this can only lead to the generation of holes in the case of n-type silicon. In the first zone of the I-V curve (see Fig. 1), the zone before the first peak is associated with the formation of porous silicon (PS). This zone is divided in the microporous zone (pore sizes below 2 nm) and the mesoprous zone (pore sizes between 2 and 50 nm). The morphology and the anodisation rate depends on the doping density, the HF concentration and the current density. In the electropolishing range, the current exceeds the critical current density and the surface is smoothened.

The exact dissolution chemistries of silicon are still unclear and different mechanisms have been proposed. Turner and Memming and Schwandt have proposed the following reaction for the dissolution of silicon:[27-28]

$$Si + 2\ HF + \lambda h^+ \rightarrow SiF_2 + 2\ H^+ + (2-\lambda)e^-$$

$$SiF_2 + 2\,HF \rightarrow SiF_4 + H_2$$
$$SiF_4 + 2\,HF \rightarrow H_2SiF_6\,,$$
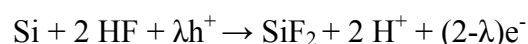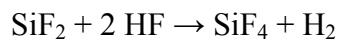
where h^+ and e- are the exchanged hole and electron, respectively, whereas λ is the number of charges exchanged during the elementary step.
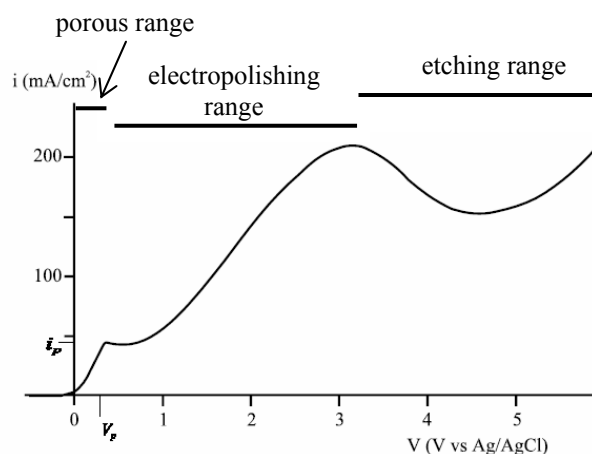
Fig. 1 i-V curve of a p-type silicon wafer in a 5% HF solution. Resistivity of the wafer 0.01 - 0.018 ohm cm, the scan rate is 500 mV/s (taken from ref. 26).

Mechanisms, based on the same approach are often suggested in the literature.[29-32] For example, Lehman and Gösele[33] have proposed another variant for the dissolution mechanism based on a surface bound oxidation scheme, with hole generation and subsequent electron injection, which leads to the divalent silicon oxidation scheme.

All the properties of a porous silicon layer, such as porosity, thickness, pore diameter and microstructure are strongly dependant on the anodization conditions. These include HF concentration, pH of the solution and its chemical composition, current density, wafer type and resistitvity, crystallographic orientation, temperature, anodisation duration, stirring conditions and illumination (or not) during anodisation.

It appears that for a given HF concentration, the porosity increases with increasing current density and for a fixed current density the porosity decreases with increasing HF concentration. For given anodisation conditions (current density, HF concentration), the porosity is much higher for the thicker layer.

The internal surface of PS layers varies from about 200 to 600 m^2/cm^3 depending on the dopant level of the substrate. Increasing the current density under the same conditions also increases the pore radius size. Typical pore sizes are between 2 and 15 nm.[34]

2.2 Chromatography

2.2.1 Concept of chromatography

Chromatography is a technique that allows the separation of a mixture of species in separate compounds. It is based on different distribution of compounds between a mobile and a stationary phase. The latter can be a wax, solid or an immobilized liquid whereas the former can be any fluid that has sufficient selective solubility for the analyte compounds in order to generate different migration velocities. The selectivity mechanism comprises charge, hydrophobicity, partitioning, size, adsorption, molecular recognition or a combination of these mechanisms. An important effect besides migration is dispersion, what causes the peaks to become wider in time. The capacity from a column to restrain the dispersion is called column efficiency, also referred to as height equivalent to a theoretical plate (plate height). Over a complete column, this leads to a number of plates (N), which is a measure for the number of exchanges or equilibria that can take place (the concept originates from the distillation theory).

The first chromatographic separation was performed in 1906 by the Russion botanist Mikhail Semenovich Tswett, who separated a coloured leaves extract by sending a sample of it through a column packed with calcium carbonate conditioned with organic solvents.[35] Due to different affinities of the pigments he saw different coloured bands, hence the name chromatography (*khromatos* means 'color' and *graphos* means 'writing').[36] Despite the importance of Tswett's experiment back then, the true potential of the technique became only widespread in 1931, after a separation experiment of carotenoids present in egg yolk, performed by Edgar Lederer at the University of Heidelberg. A next hallmark in liquid chromatography (LC) was the development in 1941 of partition chromatography by A.J.P. Martin and R.L.M. Synge. They coated silica-gel particles and separated a mixture of monocarboxylic acids (present in wool) and obtained different bands due to the different partition coefficients of the compounds.[37] They also demonstrated a separation of dicarboxilic amino acids using a sheet of filter paper as stationary phase, what was at the time impossible with any other technique given the close resemblance of these components. Martin developed also gas chromatography later on.

The development of gas chromatography has been an extremely successful story because of the large advantage that in this case the simplest conceivable open-tubular format is highly efficient (as opposed to LC).

In the beginning of the sixties NASA's lunar project made it clear that in order to analyse the gathered samples, more powerful separation techniques to separate non-volatile biological samples were required. An obvious development was the generation of higher pressure to achieve higher flow rates and faster (and higher resolution) analysis.[38-40] Both the ability to generate 400 bar and the development of homogenously packing procedures for 5 μm and 3 μm particles lead to the technique high performance liquid chromatography (HPLC), a tool that can now be found in any laboratory where biological samples are being analysed. The consumption of analytical columns is estimated to be ca 2 million per year. If one assumes that each HPLC instrument requires 5 columns per year on average, the abundance of HPLC instruments can be easily assessed.[41]

2.2.2 Theory

The partition equilibrium of a component between the stationary and the mobile phase, the basis to achieve a separation, is given by the ratio of the concentration of the component in the stationary phase to the concentration in the mobile phase and is known as the partition coefficient K:[42]

$$K = \frac{C_s}{C_m} \tag{2}$$

The ratio of the amount of material present in the stationary phase to the amount present in the mobile phase is proportional to the partition coefficient and is defined as the retention factor:[43-44]

$$k' = \beta K \tag{3}$$

with β the phase ratio.
The retention factor can also be written as:

$$k' = \frac{t_r - t_0}{t_0}, \tag{4}$$

with t_0 and t_r the respective residence times of a non-retained and a retained component.

To express the chromatographic potential of a column, Martin and Synge introduced the concept of height equivalent to a theoretical plate (HETP).[45] The concept evolved from the plate analogue in distillation theory, where many physical plates are crossed to establish a separation. Despite the non-equilibrium nature of a chromatographic process, when assuming that between each theoretical plate the solute achieved an equilibrium between the stationary phase and the mobile phase, a plate height constant can be defined as:

$$H = \frac{\Delta\sigma_x^2}{\Delta x},$$ (5)

with σ_x the spatial peak standard deviation and Δx the travelled distance. Often the initial peak width is neglected and then $\Delta\sigma_x^2$ is written as σ_x^2.

The column efficiency of a column with length L is the defined as:

$$N = \frac{L}{H}$$ (6)

An attempt to correlate the column properties with H on a theoretical basis was first made by van Deemter, in an approach nowadays known as the rate theory. The importance of specific column parameters is strongly dependant on the mobile phase velocity u_0, as can be seen in the van Deemter equation:[46]

$$H = A + \frac{B}{u_0} + Cu_0$$ (7)

The A term is independent of the mobile phase velocity and is caused by the tortuosity of the flow paths in chromatographic supports, the associated dispersion is often referred to as Eddy-diffusion. In an open tubular (OT) system, no tortuous paths are present and hence no A-term is present in an OT system. In general, the A-term represents the heterogeneity of the system and the quality of the packing has a huge influence on this term. For a particulate bed, the term can be expressed as a function of a geometrical constant λ and the particle diameter d_p:

$$A = 2\lambda d_p$$ (8)

The B-term represents the stochastic thermal movement of the individual molecules of the component, often referred to as longitudinal diffusion. It is comprised of an obstruction factor (Q) and the molecular diffusion coefficient D_m:

$$B = 2QD_m \tag{9}$$

The C-term is related to the mass-transfer resistance between the stationary phase and the mobile phase. It can be divided into a resistance from the interface towards the stationary phase (C_s) and a resistance towards the mobile phase (C_m)

The C-term is also influenced by the stationary film thickness d_f and the stationary zone diffusivity D_s and is given by:

$$C = C_s \frac{k'}{(k'+1)^2} \frac{d_f^2}{D_s} + C_m \left[\frac{k'}{(k'+1)} \right]^2 \frac{d_p^2}{D_m} \tag{10}$$

Since all the above described processes can be assumed to be non-interacting, the individual contributions of the variances (and to the plate height) can be simply summed.[47] Looking at equations 8-10, the importance of the particle diameter is clear (see Fig 2).

Another approach was used by Knox and Parcher, scientists that at the time were evaluating the performance of particles of different size. To compare the efficiency of the particles, Knox used the reduced (dimensionless) forms of H and u:[48]

$$h = \frac{H}{d_p} \tag{11}$$

$$v = \frac{ud_p}{D_m} \tag{12}$$

Using these parameters, Knox proposed the following equation after comparing the different columns he had tested:

$$h = A'v^n + \frac{B'}{v} + C'v \tag{13}$$

Typical parameters to obtain the best fit are A'=1, B'=2, C'=0.1 and n=1/3.[49-50] Because the constants are obtained by fitting experimental data and are not derived theoretically, the model has no real use in columns design but is nevertheless valuable to measure and evaluate columns quality and therefore it is used by many researchers.
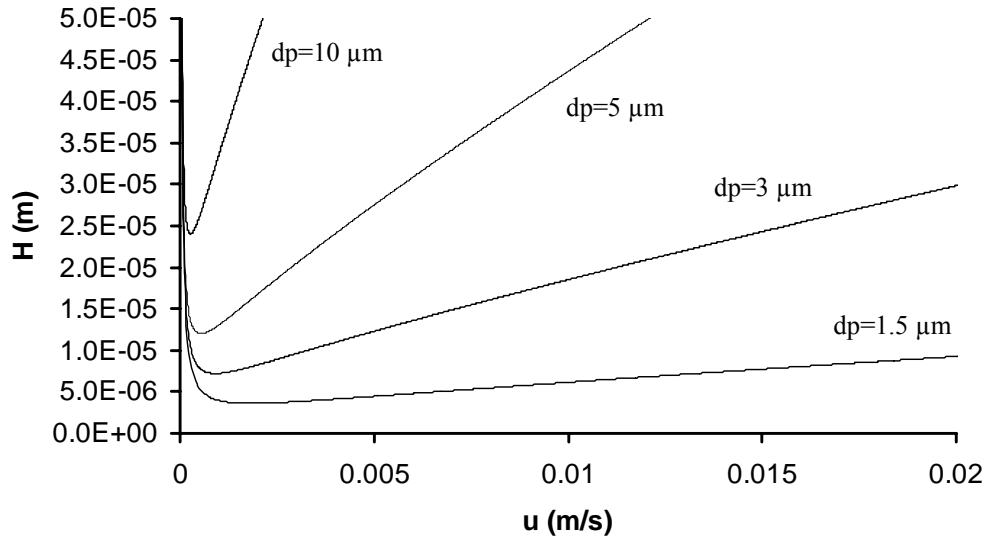
Fig. 2 Van Deemter curves of packed beds with different particle sizes. The curves were established using the Knox equation (A=1, B=2, C=0.1, n=1/3).

Besides the column efficiency, another equally important property of a column is the flow resistance, defined as:

$$\phi = \frac{d_p^2}{K_v},$$ (14)

With K_v the Darcy permeability of the column:

$$K_v = \frac{u\eta L}{\Delta P}.$$ (15)

To combine both the column efficiency and the flow resistance, a separation impedance was introduced by Giddings:

$$E = h^2\phi$$ (16)

The resolution of a separation shows the quality of a separation, it is typically applied to closely eluting components. Resolution is defined by:

$$R_s = \frac{2\Delta t_r}{W_1 + W_2}$$ (17)

with t_r the elution time and W_1 en W_2 the time-based width of the eluting peaks. Assuming Gaussian peaks the peak width can be approximated as $W=4\sigma$. Combining this with equation 17 yields:

$$R_s = \frac{\sqrt{N}}{4}\frac{k'}{1+k'}\frac{\alpha-1}{\alpha}$$ (18)

with $\quad \alpha = \frac{k_2'}{k_1'}$, (19)

this can be rewritten as:

$$N = 16R_s^2\left[\frac{\alpha}{\alpha-1}\right]^2\left[\frac{k'+1}{k'}\right]^2$$ (20)

Combined with:

$$t_r = \frac{L(1+k')}{u_0},$$ (21)

this results in:[47]

$$t_r = \frac{16R_s H}{u_0}\left[\frac{\alpha}{\alpha-1}\right]^2\frac{(k'+1)^3}{k'^2}$$ (22)
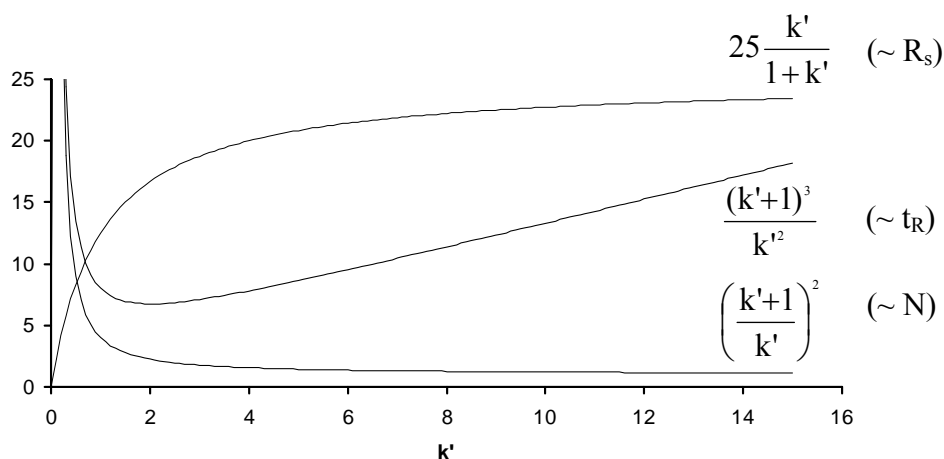
Fig. 3 Influence of k' on t_R, N and R_s

The term $(k'+1)^3/k'^2$ has a minimum at around k'=2. For k'<1, the analysis time is increased dramatically (see Figure 3). The term k'/(1+k') increases with increasing k', but the increase in resolution is less pronounced than the corresponding increase in analysis time. As above k'=5 the resolution is reaching a plateau, a compromise is typically searched between resolution and analysis time. A value between 2 and 5 is used in practice. The term $[(k'+1)/k']^2$ in Eq. (20) increases dramatically when k'<1. Even though a large increase in plate number is accomplished, the loss in resolution and the large increase in analysis time make this region unfavourable.[42]

2.2.3 Flow generation

2.2.3.1 Electro-osmotic flow

The predominant way to propel a liquid on a chip, described in the literature, is by electro-osmotic flow (EOF). When the acidic silanol groups of glass are brought into contact with an ionic solution, cations will bind to the surface. The resulting sandwich of adjacent layers with negative and positive charges makes up the so-called electrical double layer. When a potential difference is applied along the length axis of the channel, the cations within the diffuse layer will migrate towards the cathode, and by doing so take along their hydratation layer. The electrical double layer that encloses the entire mobile phase contained within the channel will generate a bulk flow directed towards the cathode: the electro-osmotic flow. The flow profile is flat, in contrast to the parabolic flow profile encountered in a pressure-driven system. This offers a significant advantage over pressure-driven methods, because the contribution of the peak dispersion due to the mass transfer in the mobile phase is reduced.

The EOF-generated velocity is described by:[51]

$$u_{eof} = \frac{\varepsilon_0 \varepsilon_r \zeta}{\eta} \frac{\Delta V}{L} \qquad (23)$$

with ε_0 and ε_r the dielectric constants of the vacuum and the solvent, respectively. ΔV is the voltage gradient, η is the viscosity of the solvent, L is the channel length and ζ is the zeta potential. The latter parameter is defined as the potential of the electrical double-layer at the plane of shear, which is dependant on the capillary surface charge and the double layer thickness. This explains the influence of the pH and the ionic strength of the flow solution on the mobile phase velocity. Below pH=4, the number of ionized silanol groups is so low that EOF disappears. The EOF is the highest above pH=8.5, when the silanol groups are fully ionized. The presence of an organic solvent in the mobile phase also influences the EOF. These factors are a huge drawback of EOF-driven systems, because the mobile phase composition can not be freely chosen, which can prevent a successful separation when using for example hydrophobic interaction as partition mechanism. Also, the solution resistance to current transport is accompanied by Joule heating, drastically reducing column efficiency due to the occurrence of radial temperature gradients and the accompanying viscosity and diffusion rate gradients. Under optimal conditions, the maximum EOF that can be achieved in a 50 µm ID capillary packed with 3 µm particles is about 3 mm/s. As commercial power supplies cannot exceed 30 kV, similar velocity limitations exist in pressure- and EOF-driven systems.[52]

On the other hand, Eq. (23) shows that channel (or particle) diameter does not affect the mobile phase velocity which is a huge advantage over pressure-driven flows. However, a lower limit exists to the capillary diameter. Channels having a limited width will have an overlapping electrical double layer (EDL), so that the diffuse layer cannot fully develop. This results in a decrease in EOF, the corrected value is then:[53]

$$u_{eof} = \frac{\varepsilon_0 \varepsilon_r \zeta E}{\eta} \left[1 - \frac{2 I_1(r_p / \delta)}{(r_p / \delta) I_0(r_p / \delta)} \right] \qquad (24)$$

with I_0 the zeroth order modified Bessel function of order one, I_1 the first order modified Bessel function of order one and δ the thickness of the EDL that is given by:

$$\delta = \sqrt{\frac{\varepsilon_0 \varepsilon_r kT}{2 N_a e_0^2 C_s}} \qquad\qquad (25)$$

With k the Boltzmann constant, N_a Avogadro's number, T the temperature, C_s the ionic strength, r_p the radius of the channel and e_0 the elementary charge unit. Looking at Fig. 4, it can be seen that the EOF velocity decreases, but also that the flat profile becomes parabolic at small channel aspect ratios.
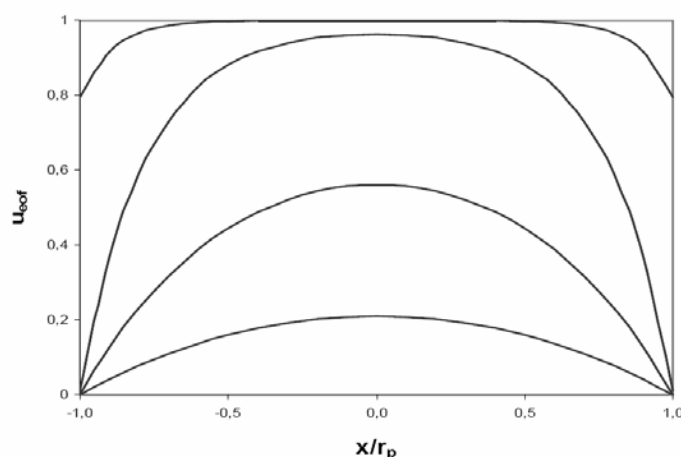
Fig. 4 Electro-osmotic flow profile in an open tube at r_p/δ values of 1, 2, 5 and 10 (lower to upper curve), with x the position with respect to the channel centre.

2.2.3.2 Shear-driven flow

Shear-driven-chromatography (SDC) takes advantage of viscous drag, an effect that in pressure-driven chromatography imposes a limit on the kinetics and the performance of the separation. [54-56] In SDC, a moving wall element provides an impulse source, dragging the fluid through the channel without the need for a pressure or voltage gradient. A cross section of the system is given in Fig. 5. The flow rate is only determined by the velocity of the moving element and is independent of the channel depth. A linear velocity profile is obtained, in this way providing an average velocity equal to half the velocity of the moving wall. The independence of the flow rate on the channel depth (d) is the basic advantage of SDC, as the speed of a chromatographic separation scales with d^{-2}. As pressure and electrically driven systems are limited in length (L) due to pressure and voltage drop limitations, and the resolution of a separation scales with L/d, it is clear that SDC theoretically has a tremendous and sheer unlimited potential.
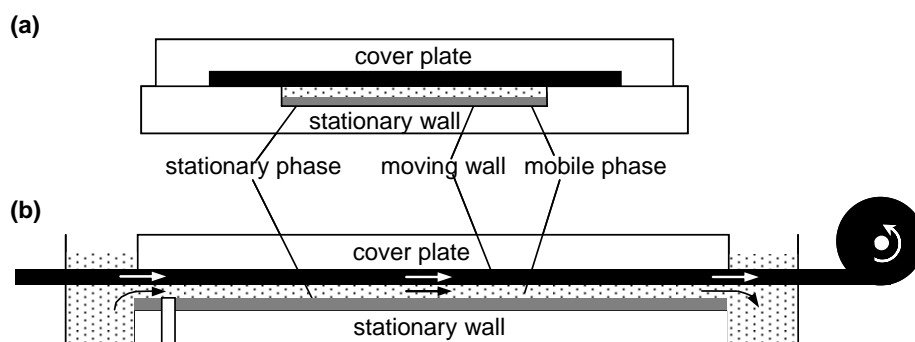
Fig. 5 Radial cross section **(a)** and longitudinal cross section **(b)** of a basic design for a shear-driven chromatography apparatus. The dimensions of width, length, and thickness are not to scale. The white and black arrows respectively denote the movement of the movable wall and the mobile phase.[56]

2.2.3.3 Pressure driven flow

Standard HPLC pumps can at the moment deliver 400 bars. The pressure drop of a column is described by

$$\Delta P = \varphi \eta L u / d_p^2 \tag{26}$$

with φ a geometrical constant, η the mobile phase viscosity, d_p the particle diameter, L the column length and u the mobile phase linear velocity. When performing a separation experiment, it is important to work around the optimum of the van Deemter curve. This imposes a limit on the column length and/or on the particle diameter. Recently, some laboratories are working with pressures as high as 3500 bars (referred to as ultra-HPLC) to increase the performance, recently Jorgensen et al achieved 350,000 plates working with a column of 50 cm long packed with 1 μm particles.[57-59] Besides the lack of commercially available high-pressure equipment, the generated heat in the column and its dispersive effect is recently in debate. The uneven radial and axial temperature gradients result in different viscosities, making the peaks subject to additional dispersion. The effects become however a lot smaller when decreasing the column diameter.

Porous particles of 1.8 μm have recently become commercially available as Zorbax RRHT® by Agilent,[60] pumps capable of generating 1000 bars have recently become commercially available by Waters. To reduce frictional heating, columns and minimize temperature effects, the column diameter should not be larger that 2 mm. Moreover, columns packed with small particles should contain frits with an appropriate porosity to retain the particles.[41]

Besides using higher pressures, another way to increase the mobile phase velocity is the usage of heated columns so that the working conditions occur at lower viscosity.[62-63] LC at elevated

temperatures has traditionally not been widely used, except for size exclusion chromatography (SEC) of polymers of low solubility, often requiring temperatures of 150 °C in halogenated aromatic solvents to be kept in solution.[61] Three serious impediments have to be accounted for.[62-64] First, the stationary phase must be thermally stable. A variety of stationary phases that can withstand 200 °C have been developed over the last years. Second, the temperature mismatch between the incoming eluent and the column must be minimized (below 5 °C), because a temperature gradient is a serious cause of additional band broadening. The associated heat effects were discussed by Poppe et al.[65] And last, the analytes should be thermally stable on the time-scale of a chromatographic run.[66]

2.2.4 Columns formats

2.2.4.1 Packed columns

In the early years of chromatography, the most widely used materials were limestone, silica gel, hydroxapatite and diatomaceous earth. These irregular shaped particles had size ranging from 30 to 100 μm. The large size and the low selectivity limited the separation power of these devices, whereas the low stability and the fact that the packing methods at the time were more of an art than of an established method, made the results very irreproducible.

In the 1940s to the 1960s superficially porous shelled particles with a solid silica core of 25 μm were developed by Kirkland. The particles demonstrated very good mass transfer characteristics and were commercially marketed as Zipax®.[67]

In 1969, Knox and Saleem had started thorough theoretical contemplations on the optimization of the speed and the efficiency of packed columns, they concluded that particles of the order of 2 μm with operating pressures of minimum 200 bars were necessary. This initiated the search for methods to produce and pack smaller and smaller particles. At that time, columns were dry packed using vibrational techniques, it was however impossible to use this technique moving over to particles below 20 μm due to static charge buildup. Inspired by the work of Huber in the field of GC, Kirkland then developed a slurry packing method with porous silica microspheres, commercialized by DuPont as Zorbax®.[68]

Another focus point was the surface chemistry and the purity of the particles. This led to the development of the B-type silicas, that had a low metal content and surface acidity and that could be fabricated more reproducibly than earlier types.

From the 1980s to the 1990s the diameter was reduced to 5 μm, nowadays particles down to 1.8 μm are commercially available. Jorgensen and co-workers have used even particles as

small as 1 μm. Since they needed 7500 bars to carry out their experiment and most modern HPLC equipment is limited to 400 bars, this technology is only relevant on the academic level at the moment. [69-70]

Different formats of the particles are currently available. Non-porous silica (NPS) are thin porous shelled particles in the range of 1.5-2.5 μm, that exhibit lower dispersion because of the more efficient mass transfer. The lower associated surface however decreases the loading capacity, making the particles not suitable for trace analysis and low sensitivity detectors. Also the high back-pressures that are needed inhibit the success of these particles. Superficially porous particles are larger (5 μm) and coated with a thicker porous shell. Due to the lower required back-pressure and the better loading capacity, the particles (commercialized as Poroshell®) are very useful to separate slowly diffusing molecules.[71]

Different pore sizes are used depending on the dimension of the analyte to be separated. For low molecular weight compounds, particles with pore diameters between 6-50 nm are typically used, presenting specific surface areas of 100-400 m^2/g. For low molecular weight fine chemicals, pore sizes of 10-12 nm are adequate, whereas 30 nm is an appropriate dimension for analytes of a molecular weight between 20,000 and 50,000 Da.

For the separation of synthetic polymers and biopolymers, pore sizes larger than 50 nm (specific surface area's smaller than 50 m^2/g) are mainly used.[41] As a rule of thumb, the average pore diameter should be 4 times larger than the hydrodynamic diameter of the analyte, else the intra-particle diffusion becomes hindered. An important issue is that the pores should be sufficiently interconnected, to keep the intra-particle dispersion at a minimum.[72-74]

Recently, advanced Materials Technology introduced a novel column type marketed as Halo HPLC column, based on a fused core particle technology developed by Kirkland.[41] These particles are composed of a solid silica core (1.7 μm diameter) surrounded by a porous layer (0.5 μm thickness). The specific surface area is 150 m^2/g and the average pore diameter is 9 nm.
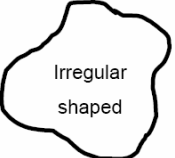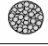
Non porous particles exhibit excellent mass transfer characteristics, but have a limited mass loadabality. A super-high-speed separation of 6 proteins within 60 s was demonstrated using a Micra NPS silica column coated with polystyrene in gradient elution mode.[75]

Perfusion packings consist of another type of particles that have besides diffusive pores, also flow through pores. The latter increases the mass transfer in the mobile phase, because a flow

through the particle is generated. The commercially available format of these particles is about 12 μm in size, this large format is very suitable for preparative separations.

The stationary phase in HPLC is mostly a C8 or C18 phase (92 % abundance), but phenyl phases are also becoming more and more popular.[13]

Table1. Evolution of the commercially available particle sizes and shapes of chromatographic packing material. Reproduced from[76]

Year of acceptance	Particle size	Most popular nominal size (μm)	Plates/15 cm (approx.)
1950s	Irregular shaped	100	200
1967	Glass beads	50 (pellicular)	1000
1972		10	6000
1985		5	12000
1992		3-3.5	22000
1998		1.5 (pellicular)	30000
1999		5 (Poroshell)	8000*
2000		2.5	25000
2003		1.8	32500

* for proteins MW 5700

2.2.4.2 Monoliths

A disadvantage of the particulate column format is that the mass transfer characteristics and the flow resistance are coupled, so that a compromise has to be made between fast enough mass transfer and fast enough flow rates.[78]
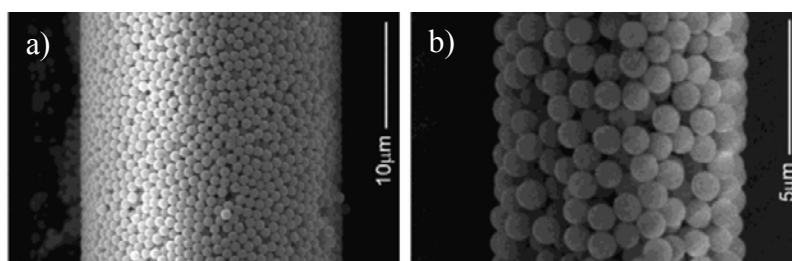
Fig. 6 Sem images of extruded sections of a 1 μm non-porous particle bed for a **a)** 30 μm and **b)** 10 μm internal diameter capillary (reprinted from ref 77)

This has lead to the development of monoliths, materials that have a continuous porous skeleton with relatively wide flow through pores. Whereas the former still exhibited a high

flow resistance, the latter lacked solvent stability. At the end of the 1980s Hjerten et al. used poly(acryl acid-co-methylenebisacrylamide) to separate proteins. These foams could not withstand high pressures however, not really presenting true kinetic advantages in the end.[85]

A breakthrough occurred in the 1990s when Frechet, Svec and co-workers introduced an in-situ polymerization process. Because the stationary phase could be cast inside the column, the mechanical stability of the monolith was dramatically increased. The polymerization solution typically consists of a mixture of free monomers (with a cross-linker), a free radical initiator and a porogenic solvent. The initiator is activated thermally or by photo-activation. Given the wide range of available monomers and the associated chemistries, interactions such as ion-exchange, hydrophobic interaction and reversed-phase are possible. Furthermore, by adjusting the porogen solvent composition, the porous properties can be easily tailored.

The columns are well suited for low and high pH applications and exhibit excellent biocompatibility.[86]

The polymers tend to swell when they come in contact with solvent, increasing the pressure drop. The major applications can be found in the field of ion-exchange chromatography and SEC. The material is very popular for the separation of proteins and nucleic acids.[87-88]

Besides these polymeric monoliths, also a silica analogue is available. Already in 1979, Pretorios and co-workers reported on a method to prepare an open-pore silica foam, but because the surfactant used to create the foam was never identified, a chromatographic evaluation never took place. In 1996 Fields et al. prepared a xerogel-based silica monolith by heating a potassium silicate solution in a fused silica capillary.[89]

Nakanishi et al. developed a procedure to generate bimodal pores in the monoliths, with better homogeneity and better separation performances.[90-91] In this process, an alkoxysilane is hydrolized in the presence of an acidic or basic catalyst and poly(ethylene)glycol is used as the porogen. In contrast to polymer monoliths, the silica monoliths shrink after the gelation process and can hence not be produced in-situ. After the solidification process, the porous rod is removed and cladded with polyetheretherketone. Compared to particulate columns, the pressure drop is about 30-40 % less whereas the efficiency is comparable to 3.5 μm particles. The mesopore sizes are of the order of 13 nm, what makes the material only useful for small molecules (not for proteins). These monoliths are commercially available by Merck GmbH under the brand Chromolith®. Recently also a method was developed to prepare silica monoliths in silica capillaries.[92]
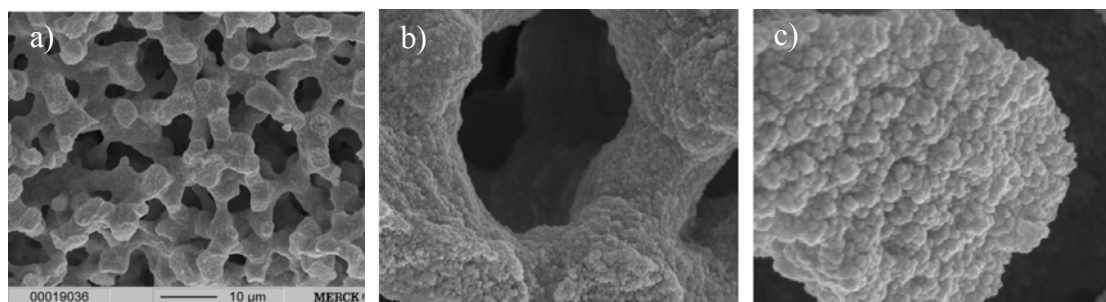
Fig 7 (a) SEM-picture of the typical porous structure of monolithic silica columns, **(b)** the macropores or throughpores and **(c)** the mesoporous structure of the silica skeleton (taken from ref 93).

2.2.4.3 Pillar array columns

One of Knox' important conclusions was that around h_{min} the contribution of the C-term is negligible and that the A-term dominates. Limitations in packing technology would prevent the further decrease of A and hence also h_{min}.[47-49] Knox stated that lower values of h_{min} could be obtained if the stationary phase would be made entirely regular. This was first put into practice by Regnier and coworkers in Quartz.[95-97] Even though they were working in EOF mode, it opened many old school researchers' eyes about the potential of micro-fabrication in pressure-driven chromatography. The presence of bifurcation channels at the inlet of the wide channel, allowed a nice definition of plugs coming from a narrow capillary. Kutter and co-workers combined this system with a UV-Vis absorption cell with a detection limit of the order of 10 μM.[98-99] Desmet and co-workers began to contemplate about the ideal pillar structure, internal and external porosity and practical limitations of the format when implying this system on pressure-driven chromatography, the area where more significant advantages would arise. Performing a number of computational fluid dynamics (CFD) simulations, reduced plate heights as small as 0.5 have been predicted for a retained solute (zone retention factor k''=2, D_s=5 10^{-10} m^2/s) in a channel with an external porosity of 0.4, i.e. easily 5 times smaller than the currently available silica monoliths.[100-102] On the other hand, the separation impedence number was found to be of the order of E=200-300 depending on the pillar shape, which is about 10 times smaller than the best possible packed bed columns. Vervoort et al. showed that even though the sidewall area makes up only a negligible fraction, the sidewall region can lead to a strong increase of the band broadening in pressure-driven 2D etched columns. The effect can easily be a factor 2-4 in the u $\gg$ u_{opt} range, when a non-ideal distance is provided between the pillar adjacent to the sidewall and the sidewall itself. When this distance is exactly 0.15 times the cylindrical pillar diameter (external porosity 0.4), the flow resistance at the sidewall zone and at the central zone of the channel is identical and hence no sidewall induced band broadening occurs.[103]
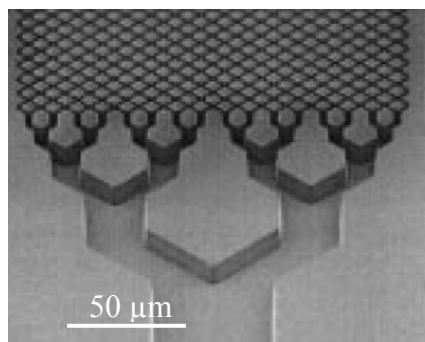
Fig. 8. Microfabricated inlet splitter of the micro-fabricated device proposed by Regnier and co-workers. The splitter has a constant cross-sectional area (taken from ref. 95).

In 2006 de Pra et al. of the University of Amsterdam performed (in collaboration with the MESA+ Institute also based in The Netherlands and the Free University of Brussels) band broadening experiments on columns with non-porous silicon pillars under non retaining conditions,[104] achieving a value of h_{min}=0.2, very close to what was predicted by Gzil et al.[100] In this paper, it was also shown experimentally that slight flow resistance differences between the sidewall-zone and the central part of the channel give an important dispersion source.

This thesis will build on this work and focus on the improvement of these pillar array columns in order to arrive at LC columns which are competitive with commercially available systems.

2.2.4.4 Evaluation of the performance of different column formats

During the last two decades, many new and innovative LC formats, such as the polymer and silica monoliths and the pillar array columns, have emerged. In the old days, when particulate columns were the only available format, different columns could be simply evaluated on the basis of the plate heights near the minimum and the C-term dominated region of the van Deemter curve. With the new arising formats, having different shapes and flow resistances, plate height information only no longer suffices, because the ability to apply larger flow rates for a certain column length and pressure drop is not accounted for.

Switching to reduced coordinates does not solve the problem, because it is impossible to identify a general reference length for which two formats can coincide on the same reduced plate height curve.

It is custom to combine both H and the column permeability K_v in the separation impedance number:

$$E_0 = \frac{H^2}{K_v} = h^2\phi \qquad (27)$$

Even though this approach omits the need for a common characteristic reference length, it does not really allow a relevant comparison. As for example two packed beds with particles of for example 2 and 5 μm have the same E_0 number, but need a completely different time to achieve for example 20,000 plates, it is obvious that the kinetic character is not exposed by E_0.[105]

For a regular or periodically structured columns format it is possible to identify characteristic feature dimensions to completely describe the column architecture. When two columns can be made to perfectly overlap by rescaling their characteristic feature sizes they are called to be self-similar. It is well understood that members of the same self-similar structures group (SSG) are expected to have the same A', B' and C'-constants in the reduced Knox equation, when the reduction occurs on the basis of any characteristic dimension (d_{ref}) of the geometry. Based on:[106]

$$t_R = t_0(1+k')$$
(28)

$$\text{with } t_0 = \frac{NH}{u_0}.$$
(29)

According to Eq. (15) the achievable mobile phase velocity can be written as:

$$u_0 H = \frac{\Delta P}{\eta} \frac{K_v}{N}$$
(30)

Eqs. (29) and (30) are linked via the Knox equation:

$$H = A'u_0^n + \frac{B'}{u_0} + C'u_0.$$
(31)

The number of plates can then be rewritten as:

$$N = \left(\frac{\Delta P}{\eta}\right)\left[\frac{K_v}{u_0 H}\right]_{exp},$$
(32)

inserting this in Eq. (29), yields:

$$t_0 = \left(\frac{\Delta P}{\eta}\right)\left[\frac{K_v}{u_0^2}\right]_{exp}$$ (33)

Plotting t_0 versus N, one can easily determine the required time to achieve a number of plates N.

To compare the intrinsic performance of different formats, all systems should be evaluated for the same ΔP, independently of the actual applied experimental pressure drop. An obvious value is the operating limit of a commercial HPLC instrument, i.e. 400 bar.

Dividing now Eq. (33) by the square of Eq. (32) yields:

$$\frac{t_0}{N^2} = \left(\frac{\eta}{\Delta P}\right)\left[\frac{H^2}{K_v}\right]_{exp} = \left(\frac{\eta}{\Delta P}\right)[E_0]_{exp}$$ (34)

Eq. (34) shows that the t_0/N^2 is proportional to E_0, which can be considered as a dimensionless analysis time. A plot of $E_0=H^2/K_v$ versus N hence displays the same type of information as the (N,t_0)-plot. The y-axis is in both cases a direct measure for the difference in time between columns in comparison.

In the (N, E_0) plot, the minimum of the van Deemter curve is directly visualized, as can be understood by Eq. 27 ($E_0 \sim H^2$). The minimum also reveals optimal particle or support feature size to obtain a given number of plates in the shortest time. H_{min} is translated here into N_{opt}, which can be considered as the plate number for which the support reaches the best kinetic performance/pressure cost ratio. When comparing columns that have different retention properties, N and E should be replaced by respectively

$$N_{eff} = N\frac{k'^2}{(1+k')^2} \quad \text{and}$$ (35)

$$E_{eff} = E_0\frac{(1+k')^5}{k'^4}$$ (36)

This approach then allows a fair comparison between column structures of different shapes and formats. In Fig. 9 some packed beds with different particles are being compared with
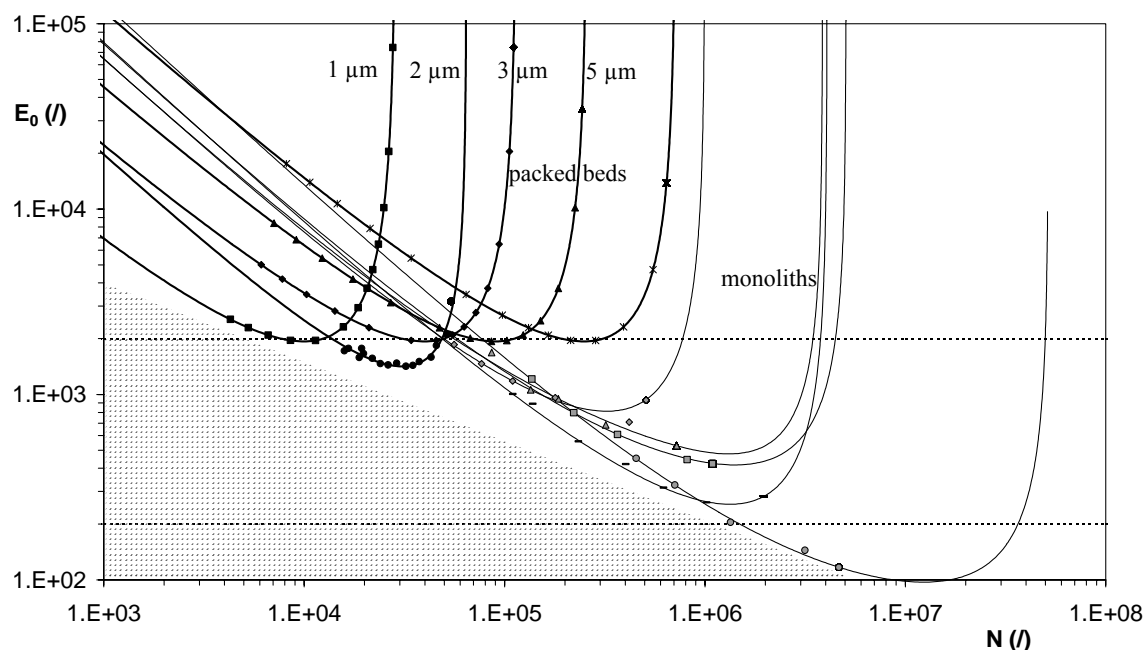
Fig. 9 (N, E_0) plot assuming $\Delta P=400$ bar of the performance of some typical packed beds (PB-1μm, ■ ; PB-2$μm$, ◆ ; PB-3 $μm$, ▲; PB-5 $μm$, ✳, UHPLC 1μm[107] and silica monoliths (MS(50)-A, ○ ; MS(50)-B, ▢; MS(50)-C, △; MS(50)-D;[108] ◇, MS-PTFE(B),[109] -, taken from the literature. The respective monoliths have following domain and pore sizes: MS(50)-A, $d_{dom}=10$ $μm$, $d_{por}=8$ $μm$; MS(50)-B, $d_{dom}= 4.2$ $μm$, $d_{por}=2.8$ $μm$; MS(50)-C, $d_{dom}=3.3$ $μm$, $d_{por}=2.2$ $μm$; MS(50)-D, $d_{dom}=3$ $μm$, $d_{por}=2$ $μm$; MS-PTFE(B), $d_{dom}=3.81$ $μm$, $d_{por}=2.23$ μm.

some silica monoliths with different domain and pore sizes. Packed beds with particle sizes below or equal to 3 μm are clearly superior in the N<50,000 range, whereas silica monoliths are preferable in the higher plate number range.

Kinetic plots are also interesting to investigate the effect of an increased pressure drop, as currently pursued in UHPLC. In order to represent the influence of the pressure, the E_0 number should be replaced by t_0/N^2. In Fig. 10 pressure values up to 4000 bar are depicted in such a plot. The increase in pressure results in a shift of the N_{opt} values to a higher value and at the same time all t_0 times decrease. It is clear (see grey zone in Figs. 8-9) that the use of high pressure is a possible strategy to enter in a region that is currently not commercially available (the so-called 'forbidden region').[106]
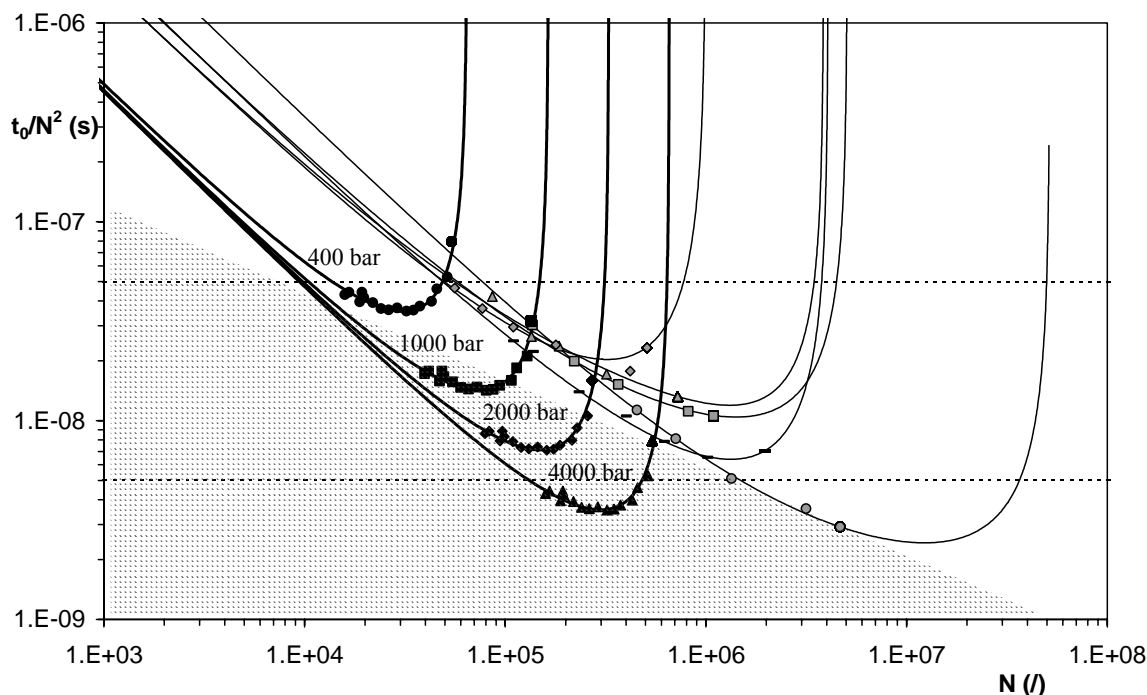
Fig. 10 (N, t_0/N^2) plot of the same silica monolith data as in Fig. 9 (taken at $\Delta P=400$ bar, same symbol code as above) and $d_p=1$ μm nonporous particle UHPLC data respectively $\Delta P=400$, 1000, 2000, and 4000 bar.[106]

2.3 Integration of functionalities

2.3.1 Injection

Ideally, an injector should be able to insert sharply delimited plugs of a desired volume in a reproducible way. As chip-volumes are typically of the order or smaller than dead-volumes of connection pieces, on-chip injection is mostly a necessity. Described mechanisms to inject are either pressure-, electrically- or shear- driven. Electrical systems are easy to implement and do not require any valves to inject, which is an important reason for the prevalence of electrically-driven chip-devices.[1] An important constraint is however the necessity for a non-conducting substrate (hence excluding silicon) and also the absence of any built-up pressures present in the system, hence prohibiting for example a pressure–driven mobile phase propulsion. Shear-driven injections have been described in combination with shear-driven chromatography.[54-56] Very small (pl) plugs with high aspect ratios have been successfully injected, but it appears only feasible to be used in shear-driven chromatography given the typical movable wall (OT) format that is needed. When applying a pressure to drive the mobile phase, the wall would detach from the complementary substrate.

For a pressure-induced injector, valves are necessary to control the sample plug volume. Extensive research has been carried out during the last years on the development of micro-

scale valves. The fabrication is cumbersome and the valves developed so far are not able to withstand reasonable pressures. Also, the usable material is limited because many candidate materials tend to swell or dissolve when coming into contact with the solvents used to perform chromatographic separations. Therefore, passive injector microstructures are preferred, typically a cross injector (the channel intersects the separation channel at one position) or a twin-T injector (2 channels share a common length).[1] For the sake of detection when working in UV-Vis absorption mode, it is beneficial to fabricate channels with high aspect ratio's to increase the path length of the light crossing the channel. When using one of the above described passive injection systems, the sample will diffuse into the separation channel when crossing the channel to define the plug. This leads to asymetric peaks, which will partially degrade the column's performance. A smart solution to this problem has been put forward by Blom et al., which was used in the fabrication procedure for their hydrodynamic chromatography (HDC) device. The authors fabricated 100 μm deep injection channels to allow the sample to cross the separation channel fast, before the injection zone (1 μm deep) was being filled with sample.[110-111]

2.3.2 Detection with UV-Vis absorbance

2.3.2.1 Conventional approach

The vast majority of HPLC analyses are carried out with the UV-Vis absorbance detector, that is typically sensitive for a wavelength range between 190-800 nm. Many organic compounds have absorption bands in this region. The linear range of UV-vis detectors goes to about 1 or 2 absorbance units, corresponding to a linear dynamic range of 10^4 to 10^5. UV-Vis detectors either use a low-pressure Hg lamp as the light source (useful at around 254 nm) or a deuterium discharge lamp (used for the 200-350 nm range). Multiwavelength detection can also be applied using photodiode array type detectors. The sensitivity is typically less that a few ng when no disturbances in temperature or flow rate occur. For solutes that have no absorption bands in this region, a chemical derivatization procedure can be applied before the injection or the separation.

While UV-Vis absorbance is one of the most popular detection modes for macro-scale chromatography, it has not been used as extensively for microchip separations. Limiting factors include the reduced optical path lengths and sample volumes, which can impact detection sensitivity.

The geometrical extent of the detection cell generates a plate height contribution according to:

$$H_{det} = \frac{w_{det}^2}{12} \frac{1}{L_{tot}},$$

(37)

with w_{det} the width of the detection area for a detection cell with the same dimensions as the separation channel (length L_{tot}).[42-44]

2.3.2.2 Integrated waveguides

Because the typical chip-system requires plug volumes of the order of nl, large restraints are set on the connection of the system towards a detector. The currently commercially available connections from chip-formats to an external tubing present dead volumes on the order of µl. This connection leads to a large dilution and accompanied loss in detection sensitivity, but it also partly deteriorates the separation. To anticipate this, a logical choice is to integrate the detection cell on the chip at the channel area, hence allowing to monitor the separation in the channel itself without any off-channel effects. A logical detection method is UV-Vis-absorbance. Not only is this the most prevalent method in macro-scale liquid chromatography, the method is also relatively easy to implement in such a way that the the consistency of the peaks is not compromised due to the detection method. During the last decade, innovating fabrication schemes have been conceived to guide light through micro-machined waveguides one side of the channel and collect the transmitted light in another waveguide at the other side of the channel.[98-99] As the only requirement for light to stay confined in the waveguide core-material (besides the existence of a smooth waveguide interface and transparency of the material for the applied wavelength) is that the refractive index of the surrounding cladding layer is about a percentage larger, a wide spectrum of usable materials is at hand. The light can only propagate in discrete modes (described by Maxwell's equations) and the number of modes decreases with the size of the waveguide until only 1 mode exists (when the size of the core is around the size of the wavelength). In the single mode case, light propagates through internal reflections at the core-cladding interfaces as described by Snell's Law.

Well established deposition methods such as plasma enhanced chemical vapour deposition (PECVD) and low pressure chemical vapour deposition (LPCVD) of Si_pO_q or $Si_pO_qN_r$ can be used to generate both the core material and the cladding material. The difference in refractive index is provided by simply changing the feed gasses and hence the values of p,q and r that determine the composition of the transparent material.[112] In some specific cases (to satisfy

specific light transmittance demands) the material can also be nitrogen or germanium doped to provide the refraction index contrast. Also (cheap) polymers can be used for this purpose. A sandwiched SU8 layer between two glass plates has been shown to efficiently guide light, but also polymer stacking schemes are conceivable.[113] Interesting materials in terms of transparency and thermal stability are silicon resins,[114] deuterated polyflouromethacrylate (d-PFMA)[115] and various fluorinated copolymers.[116] These materials can be applied by spin-coating and can be patterned by reactive ion etching.

In order to increase the path length (and detection sensitivity) if the application prohibits the use of wide channels, the detection cell can be a U cell[117-121] where the plug is locally elongated and the light can be sent then across this elongated zone.

As light is leaving the light delivering waveguide, not all the light will follow the axis line of the waveguide due to the occurrence of stray radiation. This effect occurs at light interface boundaries and is a consequence of the non-collimated nature of the light there. Very recently, a diverging lens was implemented in PDMS in front of a fibre to collimate the light leaving the waveguide.[122]

The positioning of such a lens with respect to the light delivering element can be easily calculated using: $f = n_1 R / (n_2 - n_1)$, with n_1 and n_2 the respective refractive indices of the two materials, R the radius of the lens and f the focal length of the plano-convex lens.

This resulted in a reduction of the stray radiation from 31.6 % to 3.8 %, allowing a detection limit of 1.2 µM for fluorescein.

Symbols

K	partition coefficient (/)
C_s	component concentration in the stationary phase (mol/m^3)
C_m	component concentration in the mobile phase (mol/m^3)
k'	phase retention coefficient (/)
L	column length (m)
N	number of theoretical plates (/)
Q	obstruction factor
t_r	residence time of a retained comonent (s)
t_0	residence time of a non-retained component (s)
u_0	mobile phase velocity (m/s)
H	height of a theoretical plate (m)
σ_x	spatial peak standard deviation at position x (m)
$\sigma_{x,0}$	initial spatial peak standard deviation (m)
σ_t	time-based peak standard deviation at time t (s)
$\sigma_{t,0}$	time-based initial peak standard deviation (s)
d_p	pillar or particle diameter
λ	geometrical constant in the A term of the van Deemter equation (/, Eq. 8)

D_m molecular diffusion coefficient (m^2/s)
h   reduced plate height (/)
h_{min} minimal reduced plate height
ν   reduced mobile phase velocity (/)
K_v Darcy permeability (m^2)
η   dynamic viscosity (kg/ms)
Φ   flow resistance (/)
E   separation impedance (/)
R_s resolution (/)
ζ   zeta potential (V)
ε_0 permeability of vacuum (C^2/N.m)
ε_r permeability of medium (C^2/N.m)
ΔV   voltage gradient (V)
δ   double layer thickness (m)
T   temperature (K)
C_s ionic strength (mol/m^3)
e_0 elementary charge unit (C)
N_a Avogadro's number (mol^{-1})
U_{eof} electro-osmotic flow generated velocity (m/s)
ΔP   pressure drop (N/m^2)
k''   zone retention coefficient (/)
H_{det} plate height contribution due to detection (m)
w_{det} width of the detection area (m)

Abbreviations

LC   liquid chromatography
CD   critical dimension
RET   resolution-enhancement techniques
NA   numerical aperture
DUV   deep-uv
RIE   reactive ion etching
OT   open tubular
SDC   shear-driven chromatography
EOF   electro-osmotic flow
EDL   electrical double layer
SSG   self-similar structures group

References

1.   Kutter, J. P.; Fintschenko, Y. *Separation Methods in Microanalytical Systems*, Taylor and Francis, Boca Raton, 2006.
2.   Quiram, D.J.; Schmidt, MA.; Mills, P.L.; Ryley, J.F.; Wetzel, M.D.; Kraus, D.J.; Jensen, K.F. *Ind. Eng. Chem. Res.* **2007**, *46*, 8319-8335.
3.   Terry, S.C.; Jerman, J.H.; Angell, *J.B. IEEE Trans. Electron. Devices* **1979**, *ED-26*, 1880.
4.   Bassous, E.; Taub, H.H. ;Kuhn, L. *Appl. Phys. Lett.* **1977**, *31*, 135.

5.   Van de Pol, F.C.M.; Van Lintel, H.T.G.; Elwenspoek, M.; Fluitman, J.H.J. *Sens. Actuators A*, **1990**, *21*, 198.

6.   Shoji, S.; Esashi, M.; Matsuo, T. *Sens. Actuators* **1988**, *14*, 101.

7.   Göpel, W.; Hesse, J.; Zemel, J.M.L., *Sensors-A Comprehensive Survey 2*, Wiley-VCH, Weinheim, 1991.

8.   Manz, A.; Miyahara, Y.; Watanebe, Y.; Miyage, H.; Sato, K. *Sensors and Actuators B* **1990**, *1*, 249-255

9.   Manz, A.; Graber, N., Widmer, H.M. *Sensors and Actuators B* **1991**, *1*, 244-248.

10.   Tokeshi, M.; Minagawa, T.; Kitamori, T. *Anal. Chem.* **2001**, *72*, 1711-1714.

11.   Fluri, K.; Fitzpatrick, G.; Chiem, N.; Harrison, D. J. Anal. Chem. **1996**, *68*, 4285-4290.

12.   Mao, X.; Luo, Y.; Dai, Z.; Wang, K.; Du, Y.; Lin, B. *Anal. Chem.* **2004**, *76*, 6941-6947.

13.   Neue, U.D., *HPLC Columns: Theory, Technology, and Practice*, John Wiley & Sons, New York, 1997.

14.   Madou, M., *Fundamentals of Microfabrication*, CRC Press, London, 1997.

15.   Elwenspoek, M.; Jansen, H., *Silicon Micromachining*, Cambridge University Press, 1998

16.   Torres, C.M.S., *Alternative Lithography-Unleasing the Potentials of Nanolithography*, Kluwer, Ottawa, 2003.

17.   Smith; H.I., *Superlattices and Microstructures* **1986**, *2*, 129-142.

18.   Scheer, H.-C.; Schulz, H. *Microelectronic Eng.* **2001** ,*56*, 311-332.

19.   Lebib, A.; Chen, Y.; Bourneix, J.; Carcenac, F.; Cambril, E.; Coraud, L. ; Launois, H. Bailey, T; Choi, B.J; Colburn, M.; Meissl., M.; Shaya, S.; *Microelectronic Eng.* **1999**, *46*, 319-322.

20.   Ekerdt, J.G.; Sreenivasan, S.V.;Wilson, C.G. *J. Vac.Sci. Technol.* B 2000, **18,** 3572-3577.

21.   Resnick, D.J.; Screenivasan, S.V.; Wilson, C.G. *Materials Today* **2005**, *8*, 34-42.

22.   Vratzov, B.; Fuchs, A.; Lemme; M., Henschel; W.; Kurz, H.l, *J. Vac. Sci. Technol.* **2003**, *21*, 2760-2764.

23.   Tjerkstra, R.W.; Gardeniers, J.G.E.; Kelly, J.J.; van den Berg, A. *JMEMS* **2000** *9*, 495-501.

24.   Tjerkstra, R.W.; De Boer, M.; Berenschot, E.; Gardeniers, J.G.E.; van den Berg, A. Elwenspoek, M.C. *Electrochim. Act.* **1997**, *42*, 3399-3406.

25.   Tjerkstra, R.W.; de Boer, M.; Berenschot, E.; Gardeniers, J.G.E.; van den Berg, A. Elwenspoek, M.C. *Electrochimica acta* **1997**, *42*, 3399-3406.

26.   Tjerkstra, W., Isotropic Etching of Silicon in Fluoride Containing Solutions as a Tool for Micromachining, Ph.D. thesis, University of Twente, Enschede, The Netherlands ISBN 90-36513286.

27.   Uhlir, A. *Bell syst. Techn. J*. **1956**, *35*, 333.

28.   Archer, R.J. *J. Phys. Chem. Solids* **1960**, *14*, 104.

29.   Gee, A. *J. Electroch. Soc.* **1960**, *107*, 787.

30.   Canham, L.T. *J. Appl. Phys. Lett.* **1990**, *57*, 1096.

31.   Canhan, L.; Malvern, D., *Properties of Porous Si*, Inspec, London, 1997.

32.   Sarathy; J. et al., Appl. Phys. Lett. **1992**, *60*, 1532.

33.   George, T. et al., Appl. Phys. Lett. **1992**, *60*, 2359.

34.   Hérino, R.; Bomchil, G.; Barla, K.; Bertrand, C.; Ginoux, J.L. *J. Electrochem. Soc.* **1987**, 134, 1994.

35.   Tswett, M.S. Berichte *der Deutschen Gesellschaft* **1906**, *24*, 316-23.

36.   Ettre, L.L. *LCGC Magazine* **2003**, *21*, 458-467.
37.   Martin, A.J.P.; Synge, R.L.M. *Biochem. J.* **1941**, *35,* 91.
38.   Horvath, C. In *Chromatography a century of discovery 1900-2000*; Gehrke, C.W.; Wixom, R.L.; Bayer, E., Ed.; Elsevier: Amsterdam, 2003; pp 237-248.
39.   Huber, J.F.K. *J. Chromatogr*. **1969**, *7*, 86.
40.   Kirkland , J.J. *J. Chromatogr. Sci*. **1969**, *7*, 7.
41.   K.K. Unger, R. Skudas, M.. Schulte, J. Chromatogr. A, 2008, doi:10.1016j.chroma.2007.11.118
42.   Braam, W.G.M. *Scheidingsmethoden Chromatografie*; Wolf: Noordhoff, Groningen, 1992.
43.   Robards, K.; Haddad, P.R.; Jackson, P.E. *Principles and practice of modern chromatographic methods*, Academic press, New York, 1994.
44.   Snyder, L.; Kirkland, J.J. *Modern liquid chromatography*, ACS, Washington,1979.
45.   Martin, A.J.P.; Synge, R.L.M. *Biochem. J.* **1941**, *35,* 91.
46.   van Deemter J.J.; Zuiderweg, F.J.; Klinkenberg A. *Chem. Eng. Sci*. **1956**, 5, 271.
47.   Giddings, J.C. *Dynamics of Chromatography Part* , Marcel Dekker: New York, 1965.
48.   Knox, J.H.; Parcher, J. *Anal. Chem*. **1969**, *41*, 1599.
49.   Done, J.N.; Knox, J.H. *J.Chromatogr. Sci.* **1972**, *10*, 606.
50.   Done, J.N.; Kennedy, G.J.; Knox, J.H., *Gas Chromatography*., Applied Science Publishers, London, 1973.
51.   Barz, D.P.J., Ehrhard. P. *Lab Chip* **2005**, *5*, 949-958.
52.   Stol, R. PhD Thesis, University of Amsterdam, Amsterdam, The Netherlands, 2002.
53.   Rice, C.L.; Whitehead, R. *J. Phys. Chem*. **1965**, *69*, 4017.
54.   Desmet, G.; Baron, G. V. *J. Chromatogr. A* **1999**, *855*, 57-70.
55.   Desmet, G.; Baron, G. V. *J. Chromatogr. A* **2000**, 867, 23-43.
56.   Desmet, G.; Vervoort, N.; Clicq, D. Baron, G. V. *J. Chromatogr. A* **2001**, *924*, 111-122.
57.   MacNair, J.E.; Lewis, K.C.; Jorgenson, J.W. *Anal. Chem.* **1997**, *69*, 461-467.
58.   MacNair, J.E.; Patel, K.D.; Jorgenson, J.W. *Anal. Chem.* **1999**, *71*, 700-708.
59.   Tolley, L.T.; Jorgenson, J.W.; Moseley, M.A. *Anal. Chem.* **2001**, *73*, 2985-2991.
60.   http://www.agilent.com
61.   Greibrokk, T.; Andersen, T. *J. Chromatogr. A*. **2003**, *1000*, 743-755.
62.   Chen, H.; Horvath, Cs. *J. Chromatogr. A*. **1995**, *705,* 3-20.
63.   Vanhoenacker, G.; Sandra, P. *J. Sep. Sci.* **2006**, *29,* 1822-1835.
64.   Yan, B.; Zhao, J.; Brown, J.S.; Blackwell, J.; Carr, P. *Anal. Chem.* **2000**, *72*, 1253-1262.
65.   Poppe, H.; Kraak, J.C.; Huber, J.F.K.; van den Berg, J.H.M., *Chromatographia* **1991**, *14*, 515.
66.   Thompson, J.; Carr, P. *Anal. Chem.* **2002**, *74,* 1017.
67.   Kirkland, J.J., *Advances in chromatography*; Preston Technical Abstracts, Evanson,1967.
68.   Gehrke, C.W.; Wixofrm, R.L.; Bayer, E. *Chromatography a century of discovery 1900-2000*; Elsevier: Amsterdam, 2003.
69.   Jerkovich, A.D.; Mellors, J.S.; Jorgenson, J.W. *LCGC Magazine* **2003**, *21*, 600-610.
70.   Jorgenson, J.W.; Lukakcs, K.D. *J. Chromatogr.* **1981**, *218*, 209.
71.   Kirkland, J.J.; Truszkowski, F.A.; Dilks, Jr., C.H.; Engel, G.S. *J. Chromatogr.* **2000,** *890,* 1.
72.   Meyers, J.J. Liapis A.I. **1998**, *J. Chromatogr. A*, 827, 197
73.   Liapis, A.I. *J. Chromatogr. A* **1999**, *865*, 13.

74. J.J. Meyers et al., *J. Chromatogr. A* **2001**, *35*, 908.
75. Isseava, T. Kourganov, A. Unger, K. *J. Chromatogr. A* **1999**, 846, 13-23.
76. Majors, R.E. *American Laboratory* **2003**, *10*, 46-54.
77. Patel, K.D.; Jerkovich, A.D.; Link, J.C.; Jorgenson, J.W. *Anal.Chem.* **2004**, *76*, 5777-5786.
78. Svec, F.; Fréchet, J.M.J. *Anal. Chem.* **1992**, *64*, 820.
79. Roper, D.K.; Lightfoot, E.N. *J. Chromatogr.A* **1995,** *702,* 3.
80. Kennedy, J.F.; Paterson, M. *Polym. Int.* **1993,** *32,* 71.
81. Yang, Y.; Velayudhan, C.M.; Landish, C.M.; Landish, M.R. *J. Chromatogr.A* **1992,** *598,* 169.
82. Hjérten, S.; Liao, J-L.; Zhang, R. *J. Chromatogr.* **1989,** *473,* 273.
83. Ross, W.D.; Jefferson, R.T. *J. Chromatogr. Sci.* **1970,** *8,* 386.
84. Kubin, M.; Spacek, P.; Chromecek, R. *Collect. Czech. Chem. Commun.* **1967,** *32,* 3881.
85. Hjérten, S.; Liao, J-L.; Zhang, R. *J. Chromatogr.* **1989,** *473,* 273.
86. Xie, S.; Svec, F.; Fréchet, J.M.J. *J. Chromatogr. A* **1997**, *753*, 227-234.
87. Xie, S. *et al. J. Chromatogr. A* **1999,** *865,* 169.
88. Premstaller, A.; Oberacher,H.; Huber, C.C. *Anal. Chem.* **2000**, *72*, 4386.
89. Vervoort, N. *Novel support structures for liquid chromatography*; Dissertation, Vrije Universiteit Brussel, 2004.
90. Nakanishi, K.; Soga, N. *J. Am. Ceram. Soc.* **1991,** *74*, 2518.
91. Nakanishi, K.; Soga, N. *J. Non-Cryst. Sol.* **1992**, *139*, 1–13.
92. Nakanishi, K. Journal of the Ceramic Society of Japan **2007**, *115*, 169-175.
93. Ref Cabrera, K. *J. Sep. Sci.* **2004**, *27*, 843–852
94. Minakuchi. H.; Nakanishi, K.; Soga, N.; Ishizuka, N.; Tanaka, N. *J. Chromatogr. A* **1998,** *797*, 121-131.
95. He, B.; Tait N.; Regnier, F.E. *Anal. Chem.* **1998**, *70*, 3790-3797
96. He, B.; Ji, J.; Regnier, F. *J. Chromatogr. A.* **1999**, *853*, 257-262.
97. Slentz, B.E.; Penner, N.A.; Lugowska E.; Regnier, F. *J. Sep. Sci.* **2002**, *25*, 1011-1018.
98. Mogensen, K. B.; Petersen, N. J.; Hu¨bner, J.; Kutter, J. P. *Electrophoresis* **2001**, *22*, 3930-3938.
99. Petersen, N. J.; Mogensen, K. B.; Kutter, J. P. *Electrophoresis* **2002**, *23*, 3528-3536.
100. Gzil, P.; Vervoort, N.; Baron G.V.; Gert Desmet, *Anal. Chem.* **2004**, *76*, 6707-6718.
101. De Smet, J.; Gzil, P.; Vervoort, N.; Verelst, H.; Baron, G. V.; Desmet G. *Anal. Chem.* **2004,** *76*, 3716-3726
102. De Smet, J.; Gzil, P.; Vervoort, N.; Verelst, H. Baron, G.V.; Desmet; G. *J. Chromatogr. A,* **2005**, *1073*, 43-51.
103. Vervoort, N.; Billen, J.; Gzil, P.; Baron, G.V.; Desmet, G., *Anal. Chem.* **2004**, *76*, 4501-4507.
104. De Pra, M.; Kok, W.Th.; Gardeniers, J.G.E.; Desmet, G.; Eeltink, S.; van Nieuwekasteele, J.W.; Schoenmakers, P.J., *Anal.Chem.* **2006**, *78*, 6519-6525.
105. Desmet, G.; Clicq, D.; Nguyen, D. T.-T.; Guillarme, D.; Rudaz, S.; Veuthey, J.-L.; Vervoort, N.; Torok, G.; Cabooter, D.; Gzil, P. *Anal. Chem.* **2006**, *78*, 2150-2162.
106. Desmet, G.; Clicq, D.; Gzil, P. *Anal. Chem.* **2005**, *77*, 4058-4070.
107. Jerkovich, A. D.; Mellors, J. S.; Jorgenson, J. W. *LC-GC Eur.* **2003**, *16* (6a), 20-23.
108. Motokawa, M.; Kobayashi, H.; Ishizuka, N.; Minakuchi, H.; Nakanishi, K.; Jinnai, H.; Hosoya, K.; Ikegami, T.; Tanaka, N *J. Chromatogr. A* **2002**, *961*, 53-63.

109. Tanaka, N.; Kobayashi, H.; Ishizuka, N.; Minakuchi, H.; Nakanishi, K.; Hosoya, K.; Ikegami, T. *J. Chromatogr., A* **2002**, *965*, 35-49.

110. Blom, M.T.; Chmela, E.; Gardeniers, J.G.E.; Tijssen, R.; Elwenspoek, M.; van den Berg, A. *Sensors and Actuators B: Chemical* **2002**, *82*, 111-116.

111. Blom, M.T.; Chmela, E.; Oosterbroek, R.E.; Tijssen R.; van den Berg, A. *Anal. Chem.* **2003**, *75*, 6761-6768.

112. Hunsperger, R.G., *Integrated Optics-Theory and Technology*, Springer, Newark, 2002. 113 Balslev, S.; Jorgensen, A.M.; Bilenberg, B.; Mogensen, K.B.; Snakenborg, D.; Geschke, O.; Kutter, J.P.; Kristensen, A. *Lab Chip* **2006**, *2*, 213-217.

114. Watanabe, T.; Ooba, N.; Hayashida, S.; Kurihara, T., J*ournal of Lightwave technology* **1998**, 16, 1049-1055.

115. Yoshimura, R.; Hikita, M.; Tomaru, S.; Imamura, S. *Journal of Lightwave Technology* **1998**, *16*, 1030-1037.

116. Liang, J.; Toussaere, E.; Hierle, R.; Levenson, R. *Optical Materials* **1998**, *9*, 230-235.

117. Wang, T.; J.H. Aiken, Huie, C.W.; Hartwick; R.A., *Anal. Chem.* **1991**, *63*, 1372-1376.

118. Salimi-Moosavi, H.; Jiang, Y.; Lester, L.; McKinnon, G.; Harrison, D. J. *Electrophoresis* **2000**, *21*, 1291-1299.

119. Verpoorte, E.; Manz, A.; Lüdi, H.; Bruno, A. E.; Maystre, F.; Krattiger, B.; Widmer, H. M.; van der Schoot, B. H.; de Rooij, N. F. *Sens. Actuators, B* **1992**, *6*, 66-70.

120. Mainka, A.; Bächmann, K.J., *J. Chromatogr. A* **1997**, *767*, 241-247.

121. Liang, Z.; Chiem, N.; Ocvirk, G.; Tang, T.; Fluri, K.; Harrison, D. J. *Anal. Chem.* **1996**, *68*, 1040-1046.

122. Ro, K.K.; Lim, K.; Shim, B.C., Hahn; J. H., *Anal. Chem.* **2005**, *77*, 5160-5166.

Chapter 3: An automated injection system for sub-micron sized channels used in shear-driven-chromatography

This chapter has been published as:

An Automated Injection System for Sub-micron Sized Channels Used in Shear-driven-chromatography, De Malsche, W., Clicq, D., Eghbali, H., Fekete, V. Gardeniers, H. and Desmet, G., Lab Chip **2006**, *6, 1322-1327.*

3.1 Abstract

This chapter describes a method to automatically and reproducibly inject sharply delimited sample plugs in the shallow (i.e., sub-micron) channels typically used in shear driven chromatography. The formation of asymmetric plugs, which typically occurs during loading of the sample in wide channels, is circumvented by etching a slit in the middle of the channel that is connected to a micro-well and a vacuum system with syringes for the supply of both the analyte and the mobile phase. The design of the injection slit was supported by a series of CFD simulations to optimize its shape and that of the corresponding injection well. The system was intensively tested experimentally and showed good reproducibility, both for the width and the area of the injected peaks (relative standard deviations are max. 4 and 6 %, respectively). The concentration of the injected plug was found to be approximately 80 % of the original sample concentration. It was also observed that with the current setup the lower limit of the peak width was about 120 μm. This is a consequence of the fact that the peak width originating from the convection filling step becomes negligible to the contribution of diffusion during the filling and flushing time. Being fully automated and perfectly closed, the presently proposed injection system also paves the way to integrate other functionalities in shear driven chromatography, i.e. gradient elution and parallelization.

3.2 Introduction

Our group has previously reported on the feasibility of shear driven chromatography (SDC)[1-3]. The operation principle consists of pressing a substrate with an etched groove against a smooth glass plate, thus creating a channel. Without any pressure drop limitation, a flow in the channel is generated by simply moving one of the 2 substrates, which allows a unique access in the so-called forbidden regions that exist in other LC

systems. Due to the fast mass transfer characteristics in these channels, extremely low plate heights can be generated in very short times. Recently, a rotational variant of the approach has also been proposed[4]. In the SDC experiments in sub-micron channels described thus far, a semi-automated injection procedure was used to insert the sample inside the channels[5-6]. This method consists of manually applying the sample just in front of the channel inlet, after which a plug is injected by moving the wall for a predetermined distance using a high-precision translation stage. Subsequently flushing the pre-channel zone with fresh mobile phase then removes the non-entered sample. This method however presents some drawbacks: since the channel entrance extends to the edge of the chip, the definition of plugs is highly dependent on the dicing quality of the substrate. Furthermore, the method is slow and thus gives rise to peak broadening by diffusion already occurring during injection. The reproducibility is poor because of uncontrolled dilution and the manual handling. The fact that the sample is deposited in the open space before the channel substrate brings along contamination risks and possible changes in sample composition because of partial evaporation of the most volatile sample components. Finally, the method does not allow gradient elution, a functionality that is indispensable to perform complex separations.

In general, the definition of sharply delineated small plugs is a difficult problem in on-chip chromatography. The fact that injections are relatively straightforward to perform in electro-osmotic flow systems, in combination with electrokinetic stacking schemes, is one of the reasons for the success of electrically driven separation systems on a chip[7]. Electrokinetic pinching schemes have been shown to very efficiently prevent tailing and peak deformation[8-10]. Pinching is also possible using pressure-driven or vacuum-driven injections, a method that has been used in combination with capillary electrophoresis on a chip[11]. Another example of the use of pressure to define plugs in a channel is e.g. the work of Blom et al.[12-13] who designed a method using low resistance supply channels in a high resistance separation channel, in order to minimize the concentration gradient of the introduced plug over the channel width during sample loading. In the case of pressure-driven injections one can decrease injection times and therefore minimize diffusive band broadening by applying high pressures over low flow resistance sample inlets[14]. In the case of a shear-driven system, the application of high pressure injection flows running directly into the channel is not possible because the pressure would lift the top substrate of the channel. Typically a 0.5 bar normal load pressure is used to keep the separate

sandwich channel parts in close contact. This pressure is a trade-off between providing close contact at the interface between stationary and moving substrate and allowing the presence of a lubrication layer to avoid scratching and uncontrolled blocking. In the present study we take advantage of another feature of SDC to develop an automated injection scheme. Since SDC performs best in sub-micron depth channels, the times needed to equilibrate the liquid in the channel with a liquid brought into direct contact with this liquid are extremely short (50 µs as can be calculated from Einsteins' diffusion law and assuming d=300 nm and D_{mol}=7.96 × 10^{-10} m^2.s^{-1}):

$$t_{diff} = d^2/(2D_{mol}) \hspace{5cm} (1)$$

From this consideration, we have developed a new injection method using an etched inlet slit that enters the channel from the backside of the stationary substrate to bring the sample in direct contact with the liquid occupying the channel space. The slit is connected to a small micro-well that can be filled and emptied in a fast and automated manner. In this paper we will demonstrate that with this setup very narrow sample plugs can be injected within 1 s in a 300 nm deep separation channel, and discuss the factors that determine peak width. The basics of the injection procedure are shown in Fig. 1. The injection consists of the following steps: emptying the micro-well and injection slit, filling with analyte, injection of analyte in the channel by moving the substrate over a desired distance at a defined velocity, emptying the micro-well and injection slit, filling the well with mobile phase and finally translating the substrate to start the movement of the injected plug in the channel.

3.3 Computational fluid dynamics modelling of injection procedure

In order to study the feasibility of the injection procedure depicted in Figure 1, we have performed 2D fluidic simulations, using the Computational Fluid Dynamics (CFD) software package Fluent® (Fluent N.V., Belgium). The effect of different injection slit shapes and various channel configurations on peak width and concentration of introduced plugs was studied. For the depth of the channel a value of 1 µm was chosen. Only a part of the injection slit (10 µm high) and of the channel (70 µm long) was discretized in space using the grid generator Gambit® (Fluent N.V., Belgium). An injection time of 20 ms was set with a moving wall velocity of 1 mm.s^{-1}. Time steps of 1 ms were used to

describe the transient behaviour of the plugs. It was checked that refining the grid size and decreasing the time step had no effect on the velocity fields and the mass balances.

A computer simulation of the injection is shown in Fig. 1. Infinite mass transfer is assumed during loading, which corresponds to the use of a fast response syringe and vacuum system in combination with low-resistance supply channels. Unilateral diffusion during loading of the sample gives rise to slightly asymmetric plugs. This approximation of an infinite fast filling speed of the well leads to a linear relation between the injection time (or translated distance) and peak width, except for injection times smaller than 0.01 s where the linear flow profile can no longer be approximated by the average mobile phase velocity.[15]

In order to approximate the likely influence of the injection well shape on the acquired plug widths, simulations were performed for different slit configurations. Remarkably, no differences in peak shape occur when the shape of the slit is altered or when a dead zone or pre-channel is incorporated (see Fig. 2).
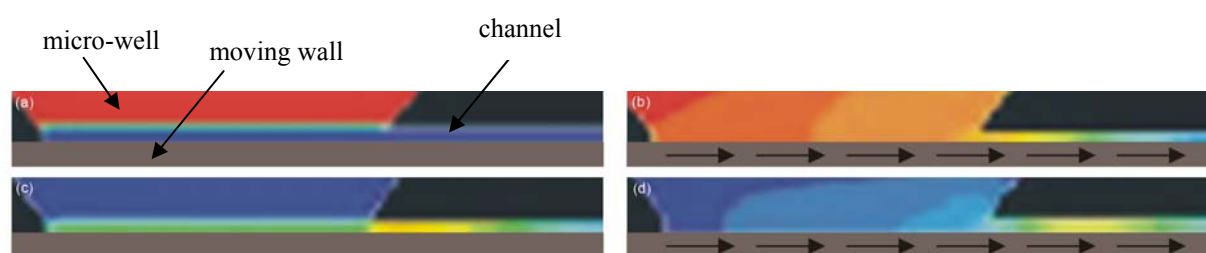
Fig. 1 CFD simulation of the different steps during injection: **a)** sample is loaded into the injection slit and micro-well; **b)** sample is injected into the channel by displacement of the moving wall at a distance further referred to as injection translation distance (see arrows), i.e. the lower part is moved to the right, here the injection translation distance imposes predominantly the defined peak width ; **c)** sample in the injection slit and micro-well is replaced by mobile phase; **d)** the injected plug is transported through the channel by restarting the motion of the movable wall. The color scale ranges from red for the original high, to deep blue for zero concentration of analyte.

This convinced us that one can simply use anisotropic etching of silicon in aqueous KOH solution, giving rise to an injection micro-well with sidewalls sloped at 55°. It turned out, however, that there is an effect on the maximum concentration and width of injected plugs, if the mobile phase cannot be aspirated completely from the bottom of the separation channel. This can occur when a polar solvent has enough affinity for the substrate material, such as silicon which has a native layer of silicon oxide.

3.4 Experimental

3.4.1 Chip design and microfabrication procedure

The process for the fabrication of the chip is depicted schematically in Fig. 3. A (100) silicon wafer with a diameter of 10 cm and a thickness of 1 mm was coated with 300 nm silicon-rich silicon nitride, with a standard low pressure chemical vapor deposition (LPCVD) process. At the backside of the wafer rectangular holes were etched in this coating, by reactive ion etching (RIE). Next, the exposed silicon was etched with 25 wt-% aqueous KOH to a depth of 850 μm. Spacers used to define the separation channels were subsequently fabricated by RIE etching of the silicon nitride layer at the front side of the wafer.
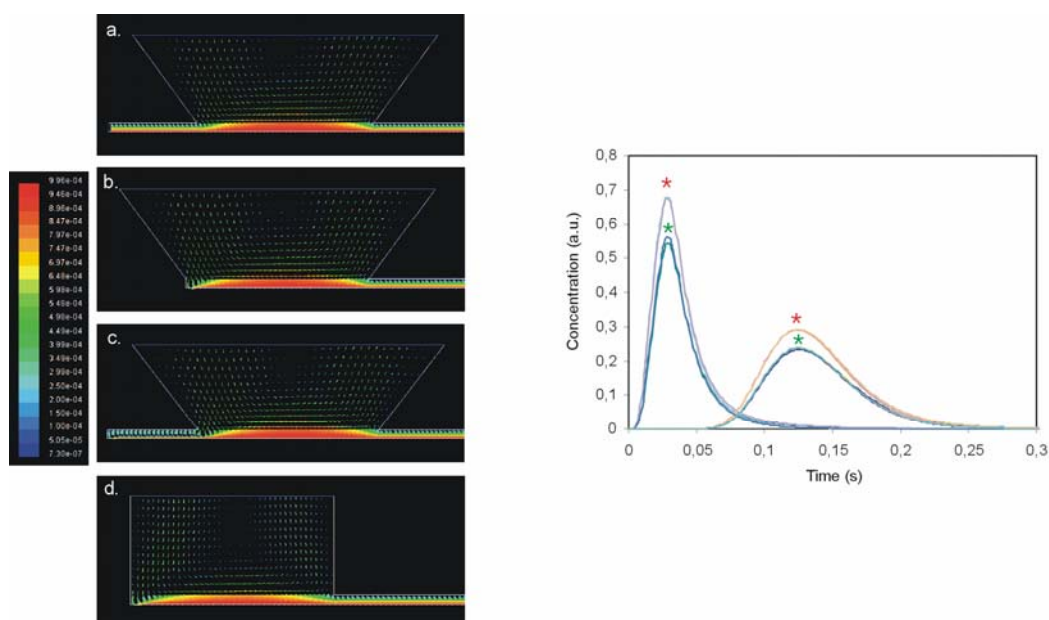
Fig. 2 Left: Flow profiles of different possible injection micro-well configurations. The pyramid-shape micro-well connects either behind the slit to a channel with continuous access to mobile phase **(a)**, is blocked precisely after the slit **(b)**, or connects to a dead-end channel **(c)**. In **(d)** the injection micro-well has a rectangular design and no extension. Right: Relative dye concentrations for the four different designs **a.** to **d.** at monitor planes situated 10 μm (left hand curves) and 60 μm (right hand curves) downstream of the injector in the separation channel. The curves with the lowest concentrations (*) arise from the assumption that the micro-well was completely replenished with buffer. In the higher concentration curves (*) it was assumed that an analyte layer with the thickness of the channel height remains at the bottom of the micro-well after washing. The curves for all four designs are indistinguishable, independent of whether or not a layer of analyte is assumed to remain in the micro-well.

Through-holes were made by Bosch-type deep reactive ion etching, in order to generate the injection slit. Finally, the wafer was diced in chips of 1 cm x 2 cm. Fig. 4b shows a typical example of one of the fabricated injection slits and sample/mobile phase micro-

well. In this particular case, a small spacer was left behind the injection slit. Without the spacer, the moving wall would essentially still drag liquid from the front end of the channel and not from the injection well itself. A 2 mm thick polymethylmethoxymetacrylate (PMMA) plate was milled with a high precision milling robot (M7 CNC, Datron, Germany) to define supply channels to the slit. Through holes were produced to connect the system to the sample and mobile phase inlet and to the vacuum system. The patterned silicon substrate and the milled PMMA block were then bonded at room temperature with epoxy glue as an intermediate layer.
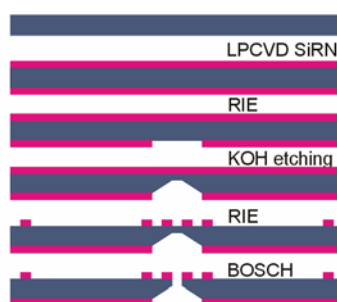
Fig. 3 Process scheme for the fabrication of the chip (not to scale). See text for details.

3.4.2 Injection system and injection procedure

Initially, a closed system was used to ensure that the well was empty before the sample or the mobile phase were introduced and to avoid dilution of the sample. It appeared however that the pressure originating from the syringes was too high to keep the movable substrate and the channel chip in close contact. This problem was solved by providing an opening to release the possible overpressure.

For the movable wall, an ultra-flat fused silica substrate(flatness λ/20, Photox Optical systems, UK) with a diameter of 5 cm was fixed in a holder which was mounted on a breadboard (M-IG 23-2, Newport B.V., The Netherlands) equipped with a linear displacement stage (M-TS100DC.5, Newport B.V.), a stepping motor (UE611CC, Newport B.V.) and a speed controller (MM4006, Newport B.V.) with a positioning accuracy of 0.5 μm. A channel was defined by pressing the silicon side of the chip on top of it at a pressure of 0.5 bar, firmly fixed in a holder to avoid undesired lateral movements. The PMMA side was connected via PEEK capillaries to an automated system of supply syringes and a vacuum pump (Fig. 4). The movements of the analyte and mobile phase syringes was actuated with stepping motors (respectively Minimotor

2036U024BK1155, 20/1 reductor, Faulhaber S.A., Belgium and M-060, Physik Instruments, Germany). This allowed an easy variation of the generated pressure, the injection distance, the velocity of the moving wall and the timing and duration of the different steps during the injection. The injection procedure consisted in emptying the injection slit and micro-well by use of a vacuum pump, filling both with analyte using a syringe, injecting the analyte in the separation channel by moving the substrate over a specific distance (which was varied, see results) at a velocity of 2 mm.s^{-1}, emptying the injection slit and micro-well by vacuum, filling them with mobile phase using a syringe, and finally translating the movable wall at a velocity of 2 mm.s^{-1} in order to propagate the injected plug in the channel. A CCD-generated image sequence is depicted in Fig. 5.
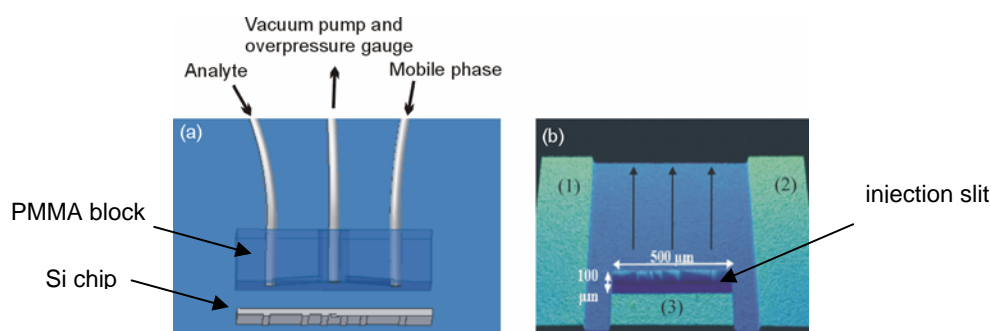
Fig. 4 Outline of the injection system. **(a)** The PMMA block is glued to the silicon chip and placed on a fused silica substrate (not shown) that serves as a movable wall. The supply channels in the PMMA connect to a cavity above the injection micro-well. The hole for the outlet capillary directly above the well was drilled somewhat larger than the capillary outer diameter to create an overpressure gauge, the other two capillaries are made to fit tightly and leak-free to the holes in the PMMA. **(b)** Wyko® (optical profilometry) scan of the backside of the etched well, showing the position of the injection slit in the channel, together with the non-etched channel spacer regions (1,2) delimiting the lateral extent of the channel and the non-etched region (3) preventing the mobile phase that is present in front of the channel to enter the channel. The flow direction is indicated by the arrows.

3.4.3 Chemicals

For the analyte solution 7-diethylamino-4-methylcoumarin (C460, Across Organics, Belgium) was dissolved in HPLC-grade methanol at a final concentration of 10^{-3} M, after which it was filtered. For the mobile phase HPLC-grade methanol was used.

3.4.4 Detection and plug analysis

To monitor the injections, the objective lens of an inverted microscope (Axiovert 200, Zeiss NV, Belgium) was positioned below the fused silica substrate. For large injected plugs (100, 200 and 300 μm translation distance) the peaks were monitored at 4 X

magnification, whereas for smaller plugs (100, 50 and 30 μm translation distance) the magnification was 20 X. To record the images, an air cooled CCD fluorescence camera (ORCA-ERG C4742-95-12, Hamamatsu Photonics, Belgium) was mounted on the video adapter of the microscope. For excitation of the analyte a Hg-vapour lamp (HBO103/W2, Zeiss, Belgium) was used, along with a UV filter cube set (U V-2A DM400 Nikon, Cetec N.V., Belgium). The camera was operated at a frame rate of 15 Hz and the exposure time was 10 ms. Analysis of the video images was performed with simple-PCI $^{®}$ 5.1 software. A region slightly smaller than the injection slit was vertically squeezed by the software to smoothen the concentration profile, this averages the intensity across the width of the channel. The peaks were fitted as Gaussian shapes using the program Sigmaplot 2000 (SPSS Science, IL, USA).
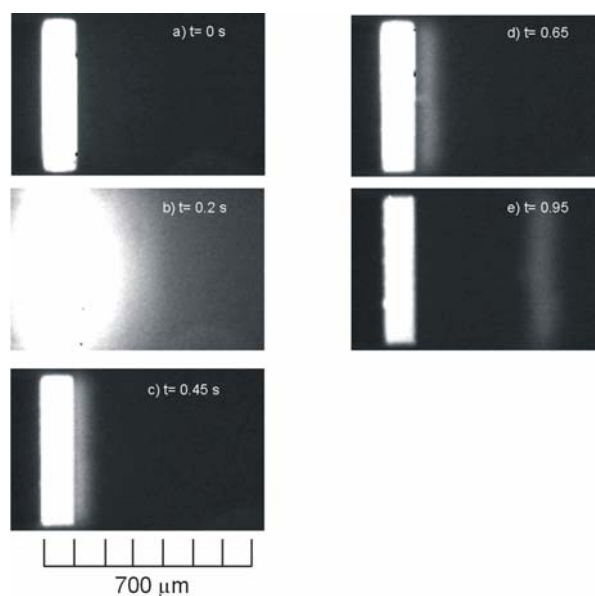
Fig. 5 Different steps in the injection procedure. **a)** the vacuum system is activated, **b)** the sample syringe is moved, **c)** the vacuum system stops while the movable wall is displaced (100 μm, 2 mm.s^{-1}), **d)** the vacuum is applied again and the well is filled with mobile phase, **e)** the tracer plug is transported through the channel by displacement of the movable wall (2 mm.s^{-1}).

For the quantitative evaluation of the peak width measurements, the diffusion coefficient of C460 in methanol was determined according to the method of Pappaert et al.[16] and found to be $8.0 \times 10^{-10} \pm 0.6 \times 10^{-10}$ m^{2}s^{-1}.

3.5 Results and discussion

Fig. 6 shows detailed view of the formation process of the injected peak and its evolution through the channel. In curve (1), the movable wall is stopped and the sample present in

the slit is replaced by mobile phase. Considering the curves (2) to (9) it can be seen that the left sides of the curves rapidly decrease in intensity. Curve (10) represents the final shape of the plug at the end of the injection process. The curves (11) to (16) correspond to the different positions of the peak during the actual flow process in the separation channel. As can be noted, the injected peaks become symmetrical within 100 micrometers of their displacement through the channel.
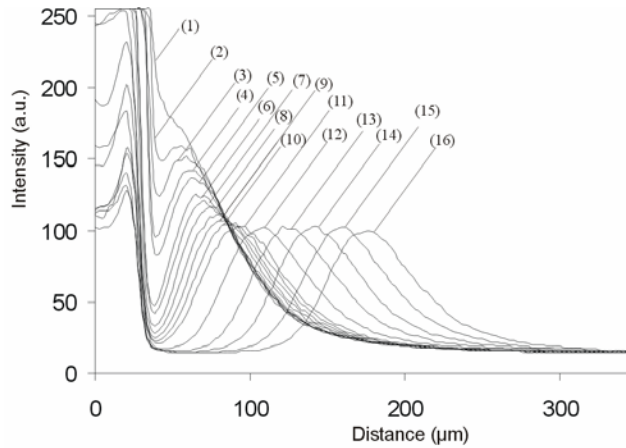
Fig. 6 Formation and evolution of a peak created by an injection with an injection translation distance of 100 μm (time step between consecutive intensity profiles is 23.2 ms). See text for details.

To characterize the operation of the injection method, different injection translation distances were investigated and the respective resulting peak widths were determined (table 1). Unfortunately, it was not possible to determine the peak width immediately after the plug is released from the slit because of the strong autofluorescence of the small PMMA piece closing off the injection well. For this reason, the plugs were analyzed at a given distance downstream of the slit. This distance had to be varied because the chips always slightly moved once the load pressure was applied. Depending on which position the width is measured, the difference in peak width can be calculated using

$$H = \Delta \sigma_x^2 / \Delta L = 2D_{mol}/u + (1/15) \, ud^2/D_{mol} \tag{2}$$

with H the plate height, σ_x the spatial standard deviation of the plug, L the distance the plug has traveled, u the movable wall velocity, d the depth of the channel and D_{mol} the diffusion coefficient. The origin of the factor "1/15" is discussed in [1]. Assuming a channel depth of 300 nm, Eq. (2) predicts a plate height value of 0.8 μm. This value is then used further on in Eq. (8) to compensate for the different measurement positions.

It was observed (see Fig. 7) that for injection translation distances below 100 μm the finally obtained plug width becomes independent of this distance.

For example, no difference is observable between an injection translation distance of 30 μm and 50 μm, both result in peak widths of 122 μm (± 3 and 4 % RSD, respectively). The timing for the pumping and suction events used to obtain the results depicted in Fig. 6 was the fastest possible with the current set-up. Using shorter filling and emptying sequences, the system went into a regime of irreproducible and tailed injections, due to the incomplete emptying of the well and limited time-response of the vacuum system.
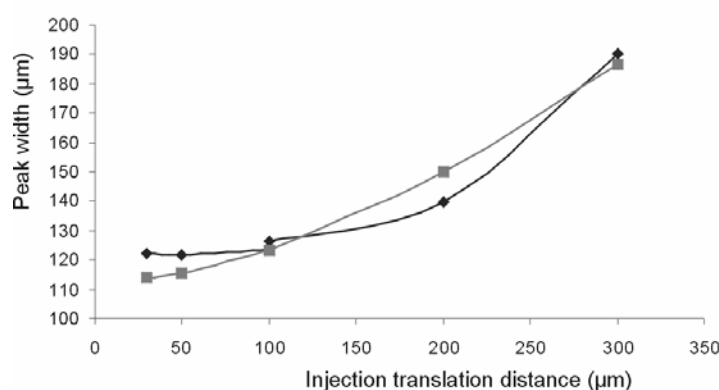
Fig. 7 Peak widths created by different injection translation distances. (—◆—) depicts the experimental values corrected for the peak width gained during movement in the channel after passing position 210 μm (the peak widths for injection translation distances smaller and equal to 100 μm have been obtained with a 20 X magnification, whereas the values for larger and equal to 100 μm translation distances where obtained with a 4 X magnification. (—■—) represents the theoretical values at position 210 μm. Estimated times for filling and flushing are 0.2 and 0.3 s, respectively.

To understand the relation between the injection sequence timing and the injection translation distance on the one hand, and the finally obtained injection plug width, the following consideration can be made.

A quantitative description for the diffusion out of a region of the injection slit and micro-well during the finite filling times is found as follows. As long as the reservoir is filled with sample, the peak width can be expressed as:[17]

$$w^2_{cont} = 5,382 \ D_{mol}t_{cont} \tag{3}$$

wherein t_{cont} is the total time during which the sample is in contact with the mobile phase occupying the rest of the channel:

$$t_{cont} = t_{fill} + z/u \tag{4}$$

In Eq. (3), the peak width w is expressed as being equal to 4 times σ_x, the square root of the second moment of the concentration vs. position profile.

The contribution due to movement of the movable wall during the injection is determined by the average distance (w_{conv}) over which the mobile phase has moved, which is half the injection translation distance of the movable wall (z):

$$w_{conv} = z/2 \tag{5}$$

The band broadening of the plug while remaining in place inside the channel during the flushing step can be derived from Einsteins's diffusion law (Eq. 1) and is given by: [18]

$$w_{flush} = (32 D_{mol} t_{flush})^{\frac{1}{2}} \tag{6}$$

The total peak width w_{inj} immedialy after the completion of the injection step is then found using:

$$w_{inj}{}^2 = w_{cont}{}^2 + w_{conv}{}^2 + w_{flush}{}^2 \tag{7}$$

The additional band broadening experienced during the movement of the plug over a distance x in the channel is then given by the product of the plate height H calculated with Eq. (2) and the average distance x over which the plug has moved, yielding for the final plug width:

$$\Delta w = 4 \left(w_{inj}{}^2/16 + Hx \right)^{\frac{1}{2}} \tag{8}$$

The above analysis has made it clear that the system variables t_{fill} and t_{flush} impose the minimal width of an injected plug. Roughly estimating these times as being respectively 0.2 s and 0.3 s, this gives rise to numerical values of respectively 29 μm and 87 μm and thus a total value of 92 μm. It is also important to notice that according to Eq. (2) smaller peaks give rise to a larger relative broadening. After having traveled 210 μm in the channel (this position is the reference value to compare experimentally determined peak widths), then an increase of 21 μm in width will occur. The total minimal peak width at our observation position is then 113 μm. Deviations of this model as are mostly due to the

approximation made in formula (6) and the uncertainty on the duration of the different steps.

In summary, the good agreement between the theoretical verification and the experimental results obtained implies that Eqs. (2-8) provide a good model to predict the injection peak width.

A crucial factor determining the success of an injection method for an analytical device is its reproducibility. Fig. 8b shows the fluorescence intensity profiles for three consecutive injections using the manual procedure described in Desmet *et al.*[17] As can be noted, the width of the injected plugs is relatively reproducible, but the intensity clearly is not.
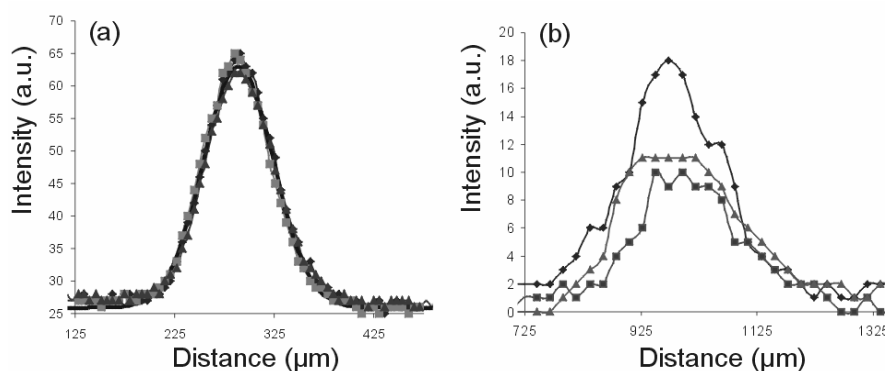
Fig. 8 (a) Repetition of 3 peaks generated by translating the movable substrate for a distance of 100 micron using the automated injection slit method. The thick line represents the average of the gauss fits of these experimental curves. The relative standard deviations of the peak width and peak area are both 1 %. **(b)** Repetition of 3 injected peaks using the semi-automated channel front injection procedure described in Desmet et al [3] . For the injection, the movable wall was translated over a distance of 100 μm. The plugs of 6.10^{-4} M FITC in methanol have traveled 975 μm after being injected. The variances of the peak width and peak area are respectively 12 and   27 %.

This is essentially due to slight variations in mobile phase drops remaining on the front of the channel substrate during the sample deposition. Depending on the magnitude of these drops, the deposited sample gets more diluted or less diluted, resulting in significant changes of the finally injected sample concentration. Another factor is the dependence on the dicing quality, which leads to non rectangular peaks in top-view. This is not the case in the automated system. Fig. 8a shows that the reproducibility of the injected sample plug width and concentration offered by the currently developed automated injection slit system is much better than with the semi-automated approach used in [17]. As indicated in Table 1, the RSD on the injection width was on the order of 1 %, except for the smallest peaks where diffusion plays a significant role and where the standard deviation was on the

order of 4 %. The RSD on the amount of injected sample was of the order of 3 % for all the injections, except for the 30 µm injection translation distance, where a value of 6 % RSD was found. Fitting the peaks in Fig. 8a with a Gaussian curve showed that the peaks

Table 1 Peak widths and relative standard deviations (n=3) of peak area and peak maximum observed at the respective positions for different injection translation distances.

Injection translation distance (µm)	Position (µm)	Peak width (µm)	RSD peak area	RSD peak max.
300	420	204 ± 1 %	3 %	1 %
200	475	162 ± 1 %	3 %	3 %
100	290	134 ± 1 %	1 %	4 %
100	230	126 ± 1 %	3 %	7 %
50	215	122 ± 4 %	2 %	1 %
30	210	122 ± 3 %	6 %	6 %

are nearly perfectly Gaussian. Although the run-to-run reproducibility of the injected concentration is quite good, the final sample concentration depends on the injected peak width. This is due to the dilution effects occurring during the flushing step of the injection (see curves nr. 2–9 in Fig. 6) caused by contact with the residual mobile phase in the supply channels and the micro-well that remain as a wetting layer. The peak concentration as measured for a 100 µm plug was 80 % (as compared to the fluorescence signal of a continuously introduced sample solution) of the sample concentration. For the smaller peaks the decrease was even stronger.

3.6 Conclusions

Using the presented chip layout and the combined vacuum and shear driven system, reproducible and undisturbed plugs have been injected with good reproducibility (relative standard deviations were max. 4 and 6 % for width and area, respectively, and were in some runs even equal to 1 %). This is an important asset for shear driven chromatography, as the analytical use of the system has always been hindered by the inability to perform reproducible injections. The semi-automated injections as performed in the past have always been shown to

be substrate dependent, since dicing quality differs considerably between different chips, and because of the human aspects of the injection. Apart from the variable timing of the consecutive injection steps used in different experiments, the unreliable positioning of the externally positioned mobile phase, sample needles, and of the vacuum system tube contributed to peak width and peak height variances. The most important variance came from uncontrolled dilution, as seen in the large difference in peak areas (RSD of 27 % for the old system as compared to a maximum of 6 % for the currently presented fully automated system). Another significant advantage of the new system (not realized in the present study however) is the ability to change the mobile phase concentration during a separation experiment in a controlled fashion and to perform gradient elution separations of complex mixtures.

Symbols

D_{mol} molecular diffusion coefficient (m^2/s)
H   height of a theoretical plate (m)
u   mobile phase velocity (m/s)
σ_x spatial peak standard deviation at position x (m)
w   peak width (m)

Abbreviations

RSD   relative standard deviation

References

1.   Desmet, G.; Baron, G. V. *Journal of Chromatography A* **1999**, *855*, 57-70.
2.   Desmet, G.; Baron, G. V. *Journal of Chromatography A* **2000**, 867, 23-43.
3.   Desmet, G.; Vervoort, N.; Clicq, D. Baron, G. V. *Journal of Chromatography A* **2001**, *924*, 111-122.
4.   Yang, X.; Jenkins, G.; Franzke, J.; Manz, A. *Lab on a Chip* **2005**, *5*, 764-771.
5.   Clicq, D.; Vankrunkelsven, S.; Ranson, W.; De Tandt, C.; Baron, G. V; Desmet, G. *Analytica Chimica Acta* **2004**, *507*, 79-86.
6.   Clicq, D.; Vervoort, N.; Vounckx, R.; Ottevaere, H.; Buijs, J.; Gooijer, C.; Ariese, F.; Baron, G. V.; Desmet, G.; *Journal of Chromatography A* **2002**, *979*, 33-42.
7.   Kutter, J. P.; Fintschenko, Y. *Separation Methods in Microanalytical Systems*, Taylor and Francis, Boca Raton, 2006.
8.   Jacobsen, S.C.; Hergenroder, R.; Koutney, L.B.; Warmack, R.J.; Ramsey, J.M. *Anal. Chem.* **1994**, *66*, 1107-1113.
9.   Jacobsen, S.C.; Hergenroder, R.; Koutney, L.B.; Warmack, R.J.; Ramsey, J.M. *Anal. Chem.* **1994**, *66*, 1114-1118.
10.   Thomas, C.D.; Jacobson, S.C.; Ramsey, J.M. *Anal. Chemistry* **2004**, *76*, 6053-6057.
11.   Jacobson, S.C.; Ramsey, J.M. *Electrophoresis* **1995**, *16*, 481-486.

12. Blom, M.T.; Chmela, E.; Gardeniers, J.G.E.; Tijssen, R.; Elwenspoek, M.; van den Berg, A. *Sensors and Actuators B: Chemical* **2002**, *82*, 111-116.
13. Blom, M.T.; Chmela, E.; Oosterbroek, R.E.; Tijssen R.; van den Berg, A. *Anal. Chem.* **2003**, *75*, 6761-6768.
14. O'Neill, A.P.; O'Brien, P.; Alderman, J.; Hoffman, D.; McEnery, M.; Murrihy, J.; Glennon, J.D. *J. of Chromatogr. A* **2001**, *924*, 259-263.
15. De Malsche, W.; Clicq, D.; Eghbali, H.; Vervoort, N.; Gardeniers, J.G.E.; van den Berg, A.; Desmet, G. *Proceedings of µTAS 2005*, Boston, MA, USA, pp.106-108 .
16. Pappaert, K.; Biesemans, J.; Clicq, D.; Vankrunkelsven, S.; Desmet, G. *Lab on a Chip* **2005**, *5*, 1104-1110.
17. Desmet, G.; Vervoort, N.; Clicq, D.; Huau, A.; Gzil, P.; Baron, G.V. *Journal of Chromatography A* **2002**, *948*, 19-34.
18. J. C. Giddings, *Unified Separation Science*; John Wiley & Sons, New York, 1991.

Chapter 4: Pressure-driven reversed-phased liquid chromatography separations in ordered non-porous pillar array columns

This chapter has been published as:

4.1 Abstract

Building upon the micro-machined column idea proposed by the group of Regnier in 1998, we report on the first high resolution reversed-phase separations in micro-machined pillar array columns under pressure-driven LC conditions.

Using arrays of non-porous silicon pillars with a diameter of approximately 4.3 μm and an external porosity of 55 %, a three component mixture could be separated in three seconds. Under slightly retained component conditions (retention factor k'=0.65 to 1.2), plate heights of about H=4 μm were obtained at a mobile phase velocity around u= 0.5 mm/s. In reduced terms, such plate heights are as low as h_{min}=1. Since also the flow resistance of the column is much smaller than in a packed column (mainly because of the higher external porosity of the pillar array), the separation impedance of the array was as small as E=150, i.e., of the same order as the best currently existing monolithic columns. At pH=3, yielding very low retention factors (k'=0.13 and 0.23), plate heights as low as H=2 μm were realized, yielding a separation of the three-component mixture with an efficiency of N=4000 to 5000 plates over a column length of 1cm. At higher retention factors, significantly larger plate heights were obtained. More experimental work is needed to investigate this more in depth.

The study is completed with a discussion of the performance limits of the pillar array column concept in the frame of the current state-of-the-art in micro-fabrication precision.

4.2 Introduction

As a radical solution to the tedious problem of column-to-column packing reproducibility of HPLC columns, Regnier[1] proposed in 1998 to leave the conventional approach to slurry pack HPLC columns with micron sized-spherical particles for the high-precision etching

technologies of the micro-electronics industry.[2] Given that these techniques also offer a perfect control over the position of each individual "particle", this novel manufacturing approach should also allow eliminating all possible sources of eddy-diffusion.

The advantage of the latter can be assessed from, amongst others, the work of John Knox.[3-4] Building further upon Giddings' coupling theory,[5] he postulated that the major fraction of the band broadening in a packed column is due to the mobile zone, and more particularly to the irregularity of the flow in the interstitial space (eddy-dispersion). He guessed that these flow irregularities are responsible for about one half of the widely accepted "theoretical" minimum of h_{min}=2 (h=reduced plate height=H/d_p). He derived this from the fact that in packed bed electro-chromatography (CEC), where the flow is much less sensitive to irregularities of the bed structure, minimal reduced plate heights of the order of h_{min}=1 can be obtained.[4,6-7] Reduced plate heights as low as h_{min}=1 have also been obtained under pressure-driven conditions in beds of very large particles (order of half a millimeter).[4] Such large particles can be made much more monodisperse than the micron size beads currently used in HPLC, and can hence also be assumed to pack more easily into a highly regular bed. Tallarek et al. showed experimentally using in-situ pulsed field gradient NMR that the part of the minimal plate height value in excess of h_{min}=1 is due to large scale inhomogeneities variations in packing density (long range and transcolumn coupling).[8] The advantage of ordered packings to obtain lower degrees of axial dispersion was also already recognized a long time ago in the field of chemical engineering.[9]

Making a computational fluid dynamics study of chromatographic beds with various degrees of packing heterogeneity,[10-11] it was found that the minimal reduced plate height in a perfectly ordered packing of porous pillars grouped in an array with an external porosity of ε=40% can be expected to be equal to h_{min}=0.91 (retained component with retention factor k'=1.25), i.e., very close to Knox' prediction. Fitting the numerically calculated Van Deemter-curve with a variety of different plate height equations revealed that the decrease in plate height obtained by going from the most heterogeneous packing case to a perfectly ordered packing case was essentially due to a strong decrease of the A-term contribution, also in perfect agreement with the physical meaning of the A-term.[3,12]

The above shows that if the currently used chromatographic beds could be made with a perfect packing uniformity, they would yield twice the amount of theoretical plates without having to change anything about the packing density or the particle shape. Moreover, since

the minimal time needed to achieve a given separation resolution scales according to the square of the plate height,[13-15] a perfectly ordered equivalent of a packed column would allow for a fourfold reduction of the time needed to achieve a given resolution. Combining the advantage of the increased order with the possibilities to produce channels with a larger external porosities and/or improved pillar shape possibility, even much larger gain factors can be expected.[10]

In their exploration of the possibilities of this microfabricated column concept, Regniers' group however mainly focused on electro-driven separations (CEC).[2,16-17] Partly because CEC seemed a very powerful alternative for HPLC at that time, but also because the electro-driven flow is less sensitive to slight local differences in pillar size than a pressure-driven flow. The microfabrication technology they had at their disposition at that time was not really perfect and yielded pillars that were not as uniformly positioned and sized as needed. Using an inlet system of subsequently bifurcating distribution channels (cf. Fig. 6 of He et al. [2]), the channels they used were also sensitive to slight differences in flow resistance between the different branches. These small differences were inevitable with the etching technology that was available at that time.

With the advent of new, more accurate etching technologies such as the Bosch[®]-process, it is now possible to etch micro-pillar arrays with a much higher spatial resolution.[18-20] Another advantage of the Bosch[®]-process is that it allows producing pillar arrays that are deeper than previously possible without obtaining pillars that are narrower at the bottom than at the top. This situation is absolutely to be avoided because it would create a velocity gradient between the bottom and top wall of the pillar array that would otherwise be detrimental for the separation resolution.

Given these new machining possibilities, and the large potential advantage, it is not unexpected to see that more and more groups are now revisiting the microfabricated column idea. Recent results have been presented by Mogensen et al., Ricoul et al. and De Pra et al.[20-22] In the latter study, pillar diameter-based reduced plate heights as small h=0.2 could be obtained for $d_p = 10$ μm pillars.

In the present study, the same type of silicon micropillar array channels as used in De Pra et al.[22] has been used. Whereas the study in ref. (22) only investigated the flow and flow

resistance characteristics of a pillar array column, the present study focuses on the conduction of reversed-phase LC separations. Conducting RP-LC separations in an array of nonporous silicon pillars is in principle relatively straightforward. The native silicon dioxide layer that spontaneously forms on any silicon surface that is exposed to the air can be expected to yield a large number of silanol groups, allowing the use of conventional silanization reagentia for the application of a reversed-phase coating monolayer. In the present study, the spontaneous air oxidation has been enhanced by wet oxidizing the pillars after they were fabricated.

To prevent problems with the potential flow maldistribution in the bifurcating inlet used in He et al.[2] and Mogensen et al.,[20] it has been opted to decouple the sample and mobile phase introduction. This necessitated the fabrication of an on-column injection system. On-column injection methods for pressure-driven injections in microfluidic devices have in the past few years been presented by a number of groups and could therefore be used as an inspiration.[23-27] To obtain a maximal visual control over the ongoing flow and separation effects, and also because the use of an off-column detector would cause to many external band broadening, it was opted to monitor the separations on-column with a state-of-the-art CCD camera. Although simulation studies revealed that diamond shaped pillars are better than cylindrical pillars [10], the present study focused on cylindrical pillars, without any other particular reason than to have the closest possible agreement with the packed bed of spheres. Comparing with the latter then provides the most direct way to quantify the effect of the bed homogeneity on the performance of chromatographic columns.

4.3 Experimental

4.3.1 Channel Fabrication

The pillar channels were defined in a silicon-glass sandwich. First, a 100 mm diameter (100) silicon wafer (p-type, 5-10 Ω cm resistivity) was thermally (dry) oxidized at 1100 °C until 200 nm silicon oxide was formed (Amtech tempress omega junior). Then, normal UV photolithography (photoresist: Olin 907-12) was used to define the pillar array. Subsequently, the exposed silicon oxide was dry etched (Adixen AMS100DE), after which the resist was removed by oxygen plasma and nitric acid. Another lithography step was then used to define the inlet and outlet channels. The exposed silicon oxide was then etched and a Bosch-type deep reactive ion etch (Adixen AMS100SE) was used to make these channels 60 μm deep.

After stripping the resist, another 11.5 μm was Bosch-etched into the exposed silicon, leaving pillars of 11.5 μm height and supply channels with a total depth of 71.5 μm. To remove the fluorocarbons, the wafers were set in a (wet) oxide furnace (Amtech tempress omega junior) at 800 °C for 30 min, after which the wafers were cleaned in nitric acid and dipped in HF. Subsequently, the wafers were wet oxidized again for 30 min in order to provide a maximum amount of silanol groups for the coating step (see below). The top of the channels was formed by a 100 mm diameter Pyrex® wafer (thickness 0.5 mm). On the silicon wafer, through-holes were first defined by photolithography on a dry resist foil (Ordyl BF410). The exposed glass was subsequently powder blasted using 30 μm alumina particles. After stripping the foil, the substrates were anodically bonded (voltage ramped to a maximum of 1000 V at 400 ℃, on an EVG EV-501 wafer bonder).

4.3.2 Chip coating procedure

To enable reversed phase LC separations, the mantle surface of the microfabricated pillars was covalenty coated with a monolayer of hydrophobic C8-chains. Both the coating and flushing step were carried out using a commercial nano-flow HPLC-system (Agilent Technologies 1100 series, Darmstadt, Germany). The connection between the pump and the chip was established by means of a home-made set-up. In this set-up, the chip was sandwiched between a holder that consisted of 2 plates. The top plate was made of Delrin and was perforated with drilled through-holes that were compatible with commercially available Upchurch® nanoport connectors (Achrom, Belgium). The bottom plate was made of aluminium with the central part removed to observe the microfluidic channels on the chip with the inverted microscope during the experiments. The tubing used to connect the pump and the chip consisted of fused silica capillaries (Achrom, Belgium) with an ID of 150 μm.

A PEEK-tubing (ID=1 mm) with a length of 1,5 m was manually filled with a 15% (v/v) solution of octyldimethylchlorosilane (Sigma-Aldrich, Belgium) in HPLC-grade toluene (Sigma-Aldrich, Belgium) (Fluka, Belgium) using a commercial syringe and subsequently inserted between the pump and chip by applying two capillary-PEEK-tubing adaptors (Achrom, Belgium) at both ends of the tubing. This solution was then pumped through the chip for 5 hours at a flow rate of 0.3 μl/min. Finally, the chip was flushed for 5 h with toluene and 3 h with methanol at a flow rate of 0.5 μl/min. Solutions used in the experiments were filtered through Anotop 25 filters (Whatman, England).

4.3.3 System hardware and separation procedures

The basic principle of the employed injection procedure has been described previously [23-24] and is based on the presence of an injection zone devoid of pillars (200 µm wide in the present case). The sample injection consisted of two consecutive steps: the definition of a sample plug with a certain defined axial width, followed by the transportation of this plug along the column by the mobile phase flow. Two external six-port valves (Rheodyne MX, Germany) close the mobile phase inlet and outlet during injection and the sample inlet and outlet during separation.

A home-made set-up with pressurized vessels, controlled by two pressure controllers, was used to provide the required pressure for the flow generation in the two steps of the injection process. The sample reservoir as well as the mobile phase reservoir consisted of two different home-made stainless steel vessels coupled to 0.2 µm pore size filters. The vessels were independently connected to two different pressure controllers (Bronkhorst, The Netherlands), fed by a nitrogen gas bottle, that allowed to control the pressure in the vessels with a precision of the magnitude of millibars. This approach allowed applying two different independent pressure settings, one for the sample injection and one for the mobile phase flow. Wide capillaries (ID=150 µm, Achrom, Belgium) were used for the connection between the pressurized vessels and the chip, so that the pressure readout of the pressure controllers could be used as a measure of the inlet pressure of the column. The operation of the pressure controllers, the external valves, as well as the translation stage was automated using a home made software program written in C++ allowing the simultaneous control of all these instruments from one central computer.

Maximal pressure was currently set at 22.5 bar, due to the pressure limitation of the employed mass flow controllers. Linear velocities ranged from 0.03 to 3.8 mm/s at respectively 0.2 and 22.5 bar. In terms of flow rate, this corresponded to 0.2 µl/min at 20 bar. Using a nano-flow HPLC pump, the currently used set-up was also tested at more elevated pressures. It was found that, at least up to 60 bar, the set-up could be operated without creating any leakage. Higher pressures were not tested yet.

The separation experiments were performed using as a mobile phase a methanol-water mixture with ratios varying from (20/80, v/v) to (30/70, v/v). In most experiments, the water phase was buffered at pH=7 using a phosphate buffer. A number of experiments was also undertaken using a buffer at pH=3, mentioned where applicable. For the evaluation of the

separation properties, a mixture of 3 coumarin dyes [28-29] has been used. Coumarin dyes are known to have a high quantum yield, and can therefore still be easily detected in highly miniaturized systems.[30] For the separation experiments, solutions of coumarin C440 ($0,75.10^{-4}$ M), C460 ($0,75.10^{-4}$ M) and C480 (3.10^{-4} M) (Fluka, Belgium) were prepared in the same methanol/water ratio as the mobile phase in order to avoid viscous fingering.[31] For the detection of the fluorescent sample plugs, an inverted microscope (Axiovert 200, Zeiss NV, Belgium) was used, equipped with a UV-1 filter cube set (U V-2A DM400 Nikon, Cetec N.V., Belgium) allowing for excitation at 350 nm and for emission above 450 nm. In this way, the standard Hg-vapor lamp (HBO103/W2, Zeiss, Belgium) of the microscope could be used to excite the fluorescent coumarin dyes in the UV. The maximal emission of the fluorescent light occured around 460 nm. The separations were visualized using an air-cooled CCD fluorescence camera (ORCA-ERC4742, Hamamatsu Photonics, Belgium) mounted on the video adapter of the microscope. The video images were subsequently analyzed with the accompanying simple-PCI® 5.1 software. The microscope was mounted on a breadboard (M-IG 23-2, Newport, The Netherlands), together with a linear displacement stage (M-TS100DC.5, Newport) and a speed controller (MM, 4006 Newport).

It was verified that the signal remained linear in the range of pixel intensities between 15 (background noise level) and 240. With a typically employed set of camera settings this corresponded to concentrations ranging between 60 μM and 1 mM. Care was taken that all experiments were conducted in this range.

As the marker for the mobile phase velocity, the coumarin C440 was used. It was checked that its elution velocity was, within the uncertainty of the measurement, always very close to the unretained component velocity expected on the basis of the established pressure-flow rate correlation and the viscosity value corresponding to each of the different employed mobile phases. Viscosity values were taken from.[32]

4.3.4 Safety

Hydrofluoric acid and nitric acid have been used during the chip production in the clean-room. Inhalation and contact with skin and eyes has to be avoided. The pressurized vessels and its tubing to the nitrogen bottle should be fixed conform the rules for working with pressurized gases. During depressurization, solvent vapor is released from the vessels through

a separate tubing, this should occur in a well ventilated environment. Given their presumed toxicity, the coumarin dyes must be handled with care.

4.4 Results and discussion

Fig. 1a shows a bird's eye view of part of the entrance region of one of the employed micro-pillar array columns. The injection zone, devoid of pillars and having the same 11.5 μm depth as the pillar array region, is enclosed by two laterally running injection channels. Both are 71.5 μm deep and are used during the sample injection step: one for the feeding of the sample and one for the evacuation of the excess of introduced sample (see also the white arrow flow pattern added to Fig. 1a).

Fig. 1b shows a detail of the same column. The picture shows the individual pillars, as well as the equilateral triangular positioning grid used to define the position of the pillar centers. It also shows how the last row of pillars immediately adjacent to the side-wall is positioned with respect to this wall. The design of the side-wall region was based on a previous numerical design study.[33]
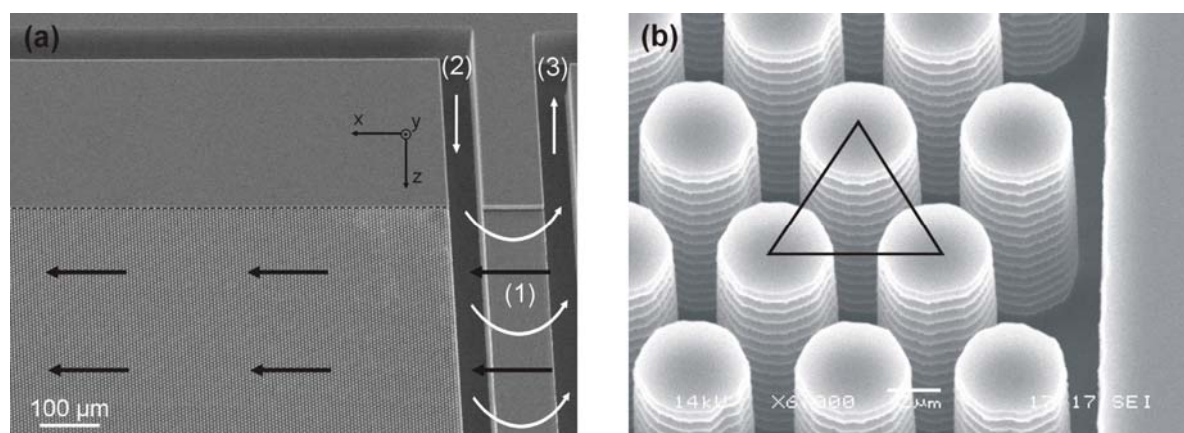
Fig. 1 SEM (Scanning Electron Microscopy)-images of a microfabricated pillar array column produced on a silicon wafer: **(a)** bird's eye view showing the injection zone (1), the sample feeding (2) and evacuation (3) channel, and a part of the micro-pillar array near the one of the two side-walls. During the sample introduction step, the sample flows as indicated by the white arrows. During the separation, the mobile phase enters from the mobile phase inlet channel situated at the front end of the channel (situated to the right of position (3) but not shown here), following the pattern indicated by the black arrows. **(b)** A zoom-in of the pillars near the side-wall region. The black equilateral triangle represents the unit cell of the ground-plan that was used to position the center of the individual pillars.

The white rings that can be observed on the mantle surface of the pillars are due to the indentations or scallops that are formed on the pillars because of the cyclic nature of the Bosch® etching process. In this process, each cycle consists of a first step (typically lasting 1

to 2 s) wherein fluorocarbons (inhibiting the etching) are deposited on the bottom and side walls of the structure that is being recessed.

In the subsequent etching step (typically lasting 3 to 7 s), these fluorocarbons are much faster removed at the bottom of the channel, while the side-walls of the pillars remain much longer covered and are hence much less attacked by the etching plasma, allowing them to retain a nearly perfectly vertical slope. The presence of the indentations can be inferred to have no significant effect on the band broadening, because they disturb the flow over a much shorter distance than the pillars themselves.[34-35] The masks were designed to yield a pillar array with an external porosity (ε) of exactly 40%, and with a distance between the last row of pillars and the flat side-wall that exactly matches the "magical" distance calculated in Vervoort et al.[33] needed to eliminate the additional band broadening that could originate from the side-wall zone (cf. discussion further below). Unfortunately, the precision with which the lithography mask can be transferred into the silicon wafer depends on various poorly controllable effects such as the diffraction of UV-light in micron-sized dimensions and the inevitable under-etching of the used silicon oxide mask. With the current state of the art in etching technology, it is therefore nearly impossible to prevent deviations between the mask dimensions and the dimensions of the finally obtained microstructure of the order of a few tenths of a micrometer.[36] Measuring the finally obtained pillar diameters from a large collection of SEM pictures, the average diameter in all channels used in the present study was found to be equal to d_p=4.3 μm. This constitutes a deviation of about 0.7 μm from the target value of d_p=5 μm. Fortunately, this deviation is highly uniform throughout the entire array, such that the pillar-to-pillar diameter variation is much smaller (less than 0.1 μm). An exception to this is again the region near the side-walls, where the extra-pillar volume is locally higher, hence leading to different light diffraction effects and therefore also to slightly different pillar diameters.

Since the numbers of pillars is not affected by the underetching, the deviation from the target pillar diameter of course also causes the external porosity ε to deviate from its target value. The external porosity ε, defined as the ratio of the extra-pillar volume and the total channel volume, is a highly important geometrical parameter. Together with the pillar diameter, it determines the inter-pillar distance, which in turn can be inferred to be the main controlling factor of the band broadening and flow resistance of the column. In the presently studied channels, the external porosity was determined to be ε =55%, whereas the original mask design aimed at an external porosity of ε =40%.

Another consequence of the imperfect replication of the mask pattern into the wafer is that the pillar-to-wall distance in the side-wall region (cf. Fig. 1b) deviates from the "magical" distance calculated in Vervoort et al.[33] The physical reason for the existence of this "magical" distance is that it is the distance for which the flow resistance of the flow-through pore near the side-wall is identical to that of the flow-through pores in the rest of the array. As a consequence, it prevents the formation of a velocity difference between the side-wall through-pore and the rest of the array. If this condition is fulfilled, the pillar array column can be expected to produce the same amount of band broadening as if it had no sidewalls (at least for the case of unretained components). It is well known that, despite the wall region only makes up a small fraction of the total column volume, the existence of a velocity difference between the wall region and the rest of the array can give rise to a strong additional band broadening.[37-41] In Vervoort et al.,[33] it was shown using numerical simulations that a deviation of about 15 % of this magical distance can already lead to a fourfold increase of the plate height (non-retained species in non-porous pillar array). Experimental evidence of the dramatic influence the side-wall effect can have on the observed band broadening has recently been given in De Pra et al.[22]

Measuring the deviation between the actual pillar-to-side-wall distance and the preset target value on three different channels on the same wafer, deviations in both the positive and the negative sense were observed. In one channel, there was even one side with a positive deviation and one side with a negative deviation. The typical magnitude of the deviation was 0.2 μm, while the ideal pillar-to-wall distance for an array of 5 μm pillars with an equilateral triangular arrangement and $\varepsilon=0.4$ can be calculated to be equal to 0.76 μm. The measured deviations are hence even larger than the 15% deviation that is known from Vervoort et al. [33] to lead to a fourfold increase of the total band broadening.

Fig. 1b also shows that the pillars slightly deviate from a perfectly circular shape and show some slight deformations. This is most probably due to the wet oxidation process employed after the etching step to create a maximal number of silanol groups on the pillar surface. This was inferred from the fact that the pillars in the arrays that were produced without this additional step were perfectly circular. Fig. 2 shows a compilation of CCD camera images of an eluting band (slightly retained, with k'=0.65) taken at different positions along the axis of the column. The first three images were acquired in the first 1.7 mm of the channel, the last image was obtained after displacing the channel over a distance of about 1 cm downstream of

the injection point. With an exception for the two side-wall regions, Fig. 2 shows that the central line (extending in the z-direction) of the eluting band remains perfectly straight (see also Fig. 3a further on). Some small local disturbances of the eluting bands can still be noted, but these disturbances can be attributed to the presence of some crystallized dye that typically appears after some injections at the injection zone (cf. the intense spots remaining in the injection zone after the injection of the band), as well as to the occasional presence of dust particles in the channel. The former problem can be limited by regularly flushing the channels with a good solvent (e.g. methanol), whereas the latter is tougher to solve and requires further research. This should come as no surprise because fouling of microchannels is generally recognized as an important and often underestimated issue.[42] Whereas the band deformation in the central part of the channel can be well prevented, the deformation of the bands in the side-walls regions was an intrinsic problem in all considered channels. As mentioned here above, this deformation results from a non-ideal pillar-to-wall distance, in turn caused by the inaccurate replication of the feature sizes on the mask into the silicon wafer and from the existence of a lower limit on the distance that is needed to resolve two adjacent features during the lithography step.

The channel used to perform the measurements shown in Fig. 2 apparently has side-wall regions where the flow resistance is smaller than in the rest of the array, hence giving rise to two fronting thin band parts, one near each side-wall. As can be noted by comparing Figs. 2a-d, the thickness of the zone where the sample runs in front of the central region of the band increases with the distance elapsed in the column. This is a consequence of the radial dispersion of the sample species. Initially, only the sample species that were injected immediately adjacent to the side-walls are subjected to the higher velocity prevailing in this region. As the time elapses, more and more sample species have had the chance to diffuse back and forth between the central uniform velocity region and the two side-wall regions, and will hence have experienced the strong additional band broadening caused by the large velocity difference between the central zone and the side-wall zone.

Given that the number of species that has been subjected to this side-wall induced band broadening initially grows with the time, it can be inferred that the ensemble averaged plate heights that are measured during this transient phase will also increase with the time. This type of transient band broadening is more pronounced but very similar in nature to the side-wall effect in an open-tubular channels. The latter problem has been very clearly described by Dutta and Leighton[45] using numerical simulations. Their simulations show how plate height measurements performed during this transient phase and taking into account the entire

channel width can be expected to yield values that continuously grow with the x-coordinate of the detector plane. The observed plate heights only reach an asymptotic value if all sample species have been exchanged a sufficient number of times between the central region and the side-wall regions. The onset of this asymptotic regime is noted by the disappearance of all radial concentration gradients.
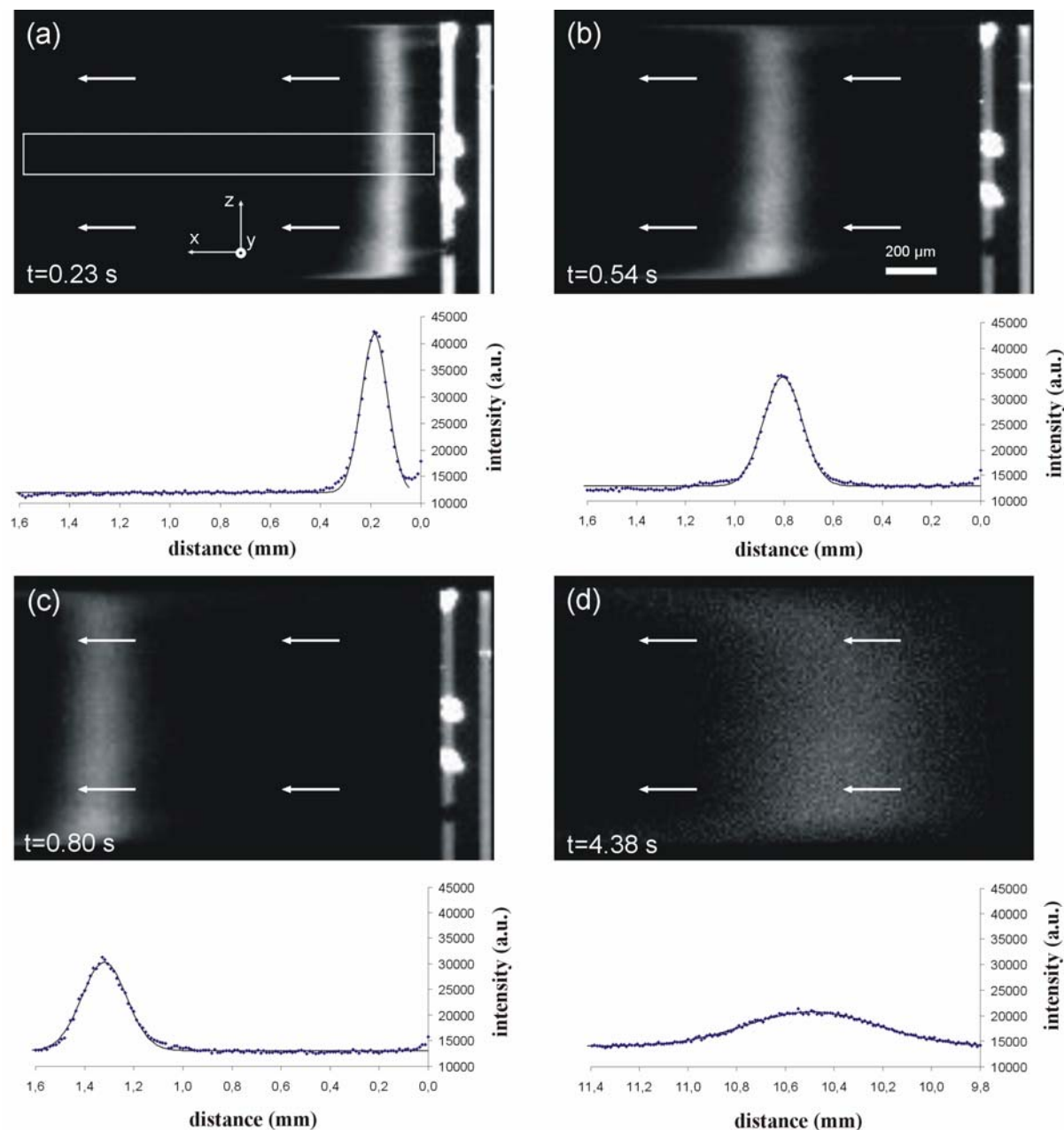
Fig. 2 Injection and movement of a retained plug of C460 (0.3 mM) in (30/70, v/v) water-methanol with a mobile phase velocity of 3.3 mm/s and the plate height of 8.5 μm. Pictures **(a)** through **(c)** depict the CCD images respectively taken at 0.23 s, 0.54 s and 0.80 s after the injection. In **(d)**, the image is taken 1 cm downstream the injection zone at 4.38 s after injection. Underneath each picture a pixel intensity read-out of the arrested image is shown (diamonds). The obtained profiles have been fitted with the Gaussian distribution function given in Eq. (1).

As can be noted from the banana-shaped band in Fig. 2d, taken 1 cm downstream from the injection point, this asymptotic regime is certainly not reached within the first centimeter of the array. Fig. 2a also allows discussing the quality of the currently employed injection process. Ideally, the injected bands should have a uniform axial width, independently of the z-coordinate. In a first approximation this is indeed the case. The shape of the injected bands anyhow approaches much better the pursued ideal rectangular shape than in the case of electrokinetic injections,[46-48] where usually a more trapezoidal shape is obtained. Making the comparison with electrically-driven injections, the rectangular shape of the injected bands should even be more appreciated if taking into account that the channels employed in the present study have a width of 1 mm, while the channels typically employed in CE and CEC-chip applications are seldom larger than 100 μm.

A more close inspection of the injected bands however reveals that they become gradually broader towards the side of the array where the sample enters first. Considering the injection flow pattern added to Fig. 1a, this is not unexpected, because there is a certain delay between the moment at which the sample crosses the injection zone near the side-wall where the sample enters first and the moment at which the sample does the same at the other end of the array. With the presently employed injection pressures of about 2 bar, this delay is of the order of 300 ms. During this time, a significant amount of diffusional band broadening can already occur near the channel wall closest to the sample inlet channel.

Below each picture of Fig. 2 the intensity read-out obtained by averaging the pixel intensity over each vertical row of pixels is given as well. Recording the passage of a species band in the same column segment (having a width of 1.6 mm with the employed 4 times magnification), and measuring the surface area under each pixel intensity curve, the typical variation of the area was less than 2 % (cf. Figs. 2a-c for example). This very low area variation demonstrates the excellent quality (linearity and sensitivity) of the employed on-column detection method. When the peak was picked up one centimeter further downstream, the surface area of the eluting bands typically varied about 5 to 10 %. These variations were quite random (i.e. occurred both in the positive and the negative direction) and were therefore assumed to be due to small changes in the distance between the channel and the microscope lens. Such changes are inevitable if displacing the wafer over distances of more than a few millimeter. Employing a different detection scheme, such as on-chip UV absorption with embedded optical waveguides or on-chip electrochemical detection,[49-52] would resolve this problem.

Trying to measure further downstream, i.e. at distances of 2 or more centimeter, a systematic decrease of the peak area was observed, presumably because the intensity in the peak front and tail becomes so small at longer distances that it tends to disappear in the background noise. Undoubtedly, this process is accelerated by the ongoing strong side-wall induced band broadening that gradually affects ever larger parts of the migrating bands (compare e.g., the band shape in Fig. 2a with that in Fig. 2d).

The plotted light intensity profiles in Fig. 2 only relates to the pixels falling into the white rectangular box (width in z-direction=150 µm) drawn in Fig. 2a. In this way, only the band broadening information coming from the central channel region is considered while the contributions coming from the side-wall regions are excluded. This approach was preferred because, as explained above, plate height values that include the side-wall effect are difficult to generalize. They inevitably vary strongly with the distance over a very long entrance length. This entrance length in turn can be expected to depend strongly on the width of the employed channels. Furthermore, designs can be conceived where the side-wall effect can be totally excluded. This would be achieved if using sufficiently wide channels where the central part of the channel is so far removed from the side-walls that the sample species migrating in this zone still have not had the time to diffuse towards the side-wall region at the time they elute from the channel in combination with injection and/or detection windows that are only interfaced with this unaffected central channel part.

In the white box, two types of measurements were made: i) time-response intensity plots obtained by monitoring the average pixel intensity on a preselected vertical row of pixels as a function of the time, and ii) spatial intensity plots, measured by considering a given video frame and plotting the z-direction averaged pixel intensity on each vertical row of pixels as a function of the distance. The latter type of intensity plots shows the spatial sample species distribution at a given moment in time. The pixel intensity plots shown in Fig. 2 have for example been obtained in this way.

The time response curves have been used to record separation chromatograms (Fig. 3), the spatial distribution curves have been used to make accurate plate height measurements for the van Deemter curve study shown in Fig. 4. It was experienced that the variance measurements in the time domain were less accurate than the spatial domain measurements, due to a smaller number of points per peak. For the time-domain measurements at 1 cm, the trade-off between

signal intensity and sample rate that needed to be made compromised an accurate determination of the band broadening in the high velocity experiments.

The peak spatial peak profiles shown in Fig. 2 have been fitted with a Gaussian function:

$$C_x = C_{max} \exp[-0.5 ((x-x_0)/\sigma_x)^2], \tag{1}$$

wherein x_0 is the position of the peak maximum and σ_x the spatial standard deviation. Comparing the fitted curves with the experimental data points, Fig. 2 shows that, after some initial small deviations, the bands assume a perfectly Gaussian peak shape 1 cm downstream of the injection zone.

Fig. 3a shows two video frames of the elution of the species bands respectively 1.57 and 4.87 seconds after injection of a three component coumarin dye mixture. It clearly shows that, despite the use of non-porous pillars with a fairly large inter-pillar spacing, the retention strength of the pillar array column is still sufficiently strong to separate the three component mixture in the first millimeter of the channel. For the employed 85/15 (v/v) water/methanol mobile phase, the measured retention factors were k'≅0, k'=2.0 and k'=4.3 for coumarin C440, C460 and C480 respectively. This shows that, provided sufficiently aqueous mobile phases are used, the non-porous pillar array column offers a sufficient retention capacity to separate the 3 component coumarin dye mixture in a distance of less than 1 millimeter. Fig. 3b shows the time response chromatogram of the same separation recorded by reading out the average pixel intensity on a selected row of pixels (extending in the z-direction and positioned at x=1.2 mm downstream of the injection zone) as a function of the time. As can be noted, the three coumarin dyes are clearly base-line separated. Calculating the plate heights by measuring the peak width at 13 % of the maximum value, the measured values were respectively H=1.5, 11.2 and 18.9 μm. Whereas the first value is certainly very low, on a pillar diameter reduced basis only slightly larger than the unretained data presented in De Pra et al.,[22] the plate heights for the two more strongly retained coumarins appear relatively large. Given the lack of theory against which these measurements can be evaluated, it is however very difficult to turn this into a clear statement. It needs for example to be verified whether, given the many different chemical treatments the pillar arrays have gone through, the coating that has been used is not unevenly distributed on a microscopically small scale. I.e., it might very well be that the coating density varies from pillar to pillar or from pillar region to pillar

region. This could be a potential source of additional band broadening and requires further investigation. Whereas the separation shown in Fig. 3a-b is performed at a relatively low velocity (u=0.6 mm/s), it was also possible to speed up the separation by increasing the mobile phase velocity. Fig. 3c, recorded at a pixel row positioned at x=1.7 mm, shows a
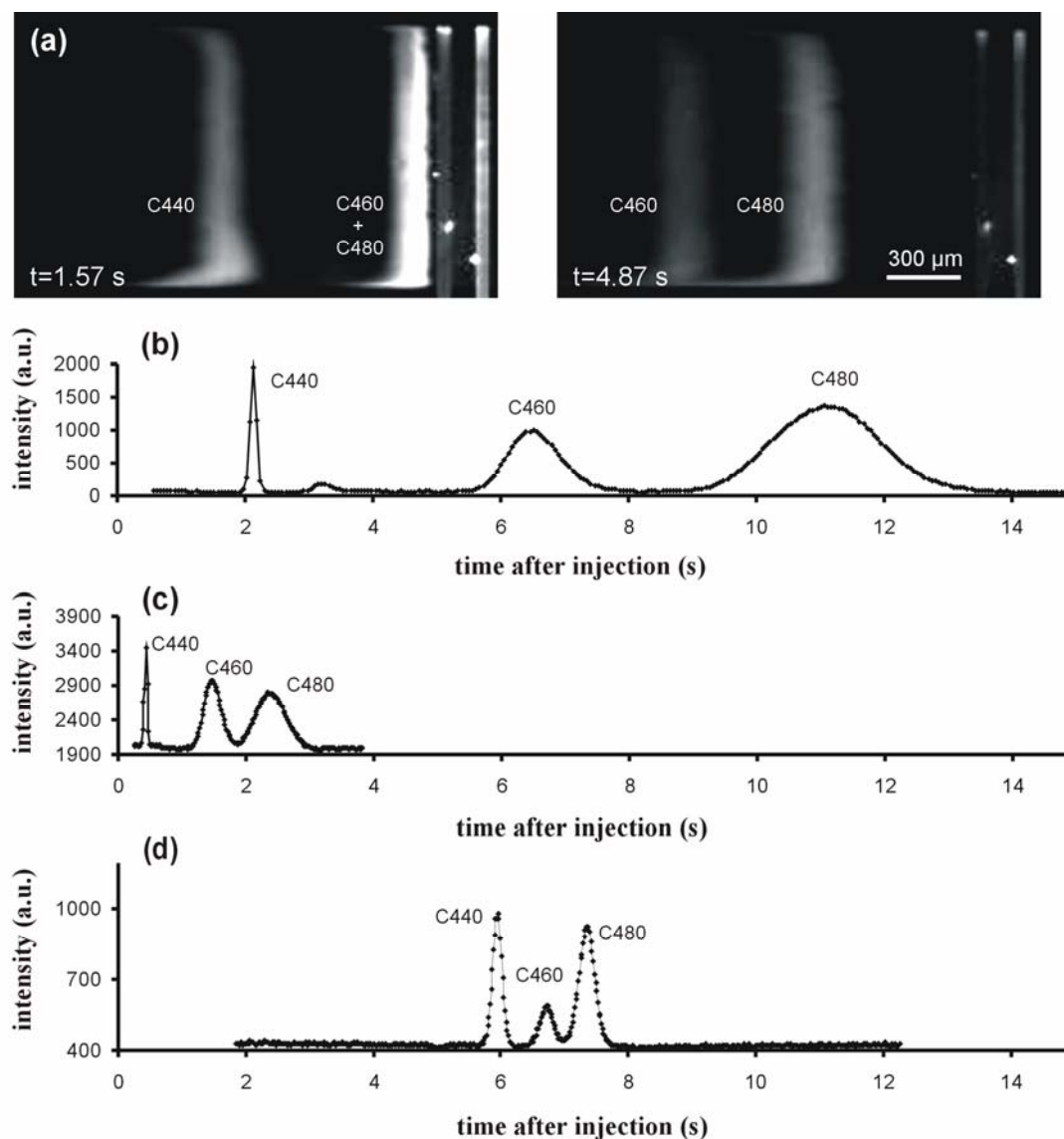
Fig. 3 Separations of C440, C460 and C480. **(a)** depicts the CCD image at 1.57 s and 4.87 s in a (20/80, v/v) methanol-water yielding retention coefficients of respectively k'≅0, k'=2.0, and 4.3 k'= (mobile phase velocity is 0.6 mm/s); concentrations are 0.25 , 0.25 and 1 mM, respectively. **(b)** chromatogram of **(a)** obtained at 1.2 mm downstream the injection zone. Plate heights are respectively H=1.6, 9.7 and 18.7 μm. The small peak at around 3.2 s is an unidentified impurity of one of the dyes, similar to what has been observed in Moore et al.[53] **(c)** Separation using same conditions as in **(b)** but employing a different mobile phase velocity (3.5 mm/s). Plate heights as monitored at position x= 1.7 mm are respectively H=3.5, 13.1 and 17.1 μm; concentrations are 0.25, 0.40 and 1 mM, respectively. **(d)** Chromatogram at x= 1 cm with (30/70, v/v) methanol-water, plate heights are respectively H=1.3, 2.0 and 2.4 μm with retention coefficients of respectively k'≅0, k'= 0.13 and k'=0.23; pH=3 and concentrations are 0.35, 0.20 and 0.75 mM, respectively.

nearly perfect baseline separation in 3 seconds. For this separation, the measured retention factors were k'≅0, k'=2.4 and 4.4 for respectively coumarin C440, C460 and C480, while the plate heights as determined at 13 % of the maximum concentration were respectively H=1.6 μm, 14.5 μm and 15.4 μm. The latter two values again appear relatively high, but nevertheless allowed for a clear three component separation in three seconds. The detection sensitivity of the employed CCD camera detection scheme was large enough to also detect separations at x=1cm, provided the bands were not too strongly retained. Fig. 3d shows such a separation, using a 70/30 (v/v) water/methanol mobile phase at pH=3. In this case, the measured retention factors were k'≅0, 0.13, and 0.23 for C440, C460 and C480, respectively. The following plate heights were obtained: 1.4 μm, 2.0 μm and 2.4 μm for the respective coumarins. These values are very low, and correspond to an efficiency of N=4,000 to 5,000 plates in 1 cm.

To make a more systematic study of the band broadening characteristics of the system, plate height measurements have been made over a broad range of fluid velocities, using the type of spatial distribution profile measurements shown in Fig. 2. Given that the front and tail parts of the more strongly retained bands were difficult to detect at a distance of one centimeter downstream of the injection, only low retention factor conditions were considered (mobile phase with 70/30 (v/v) water/methanol and pH=7). For these conditions, the retention factors were respectively found to be equal to k'≅0, k'=0.65 and k'=1.19 for coumarin C440, C460 and C480 respectively.

Given that we needed to measure over a relatively short distance, the width of the recorded bands was still significantly influenced by the injection width. To remove this influence, the peak variance was measured at two different positions, one at x=0.2 mm and one position about 1 cm further. Since it was not possible to guarantee that the three peaks would be baseline separated at the first measurement point for every considered velocity, it was preferred to inject the three different coumarin dyes individually. This was also done to alleviate the potential mass overloading problem.

It goes without saying that, given the system is prone to leakages, the stability of the flow was always a major concern. The presence of leakages was checked by checking the mobile phase volume eluting from the column during a period of 12 hours. Measurements carried out on days where the difference was larger than 5% balance were always discarded. To avoid the

presence of leakages, it was necessarily to carefully adjust the force with which all connection fittings were tied.

The obtained plate height values are represented in Fig. 4a. Each data point is the average of three or more successive measurements, with the relative standard deviations always smaller than 5 %. The obtained plate height values all clearly fall below the "traditional" $H=2d_p$-limit that is traditionally expected for a packed column.[3,8,54] For a more in-depth analysis of the data, it was preferred to plot the data in dimensionless coordinates using $h=H/d_p$ and $v=u.d_p/D_{mol}$ (Fig. 4b) and to compare them with one of the plate height expressions typically used to represent the band broadening in a packed column:[12]

$$h=A'+B'/v+C'v \qquad (2)$$

using A'=1, B'=2, and C'=0.1. As another reference, some recent experimental plate height data obtained under non-retained conditions by Wu et al.[55] on non-porous particle columns have been added as well. These data comply nicely with the theoretical curve predicted by Eq. (2).

As can be noted from Fig. 4b, the presently obtained pillar array data lie well below those recently obtained in packed capillaries of non-porous spheres by Wu et al.[55] under non-retained conditions. Comparing these data with the non-retained data in the pillar array (bottom curve in Fig. 4b), the difference is huge. For the two (slightly) retained component cases (coumarin C460 and C480), the difference with the packed bed data is smaller, but the pillar array data still have a minimum around $h_{min}=1$, which is significantly smaller than the value of $h_{min}=2$ that is traditionally observed in the best possible packed columns and also in the non-porous particle packed capillaries of Wu et al.[55] As can be derived from the plate height calculations performed at various degrees of packing heterogeneity in Billen et al.,[11] this decrease is in line with what can be expected from an improved packing homogeneity.

Fitting the three curves with Eq. (2), the obtained A'-. B'- and C'-term constants (cf. values given in Table 1) are difficult to interpret. The A'-term constants are relatively large. Given that the A'-term constant is in principle an indication for the degree of heterogeneity of a column,[3,4] it is rather surprising to note that the A'-term constants obtained here are not significantly smaller than the A'=0.5-values that are sometimes obtained in the best possible packed beds.[12] The values however lie close to the A'-term constant values obtained under non-retained conditions in De Pra et al.[12] The B'-term constants are relatively small, and

appear to increase very strongly with the retention factor. Given the insecurity about the quality of the employed C8-coatings, and given the uncertainty about the validity of the employed plate height model,[8, 12] it is however preferred to draw no firm conclusions from the obtained A'- and B'-term constants. The C'-term constant of the non-retained coumarin C440 is very small (C'=0.005), while the C'-term constant for the two (slightly) retained components (coumarin C460 and C480) cases is significantly larger than for the non-retained component.
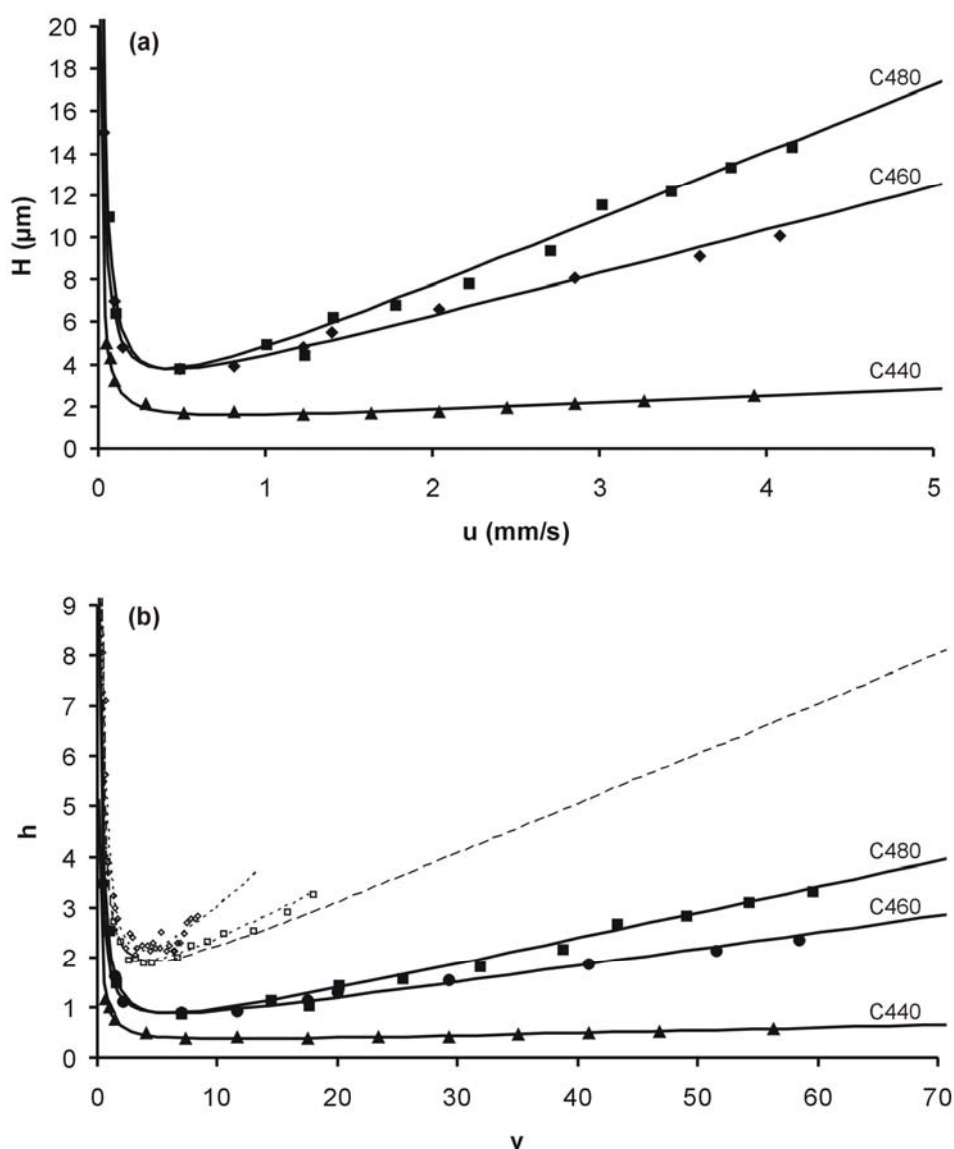
Fig. 4 (a) Van Deemter curves of C440 (▲), C460 (●) and C480 (■) in a mobile phase composition of (30/70, v/v) methanol-water. The respective k' values are k'≅0, k'=0.65 and k'=1.19 **(b)** Dimensionless Van Deemter curve of the data in (a) (same symbols) and comparison with recent experimental values obtained with non-porous packed particles by Wu et al.[55](▫), 3 μm; (◇), 1.5 μm. The dotted lines are obtained by fitting the experimental data with Eq. (2). The dashed curve (– – – –) corresponds to a typical van Deemter curve for a packed bed (Eq. 2). See text for more details.

Again, the obtained values are difficult to interpret because of the lack of a theoretical expression predicting the increase of H with the retention factor k in a pillar array column. Given the resemblance to a monolayer coated open-tubular channel, a first principles guess was made using the Golay-Aris equation for an open-tubular cylindrical capillary.[12,15, 56] This equation predicts an increase of h of 300 % at v=20 when k increases from 0 to 1.19. The current data are of the same order of magnitude. The reduced plate height comparison between the packed and microfabricated columns that is made in Fig. 4b is not entirely fair, since the band broadening in a non-porous system can be expected to be essentially determined by the pore diameter instead of by the particle diameter. The employed reduction parameter (d_p was respectively particle and pillar diameter) used to obtain Fig. 4b is hence most certainly invalid, because the relation between the pore diameter and the pillar (or particle) diameter in a pillar array will certainly be different from that in a packed bed.

Table 1. Fitting parameters for the 3 coumarins in 30/70 (v/v) methanol-water with Eq. (2). The respective r^2 values for C440, C460 and C480 are 0.99, 0.99 and 0.98.

component	A' (/)	B' (/)	C' (/)
C440	0.24	0.70	0.0056
C460	0.45	1.34	0.0337
C480	0.24	1.95	0.0523

In packed columns, a good first approximation for the pore width is that it is about 1/3rd of the particle diameter. In the case of a pillar array, the pore width can be determined more accurately. I.e., at least the width of the pore neck (where the through pores are the smallest) can be directly measured from the SEM's. In the present case, this was equal to 1.7 μm. Using the pore diameter as the reduction basis, the difference between the pillar array and the packed columns is hence considerably larger. For the packed columns, the thus defined h_{min} lies around 6, while for the pillar array a value of h_{min}=2.5 would be obtained. However, since this is all rather speculative, the reduced plate height curves that are obtained using the pore diameter as the reduction basis instead of the particle diameter are not further considered.

Instead, it is preferred to compare the packed column reference and the pillar array data in a geometry-independent manner. As elaborated in Desmet et al.,[57] a column quality assessment method that does not require any assumption about the characteristic size and shape of the support is the so-called kinetic plot representation. One of the members of the kinetic plot family is the plot of Knox' separation impedance number E versus the plate number N. This

plot can readily be established by transforming the experimental (u_0,H)-data couples into a series of corresponding data couples (E,N) using (with K_v the Darcy permeability):

$$E=H^2/K_v \tag{3a}$$

$$N=(\Delta P/\eta)(K_v/u_0H)_{exp} \tag{3b}$$

The E-number combines the plate generation speed with the pressure cost of the separations.[58] Being a dimensionless measure, it has the true meaning of a shape factor, and can therefore be considered as a measure for how well a given support shape is suited to perform rapid chromatographic separations. The lower E, the better suited the support. For the best possible packed bed columns, the E-number generally lies around 2000 to 3000.[12, 58-59] For monolithic columns, having a smaller flow resistance and hence a lower pressure cost, E-numbers as low as E=100-200 can be achieved.[59-60]

One of the interesting features of the (E,N)-kinetic plot is that, if the N-axis is plotted in reverse axis, the obtained curve assumes the same shape as reduced Van Deemter curve. Moreover, since the minimum of the curve corresponds to the velocity also marking the minimum of the Van Deemter curve, and since the data points left of this minimum relate to the B-term dominated velocities, while the data points situated to the right of this minimum relate to the C-term dominated velocities, it is in fact directly related to it.[57] The only additional parameter involved in the plot is the bed permeability. The interference of this additional parameter should however not be considered as a drawback, because the bed permeability interferes in such a way that the plot produces a highly relevant type of information. It directly shows the separation speed as a function of the required plate number (or, equivalently, the employed column length). The vertical difference between the (E,N)-curves of different supports is therefore directly proportional to the difference in separation time needed to achieve a given plate number.

Before Eq. (3) can be used, the value of the column permeability needs to be determined. For a packed column of non-porous particles, this can be calculated using Kozeny-Carman's law,[12] which for a non-porous packing with $\varepsilon=0.4$ yields:

.

$$u_0 = \frac{1}{180} \cdot \frac{\varepsilon^2}{(1-\varepsilon)^2} \frac{\Delta P}{\eta L} d_p^2 \approx \frac{1}{405} \frac{\Delta P}{\eta L} d_p^2 = K_v \frac{\Delta P}{\eta L} \qquad (4)$$

From which the flow resistance Φ can be calculated as: $\qquad \Phi = d_p^2/K_v = 405 \qquad (5)$

Given the strong dependency of the permeability on the external porosity, it is not unexpected to assume that the presently investigated pillar array column with $\varepsilon=0.55$ will have a lower flow resistance, or equivalently, a higher permeability as compared to a packed column with the same particle diameter. Fig. 5a shows the plot of $\Delta P/L$ versus the linear velocity of a non-retained component in the same channel as used to establish the Van Deemter curve shown in Fig. 4. From the slope of the curve, a channel length of 6 cm and a viscosity value of $1.66\ 10^{-3}$ Pa.s at 20 °C,[32] it was found that $K_v = 1.7\ 10^{-13}\ m^2$.

Using the pillar diameter as the reduction basis (however again without having a real physical basis indicating this is the "right" reduction parameter for the permeability), the measured permeability K_v translates (cf. Eq. 5) into a flow resistance of $\Phi=109$. This is significantly smaller than the packed column value, a decrease that can largely be attributed to the more open porous structure of the presently considered pillar array column. The obtained value is in agreement with a CFD study of the permeability of non-porous pillar arrays.[61] This study predicts a value of Φ ranging from $\Phi =274$ over $\Phi =121$ to $\Phi =56$ when the external porosity varies goes from $\varepsilon=0.4$ over $\varepsilon=0.5$ to $\varepsilon=0.6$. Given that the currently tested pillar array has a value of ε around $\varepsilon=0.55$, the experimental value appears slightly larger than what can be theoretically expected. This difference can however most probably be explained by the fact that the contribution of the channel top and bottom wall to the flow resistance effect was not accounted for in the CFD-generated data, while this is inevitably the case in the experimental value.

Considering then that $E=H^2/K_v=h^2\Phi$, it is straightforward to understand that the presently considered non-porous pillar array column with $\varepsilon=55\%$ has a separation impedance that is roughly about 16 times lower than the non-porous packed column data considered here (value based on retained coumarin C460 and C480 data). The factor 16 mentioned above is composed of a factor of 4 for the band broadening (h_{min}^2 decreases 4-fold) and another factor of 4 for the flow resistance (Φ also roughly decreases 4-fold if going from the packed column to the presently considered pillar array column) As can be noted from Fig. 5b, this value is however only reached around the minimum of the (E,N)-curve. As shown in Desmet et al.,[57] the N-coordinate of this minimum (N_{opt}) can be considered as the optimal operating point for

the support. It is the plate number the support can yield whilst experiencing the lowest impedance (provided it is used in a column with the appropriate length). If the same support is used for another plate number, it will experience a larger impedance. The optimum plate number N_{opt} depends on the size of the support (via $N_{opt} \sim d_p^2$),[62] while the E-number only depends on the shape of the support. Knowing this, two main conclusions can be drawn from Fig. 5b.
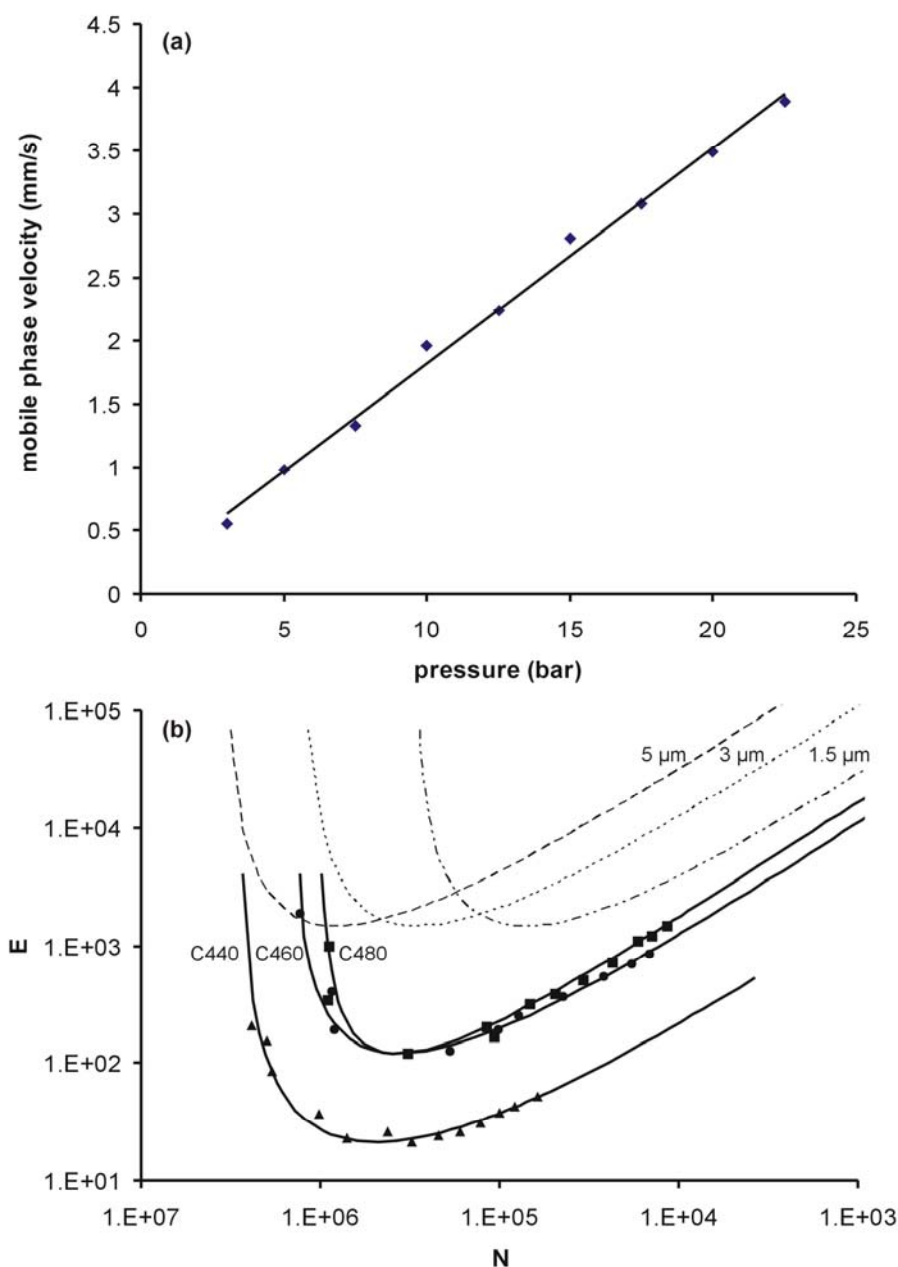
Figure 5. (a) Relation of mobile phase velocity and pressure as measured with C440 in (30/70, v/v) methanol-water. The slope of the linear fit (r^2=0.995) is 0.1705 mm.bar^{-1}.s^{-1}, symbols as in Fig. 4. **(b)** Kinetic plot comparison of the pillar array data shown in Fig. 4a with a set of typical packed column data based on Eq. 2 with A=1, B=2 and C=0.05, and by assuming three different particle size values. The pillar array data have been calculated with ΔP_{max}(pillars)=60 bar (upper limit imposed by potential leakage of Upchurch® Nanoport connectors), while the packed column data have been calculated by assuming ΔP_{max}(particles)=60 bar.

The first one is that the shape of the pillar array column (and especially its high degree of homogeneity and the high external porosity) is clearly better suited to yield rapid separations than the packed bed of particles. This follows from the fact that the pillar array curves lie significantly below that of the three reference packed bed curves (representing different particle size cases). The minimum of the two (weakly) retained component curves lies around E=150. This is as low as the lowest reported values for the current generation of best performing silica monoliths, for which values of the order of E_{min}=100 to 200 have been reported.[59-60] The second conclusion that can be drawn from Fig. 5b is based on the horizontal position of the curve minima for the pillar array column. These show that the current pillar size, yielding an N_{opt} of about N=350,000, is too large to obtain really rapid separations in the practically most relevant range of plate numbers, roughly delimited by N<50,000 or 100,000). To bring the N_{opt} point in this range, so as to maximize the difference with the packed bed curves in this particular range of efficiencies, smaller sized pillars are needed. In Desmet et al.,[62] it has been shown that a decrease in feature size does not change the shape of the kinetic plot curve but simply horizontally shifts the curve in the direction of lower plate numbers, according to $N_{opt} \sim d_p^2$.

It should be remembered that the analysis originating from Fig. 5b only holds for the non-retained or weakly retained component data generated in the present study. It can however nevertheless be inferred that, at least the second point (about the oversized pillars), will still hold under strongly retained conditions.

One of the main future goals should hence be the fabrication of pillar arrays of smaller pillars. There are however limits to the pillar size reduction. The main bottleneck for the pillar size reduction appears to be the existence of a minimal inter-pillar distance below which it is no longer possible to resolve the individual features on the mask.[34-36] The smallest feature that a state-of-the-art deep-UV lithography tool can pattern has a dimension of about 200 nm.[36] In the subsequent etching step, an underetch of 50 nm of the mask material is inevitable. Because this underetch occurs from both sides of a feature, the underetch gives a size reduction of about 100 nm. If a Bosch-type etch process is used, the uncertainty about the pillar diameter is increased with another 100 nm, because of the occurrence of etching scallops having a size of about 50 nm on each pillar side. Using a cryogenic etching process, the formation of scallops can be prevented. Adding the minimal feature size on the mask to the above etching uncertainties, it can be concluded that the minimal distance between two pillars will be somewhere between 0.3 and 0.4 μm with cryogenic and Bosch etching

respectively. For $\varepsilon=0.55$, where the ratio between the inter-pillar distance and the pillar diameter is 0.39, this means that the minimal pillar size that can be produced will be of the order of 0.75 µm to 1,0 µm. This is respectively 5.7 and 4.3 times smaller than in the currently considered array, hence allowing to shift the N_{opt}-point over a factor of 32 to 18 (cf. the $N_{opt} \sim d_p^2$-law). This shift is of about the right magnitude to lower the N_{opt}-point from its current value of $N_{opt}=350,000$ into the practically most relevant range of $N=5,000$ to $N=50,000$ plates. Being able to shift the N_{opt}-point is important because it allows to maximize the difference between the packed column curves and the pillar array curve in the plate number range of interest.

4.5 Conclusions

It is possible to perform high performance reversed-phase LC separations in microfabricated pillar array columns. Using arrays of non-porous silicon pillars with a diameter of approximately 4.4 µm and an external porosity of 55 %, a three component mixture could be separated in three seconds. Excluding the side-wall region, plate heights of about H=4 µm were obtained at a mobile phase velocity around u= 0.5 mm/s and for slightly retained component conditions (retention factor k=0.65 to 1.2). In reduced terms, such plate heights are as low as $h_{min}=1$. Since also the flow resistance of the column is much smaller than in a packed column (mainly because of the higher external porosity of the pillar array), the separation impedance of the array was as small as E=150, i.e., of the same order as the best currently existing monolithic columns. A moderating remark that however needs to be made is that the loadability of the non-porous pillars is smaller than that of the mesoporous monolits. On the other hand, with an external porosity of $\varepsilon=0.55$, the pillar array column still has a large margin for pursuing even much smaller E-number by further increasing the external porosity. At pH=3, yielding very low retention factors (k'=0.13 and 0.23), plate heights as low as H=2 µm were realized, yielding a separation of the three-component mixture with an efficiency of N=4000 to 5000 plates over a column length of 1cm. At higher retention factors, significantly larger plate heights were obtained. More research is however needed before any firm conclusions on this issue can be made.

Future work should aim at preventing or alleviating the side-wall band broadening, the production of arrays with smaller inter-pillar distances, and also at finding methods to produce porous pillars.

Symbols

E	separation impedance (/)
k'	phase retention coefficient (/)
k''	zone retention coefficient (/)
H	height of a theoretical plate (m)
h	reduced plate height (/)
N	number of theoretical plates (/)
d_p	pillar diameter (m)
ε	external porosity (/)
C_x	concentration at position x (mol/m^3)
C_{max}	maximum concentration (mol/m^3)
σ_x	spatial peak standard deviation at position x (m)
A'	see Eq. 2 (/)
B'	see Eq. 2 (/)
C'	see Eq. 2 (/)
K_v	Darcy permeability (m^2)
ΔP	pressure drop (N/m^2)
η	dynamic viscosity (kg/ms)
u_0	mobile phase velocity (m/s)
Φ	flow resistance (/)
L	column length (m)
N_{opt}	N coordinate of the minimum in a (E,N) curve (/)
D_{mol}	molecular diffusion coefficient (m^2/s)

Abbreviations

HPLC	high performance liquid chromatography
LC	liquid chromatography
RP-LC	reversed phase liquid chromatography

References

1. Kirkland, J.; DeStefano, J.J., *J. Chromatogr., A* **2006**, *1126*, 50-57.
2. He, B.; Tait, N.; Regnier , F.E., *Anal. Chem.* **1998**, *70*, 3790-3797.
3. Knox, J.H., *J. Chromatogr., A* **1999**, *831*, 3-15.
4. Knox, J.H., *J. Chromatogr., A* **2002**, *960*, 7-18.
5. Giddings, J.C., Dynamics of Chromatography – Part I, Marcel Dekker, New York, 1965.
6. Wen, E.; Asiaie, R.; Horváth, C., J. Chromatogr., A **1999**, *855*, 349-366.
7. Stol, R.; Poppe, H.; Kok, W. T., Anal. Chem. **2001**, *73*, 3332-3339.
8. Koch, D.L.; Brady, J.F., J. Fluid. Mech. **1985**, *154*, 399-427.
9. Tallarek, E.; Bayer, E.; Guiochon, G., J. Am. Chem. Soc. **1998,** *120*, 1495-1505.
10. J. De Smet, P. Gzil, N. Vervoort, G.V. Baron, G. Desmet, *Anal. Chem.* **2004**, *76*, 3716-3726.
11. Billen, J. Gzil, P.; Vervoort, N.; Baron, G. V.; Desmet, G., *J. Chromatogr., A* **2005**, *1073*, 53-61.
12. Neue, U.D., HPLC Columns: Theory, Technology, and Practice, John Wiley & Sons, New York, 1997.

13.   Guiochon, G., *Anal. Chem.* **1981**, *53*, 1318-1325.
14.   Giddings, J.C., *Anal. Chem.* **1965**, 37, 60-63.
15.   Poppe, H., *J. Chromatogr., A* **2002**, *948*, 3-17.
16.   Regnier, F.E., *J. High Resol. Chromatogr.* **2000**, *23*, 19-26.
17.   Slentz, B.E.; Penner, N.A.; Regnier, F., *J. Sep. Sci.* **2002**, 25, 1011-1018.
18.   W.J. Park, J.H. Kim, S.M. Cho, S.G. Yoon, S.J. Suh, D.H. Yoon, *Surf. Coat.Tech* **2003**, *171*, 290-295.
19.   Madou, M., *Fundamentals of Microfabrication*, CRC Press, London, 1997.
20.   Mogensen, K.B.; Eriksson, F.; Gústafsson, O.; Nikolajsen, R.P.H. ; Kutter, J.P., *Electrophoresis* **2004**, *25*, 3788-3795.
21.   Ricoul, F.; Bouffet, S., Sarrut, N.; Mittler, F.; Constantin, O.; Blanc, R.; Sudor, J.; Vinet, F.; Garin, J.; Vauchier, C., 29 th International Symposium on High Performance Liquid Phase Separations and Related Techniques, Stockholm-Sweden, June 2005.
22.   De Pra, M.; Kok, W.Th.; Gardeniers, J.G.E.; Desmet, G.; Eeltink, S.; van Nieuwekasteele, J.W.; Schoenmakers, P.J., *Anal.Chem.* **2006**, *78*, 6519-6525.
23.   M.T. Blom, E. Chmela, R.E. Oosterbroek and A. van den Berg, *Anal. Chem.* **2003**, *75*, 6761-6768.
24.   E.Chmela, R. Tijssen, M.T. Blom, H.J.G.E. Gardeniers and A. van den Berg, *Anal. Chem.* **2002**, *74*, 3470-3475.
25.   O'Neill, A. P.; O'Brien, P.; Alderman, J.; Hoffman, D.; McEnery, M.; Murrihy, J.; Glennon, J.D., *J. Chromatogr., A* **2001**, *924*, 259-263.
26.   De Malsche, W; Clicq, D.; Eghbali, H.; Fekete, V.; Gardeniers; H.; Desmet, G., *Lab Chip* **2006**, *6*, 1322-1327.
27.   McEnery, M.; Tan, A.; Alderman, J.; Patterson, J.; O'Mathuna, S.C.; Glennon, J.D., Analyst **2000**, *125*, 25-27.
28.   Kutter, J.; Jacobson, S.; Matsubara, N.; Ramsey, M., Anal. Chem. **1998**, *70*, 3291-3297.
29.   Kutter, J. P.; Jacobson, S.C.; Ramsey, J.M., Anal. Chem. **1997**, *69*, 5165-5171.
30.   Clicq, D.; Pappaert, K.; Vankrunkelsven, S.; Vervoort, N.; Baron, G. V.; Desmet, G., Anal. Chem. A-pages **2004**, *76*, 430A-438A.
31.   Shalliker, R.A., Broyles, B.S.; Guiochon, G., *J. Chrom. A.* **1999**, *865*, 73-82.
32.   Li, J.; Carr, P.W., *Anal. Chem.* **1997**, *69*, 2550-2553.
33.   Vervoort, N.; Billen, J.; Gzil, P.; Baron, G.V.; Desmet, G., *Anal. Chem.* **2004**, *76*, 4501-4507.
34.   de Boer, M.J.; Gardeniers, J.G.E.; Jansen, H.V.; Smulders, E.; Gilde, M.-J.; Roelofs, G.; Sassareth; J.N.; Elwenspoek, M., *J. Microelectromech. S.* **2002**, *11*, 385-401.
35.   Boufnichel, M.; Lefaucheux, P.; Aachboun, S.; Dussart R.; Ranson, P., *Microelectron. Eng.* **2005**, *77*, 327-336.
36.   Ronse, K., *C.R. Physique* **2006**, *7*, 844-857.
37.   Knox, J. H.; Parcher, J.F., Anal. Chem. **1969**, *41*,1599-1606.
38.   Baur, J.E.; Kristensen, J.E.; Wightman, R.M., Anal. Chem. **1988**, *60*, 2334-2338.
39.   Yun, T.; Guiochon, G., J. Chromatogr., A **1994**, *672*, 1-10.
40.   Shalliker, R. A.; Broyles, R.S.; Guiochon, G., J. Chromatogr., A **2000**, *888*, 1-12.
41.   Miyabe, K.; Guiochon, G., J. Chromatogr., A **1999**, *857*, 69-87.
42.   Mukhopadhyay, R., Anal. Chem. A-pages **2005**, *77*, 429A-432A.
43.   Vratzov, B.; Fuchs, A.; Lemme; M., Henschel; W.; Kurz, H.l, *J. Vac. Sci. Technol.* **2003**, *21*, 2760-2764.
44.   Xing, R.; Wang, Z.; Han, Y., *J. Vac. Sci. Technol.* **2003**, *21*, 1318-1323.
45.   Dutta, D.; Leighton, D.T, *Anal. Chem.* **2001**, *73*, 504-513.
46.   Wu, C.-H.; Yang, R.J., *Electrophoresis* **2006**, *27*, 4970-4981.

47.   Ermakov, S.; Jacobson, S. C.; Ramsey, J. M, *Anal. Chem.* **2000**, *72*, 3512-3517.

48.   Fu, L.-M.; Yang, R.-J.; Lee, G.-B.; Liu, H.-H., *Anal. Chem.* **2002**, *74*, 5084-5091.

49.   Hübner, J..; Mogensen, K.L.; Jorgensen, A.M.; Frijs, P.; Telleman, P.; Kutter, J., *Rev. Sci. Instrum.* **2001**, *72*, 229-233.

50.   Mogensen, K.B.; El-Ali, J.; Wolff, A.; Kutter, J. P., *Appl. Optics* **2003**, *42*, 4072-4079.

51.   Mogensen, K.B.; Petersen, N.J.; Hubner, J.; Kutter, J.P., *Electrophoresis* **2001**, *22*, 3930-3938.

52.   Petersen, N.J.; Mogensen,K.B.; Kutter, J.P., *Electrophoresis* **2002**, *23*, 3528-3536.

53.   Moore, A.W.; Stephen, C. ; Jacobson, C. ; Ramsey, J.M., Anal. Chem. **1995**, *67*, 4184-4189.

54.   Poppe, H., J. Chromatogr., A **1997**, *778*, 3-21.

55.   Wu, N.; Liu, Y.; Lee, M. L., *J. Chromatogr., A* **2006**, *1131*, 142-150.

56.   Desmet, G.; Baron G. V., *J. Chromatogr., A* **2000**, *867*, 23-43.

57.   Desmet , G.; Clicq, D.; Gzil, P., *Anal. Chem.* **2005**, *77*, 4058-4070.

58.   Bristow, P.A., Knox, J.H., Chromatographia **1977**, *10*, 279-289.

59.   Ishizuka, N.; Kobayashi, H.; Minakuchi, H.; Nakanishi, K.; Hirao, K.; Hosoya, K.; Ikegami, T.; Tanaka, N., *J. Chromatogr., A* **2002**, *960*, 85-96.

60.   Hara, T.; Kobayashi, I.; Nakanishi, K.; Tanaka, N., *Anal. Chem.* **2006**. *78*, 7632-7642.

61.   Gzil, P.; Vervoort, N.; Baron G.V.; Gert Desmet, *Anal. Chem.* **2004**, *76*, 6707-6718.

62.   Desmet, G.; Cabooter, D.; Gzil, P.; Verhelst, H.; Mangelings, D.; Vander Heyden, Y.; Clicq, D., *J. Chromatogr., A* **2006**, *1130*, 158-166.

63.   Oosterbroek, R.E.; Hermes, D.C.; Kakuta, M.; Benito-Lopez, F.; Gardeniers, J.G.E.; Verboom, W.; Reinhoudt, D.N.; van den Berg, A., Microsyst. Technol. **2006**, *12*, 450-454.

64.   Tiggelaar, R.M; ., Benito-López, F.; Hermes, D.C.; Rathgen, H.; Egberink , R.J.M.; Mugele, F.G.; Reinhoudt, D.N., van den Berg, A.; Verboom, W.; Gardeniers, J.G.E. *Chemical Engineering Journal* **2007**, *131*, 163–170.

Chapter 5: Pressure-driven reversed-phase chromatography in microstructured pillars with UV-Vis absorbance detection using microfabricated waveguides

5.1 Abstract

We report on the development and characterization of a fluidic chip wherein we integrated a pillar array column with a waveguide suitable for UV-Vis detection, using plasma enhanced chemical vapour deposition of SiO_2 and SiON and subsequent deep reactive ion etching to fabricate the devices. Using a Mercury lamp as the light source and a photomultiplier tube as the detector, a van Deemter curve was established, yielding a minimal plate height of 15 μm. This is significantly larger than the 5 μm plate height value that was measured for coumarin 480 in methanol in the central part of the channel using a fluorescence microscope. This difference is due to the fact that the UV-detection cell cannot avoid measuring the strong additional band broadening originating from the flow resistance mismatch between the central and the side-wall parts of the channel. Coating the pillars with a C8 stationary phase, the integrated detection/separation device could be used to separate a mixture of acetophenone, valerophenone and hexanophenone within 2 min and detecting it at the end of the channel.

5.2 Introduction

In the field of pressure-driven liquid chromatography, it has been recognized for many years that a reduction of the packing disorder of the traditionally employed packed beds would lead to a significant increase of the separation efficiency.[1] Recently, this advantage has been demonstrated experimentally in an array of deep reactive ion etched pillars coated with a C8 phase, using a fluorescence microscope and a CCD-camera to record the separation of 3 coumarins within 3 s yielding 5000 plates in 1 cm.[2] Given the typical plug volumes of a few nl in this device, it is a big challenge to couple this system to a detector that allows monitoring the separation of non-labeled components because it is extremely difficult to guide these plugs undisturbed towards a sufficiently sensitive detector.

During the past decade, a lot of research has been carried out on micro-chip separation devices using UV-Vis absorbance as the detection mode.[3-8] In order to increase the path length, different approaches such as the use of a multi-reflection cell,[9-10] a Z-cell[11] and a U-cell[12-13] have been presented. In order to maintain the linearity and sufficient detection

sensitivity, the path length was limited in these cases. A true break-through was reached when Kutter and co-workers integrated micro-fabricated waveguides to deliver and capture the light directly at the channel area. Besides a U-channel configuration (path length of 750 µm), they also fabricated wider channels of 500 µm width, hence avoiding detection induced band broadening. Detection limits in the µM orange have been demonstrated earlier in this configuration. There are however still losses due to stray light. Recently, a plano-convex lens was integrated in PMMA to collimate the incoming light and to reduce signal losses.[14] This strategy reduced stray radiation from ~ 32 % to ~4 %. In the present contribution, a pressure-driven reversed-phase pillar array channel is presented. The detection is mediated by UV-Vis absorbance using (non-collimated) waveguides. The focus is on the fluidic performance of the system and the practical hurdles that are limiting. For the optical characterization of the system, the reader is referred to.[7-8]

5.3 Experimental

5.3.1 Microfabrication

A 0.5 mm thick and 100 mm diameter (100) Si wafer was wet thermally oxidized at 1150 °C for 15 h, leading to a thickness of 2 µm of SiO_2 (bottom cladding layer). Next, a layer of 7 µm SiON was PECVD deposited (the core layer), then 1.5 µm SiO_2 was PECVD deposited on top (cladding layer), after which annealing in N_2 occured at 1100 degrees C for 8 h. Then, a layer of 1,5 µm a-Si was LPCVD-deposited, functioning as a hard mask in the subsequent SiON and SiO_2 etching. Next, the first lithography step was executed (1.5 thick) defining the pillar array and the waveguide. The exposed a-Si was DRIE etched until the SiON-interface was reached and the resist was stripped. Then the SiON was DRIE etched all the way through the SiO_2 until the Si interface and the a-Si was removed by DRIE etching. Further, a second lithography step (photoresist thickness of 9,5 µm) defined the supply channels, which were subsequently 100 µm deep RIE etched in the Si. The resist was then stripped and 1 µm PECVD SiO_2 was deposited (top cladding layer), then annealing occured at 1000 degrees C for 4 h. Then a 1.0 µm thick layer of SiO_2 was LPCVD deposited, after which it was annealed at 1000 °C for 4 h. Then, a layer of 100 nm of a-Si was LPCVD deposited in order to provide electrical contact for the subsequent anodic bonding. The a-Si was then wet etched (poly-Si etch consisting of nitric acid, HF and water) at the area of the waveguide using a photolithography mask, in order to not impede the transmission of light at the etched

absorption cell. On a 0,5 mm thick and 100 mm diameter borofloat substrate, a CO_2 laser marking step then defined access holes on a powderblast foil, the holes were then generated by powderblasting (particles of 50 μm). Finally the glass substrate was placed in an ultrasonic bath for 30 min and piranha cleaned, after which they were aligned and anodically bonded. See Fig. 1 for a summary of the process.

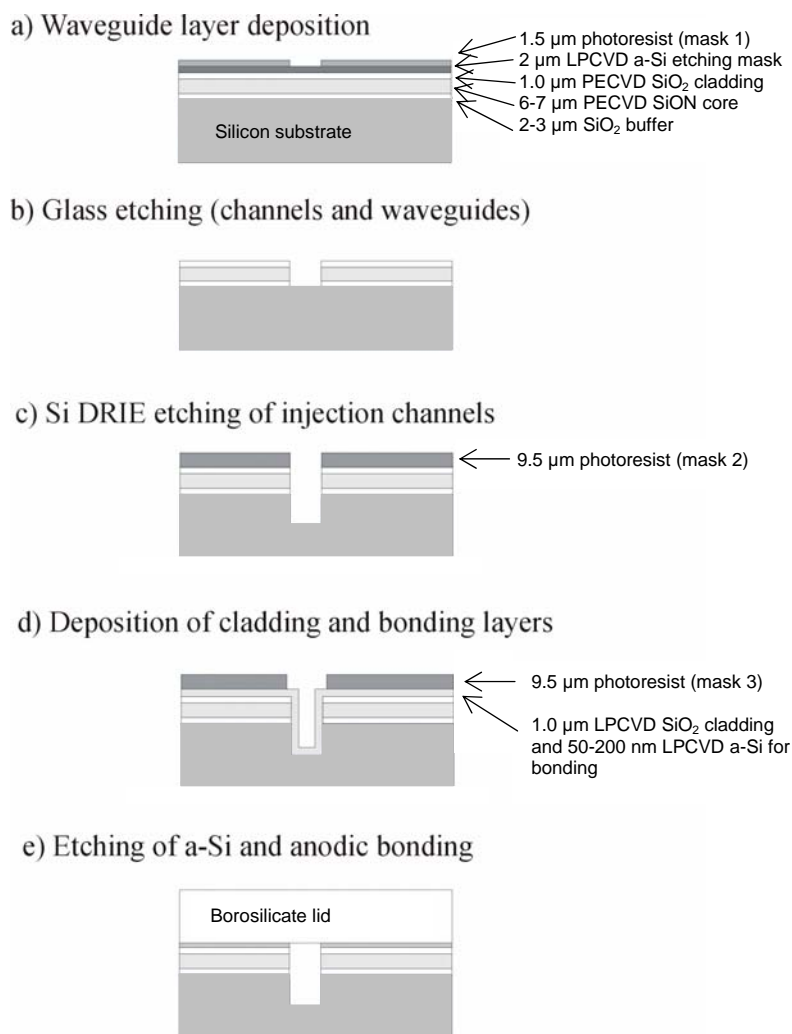### 5.3.2 Chemicals and coating procedure

The solutions of thiourea, acetophenone, valerophenone, hexanophenone were taken from a stock solution of 50 mg/ml in MeOH (UV absorbing analytes standards, Sigma-Aldrich).
The coating procedure consisted in wetting the channels with MeOH, conditioning with toluene for 2 h after which the coating solution (15 % octyldimethylchlorosilane in toluene) was sent through the channel at 30 bar overnight. Then the channel was flushed again with toluene and with MeOH. All solutions were filtered with 0.2 μm filters.

5.3.3 Detection

Light of 254 nm from a 100 W Mercury lamp was used for the absorbance measurements. Other wavelengths were cut off with a 254 nm bandpass filter. A UV transparent fibre with a core diameter of 50 μm was used for coupling the light source and the photomultiplier tube with the microfluidic chip. The fibers were aligned with the waveguides using a XYZ positioning stage from Newport and permanently attached by hardening a UV curing optical adhesive that is transparent at 254 nm (Epotek 09146; Epoxy Technology, Billerica), see Fig. 2. A more robust hardening was done with another UV-curing glue (NOA 63; Norland Products). To lower the baseline noise, a chopper along with a lock-in amplifier was used.
The separations were visualized using an air-cooled CCD fluorescence camera (ORCA-ERC4742, Hamamatsu Photonics, Belgium) mounted on the video adapter of the microscope. The video images were subsequently analyzed with the accompanying simple-PCI [®] 5.1 software. The microscope was mounted on a breadboard (M-IG 23-2, Newport, The Netherlands), together with a linear displacement stage (M-TS100DC.5, Newport) and a speed controller (MM, 4006 Newport). For the evaluation of the separation and band broadening properties, the coumarin dyes C440 (1.10^{-4} M, CAS No. 26093-31-2, Acros Organics, Belgium), C460 (1.10^{-4} M, CAS no. 91-44-1) and C480 (3.10^{-4} M, Cas no. 41267-76-9) (Fluka, Belgium) were used.

a) Waveguide layer deposition

1.5 μm photoresist (mask 1)
2 μm LPCVD a-Si etching mask
1.0 μm PECVD SiO₂ cladding
6-7 μm PECVD SiON core
2-3 μm SiO₂ buffer

Silicon substrate

b) Glass etching (channels and waveguides)

c) Si DRIE etching of injection channels

9.5 μm photoresist (mask 2)

d) Deposition of cladding and bonding layers

9.5 μm photoresist (mask 3)

1.0 μm LPCVD SiO₂ cladding
and 50-200 nm LPCVD a-Si for
bonding

e) Etching of a-Si and anodic bonding

Borosilicate lid

Fig 1. Main steps in the process flow of the micro-fabrication of the device.

5.3.4 Injection and separation procedure

The injection is performed by means of an automated valve system, controlled with a C++ program, as described in.[2] During the actual sample injection step, the automated valve system ensures that the inlet and the outlet of the mobile phase circuit are closed. During the subsequent sample separation, the inlet and the outlet of the sample injection circuit are diverted to a high flow resistance capillary, allowing for the existence of a small leakage flow and thus avoiding tailing. The flow force originates from separate nitrogen pressurized vessels controlled using 2 mass flow controllers (Bronkhorst, The Netherlands), allowing to perform the injection and propagation step at different pressures at a controlled fashion without suffering from control delay issues. Interfacing with the chip with the supply tubings occurs with commercially available Upchurch Nanoport® connectors, that are screwed in a house-made aluminum holder.
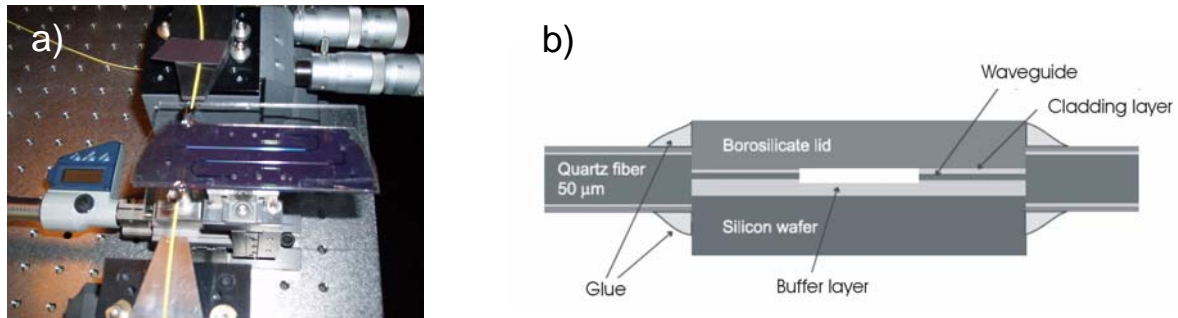
Fig. 2. a) Positioning of the fibres at the xyz-micro-positioning stage. In this picture, the wafer and the fibre are glued on the same PMMA substrate. Any stress on the wafer affects the positioning of the fibre with respect to the wafer and causes misalignment of the fibre and the waveguide **b)** Interfaces of the fibres and the waveguides (taken from [8]).

5.4 Results

5.4.1 Microfabrication

The pillar array and the interfacing regions with the injection and detection zone are depicted in Fig. 3. Because of the 10 mm wafer format and to allow the positioning of 2 channels on the same wafer, the length of the pillar zone was limited to 4.9 cm. In Fig. 3a, the deeper injection channels (100 μm) can be observed. This larger depth is necessary to avoid asymmetric peaks during the filling of the injection zone.[2] At the other end of the pillar array, the waveguides are positioned (Fig 3b). The SiON core material is surrounded by SiO_2 in the vertical direction, whereas in the horizontal direction the cladding layer consists of an air zone (the regions adjacent to the waveguide is etched away). It is also visible that a small wall is present between the waveguide and the channel, this is necessary to provide sealing of the fluidic channel. It is known from previous experiments performed by Mogensen et al. that this small wall does not generate too much sensitivity losses. Typical detection limit values that can be achieved with this set-up are of the order of μM.[7-8]

The shape of the pillars can be inspected in more detail looking at Fig. 4. An important issue to minimize the plate height of the system is the absence of taper of the pillars, in order to have an equal flow resistance at the top and the bottom of the pillars. In the produced chips, the top of the pillars was curved and a relatively high taper was present (Fig. 4b).

Two types of chips were made. The difference between the two designs is related to the last a-poly Si deposition step, which is required for anodic bonding is also covering the waveguides and hence blocking the light through it. In the first design, this layer was removed locally at

the area of the whole channel (leaving a not bonded area between the pillars and Borofloat substrate). In the second design, the a-Si was only locally removed at the area of the waveguides (allowing bonding of the pillars to the top substrate). Even though the a-Si is quite rough (Fig. 5), no problems concerning the bonding and subsequent pressurizing of the channel were observed. Pressures up to 40 bar could be applied on the mobile phase at the inlet of the chip without detecting any leakages.

5.4.2 Interfacing and detection

The linear region of the absorbance versus analyte concentration typically started at around 5 mM down to lower concentrations. The detection limit on this system varied from chip to chip but was mostly below some tens of µM (the detection limit mainly depends on the quality of the fibre and chip cleavage, and also on the manual alignment procedure).
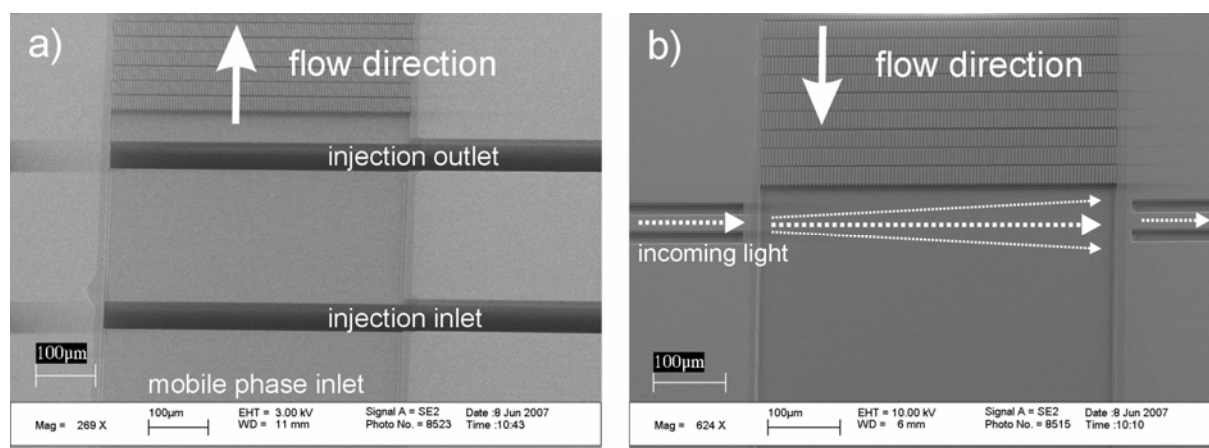
Fig. 3 a) Injection zone. The length of the injection zone is 250 µm. During the injection, an external pressure is applied at the injection inlet. During this event, the injection outlet is open and the mobile phase inlet and outlet is closed. During the mobile phase propagation, the injection inlet is closed, whereas the injection outlet is switched to a flow resistance to provide a small leakage flow to avoid tailing. **b)** Detection zone. the waveguides are positioned immediately after the pillar array. A small amount of light leaving the light-delivering waveguide is lost due to stray light.

Another important point concerning leakages was the swelling or drifting of the glue around the optical fibers, causing misalignment of the fibers with respect to the waveguides.

Both the chip and the fibres were glued on the same PMMA substrate, the fibres were very prone to misalignment when the nanoports were screwed into the holder (and a stress was generated on the wafer and thus also on the glued fibres). To resolve this, the holder had to be adapted, allowing to directly glue the fibres on the wafer independently of the microfluidic holder.
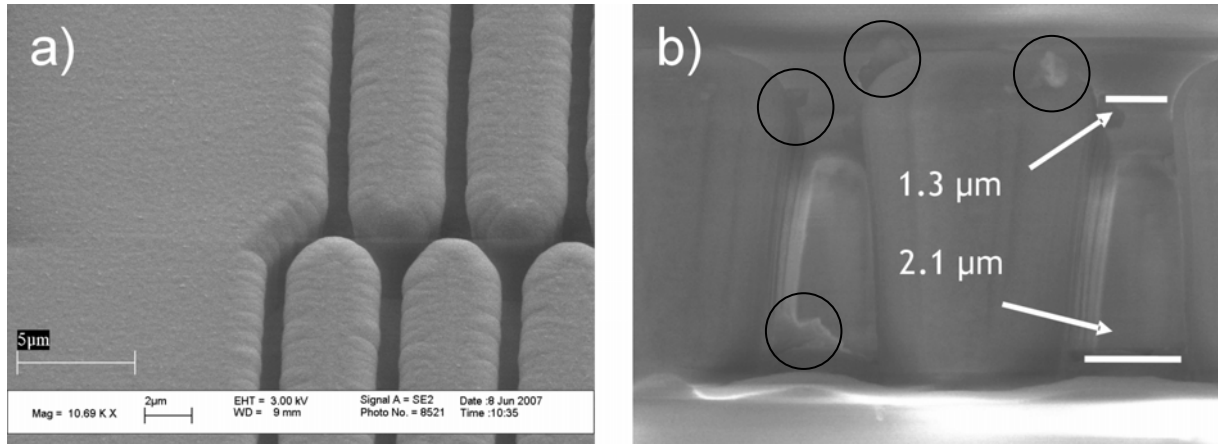
Fig. 4 SEM picture of the pillars **a)** top-view of the side wall region. Even though the distance between the pillars and the distance between the side wall and the nearest pillar appear to be the same, the local flow resistance is different at the side wall region. **b)** side-view picture depicting the taper of the pillars after bonding and cleaving the substrate. The aggregations (see circles) are due to the bad quality of the coating. The voids between the top substrate and the pillars are expected to be an additional band broadening source.

5.4.3 Band broadening

In order to study the quality of the injection, coumarin dye plugs were injected (Fig 6a). The peak widths were typically of the order of 200 μm, this is slightly less than the length of the injection zone (250 μm) because part of the plug is diverted to an external resistance to avoid tailing.
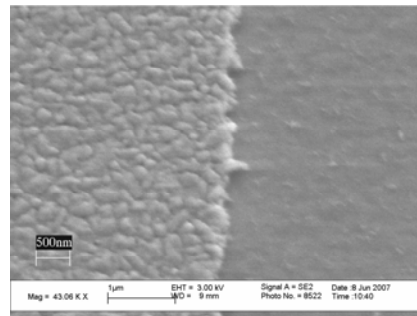

Fig. 5. SEM picture of the a-Si (left) and the SiO_2 layer (right). The roughness of the a-Si does not pose any problems for the bonding.

In order to study the intrinsic band broadening behaviour of the pillar array (excluding any side wall region effects), the plate height in the central zone of the channel was determined using:

$$H = \frac{\Delta\sigma_x^2}{\Delta x},$$
(1)

with σ_x the spatial standard deviation as determined by fitting the concentration profile on a Gauss curve. Measuring the peak broadening in the central part of the channel within the first 2 mm for the dye C480 in methanol with a CCD camera (Fig 6), a plate height of 5.2 μm was obtained for a velocity of 0.4 mm/s. Next, the total plate height (including the side-wall effect) was determined.
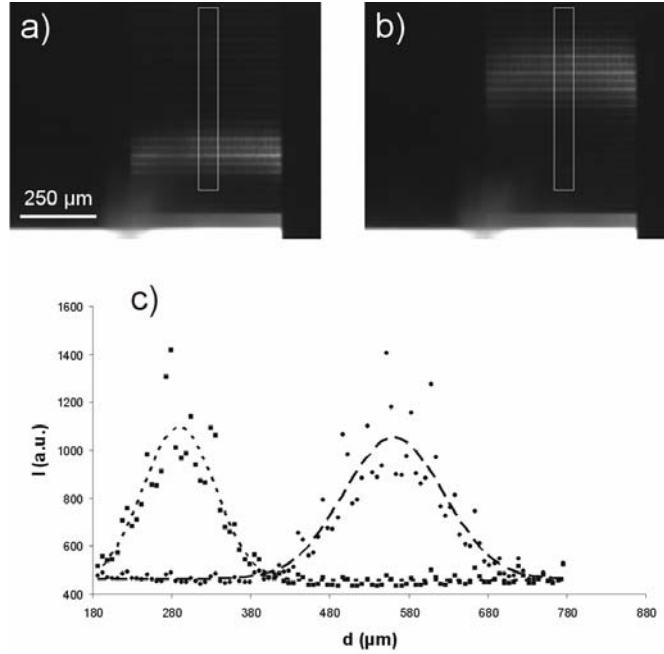
Fig. 6 Propagation of an injected plug of coumarin C480 in MeOH travelling at a velocity of 0.4 mm/s, recorded with a CCD camera. **a)** At around 300 μm downstream the injection slit no side wall effect is yet visible **b)** The peak has travelled 270 μm further, a delay zone at the sidewall region is visible now c) The central part of the peak is averaged to establish an axial concentration profile that is not influenced by the side wall region. Fitting the recorded plate height with a gauss curve (dashed lines), the resulting plate height is H=5.2 ± 1.2 μm (n=5).

This was done by monitoring a passing peak at the end of the pillar array (Fig 7a). This yielded peaks that suffered from tailing. These non-Gaussian peaks should therefore be analysed using the momentum method. A moment of order k is defined as:[15]

$$M_k = \frac{\int_0^\infty t^k C(t)dt}{\int_0^\infty C(t)dt} \; , \tag{2}$$

with C(t) the concentration at the monitor plane at time t.

To verify whether the contribution of the side wall effect to the plate height varies along the length of the channel, plate heights for C480 were measured at different positions in the

channel. This result is given in Fig 8, clearly showing that for both velocities the plate height has reached a constant value for both velocities within the first cm of the channel.

A van Deemter curve was established for thiourea in MeOH using the waveguide in UV-Vis absorbance mode, yielding minimal plate heights of around 15 μm (Fig. 9). This is a very high value, given the fact that in a 2 D sidewall-less array of pillars with these dimensions (without taper), a value below 2 μm is expected.[16-17]

5.4.4 Coating

The employed coating procedure was the same as in [2], which is known to be a very straightforward procedure for coating circular Si pillars (that were wet thermally oxidized for a thickness of about 100 nm) with an inter pillar distance of about 1.5 μm.
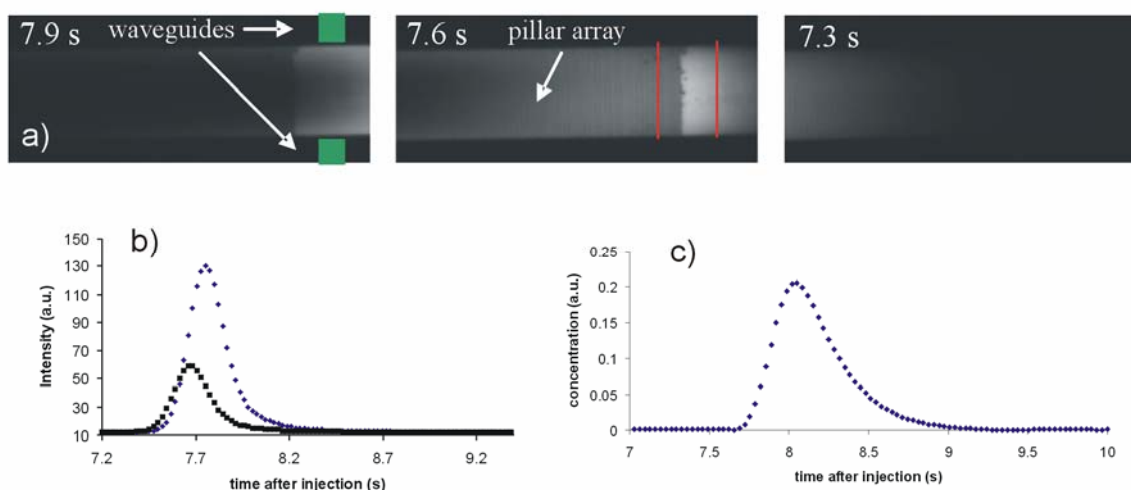
Fig. 7 Observation of arriving plugs at the waveguide area. **a)** CCD camera generated pictures during the passage of the peak. At 7.3 s, a narrow front is visible, whereas at 7.9 s a strong tailing at the sidewall area can be observed. **b)** Chromatogram obtained at 4.85 and at 4.9 cm downstream the injection slit (respectively in the end of the pillar bed and just after it) using a monitor line of 6 μm wide (see red lines in fig 6a). The σ_t values are calculated using the moment method (see text) and are 0.164 s and 0.158 s for the first and the second monitor line, respectively. The associated plate heights are respectively 20.7 μm and 19.0 μm. **c)** Chromatogram obtained with the waveguide for thiourea in MeOH (σ_t=0.237 s, H=42.9 μm).

During the development of the coating procedure in [2], it was observed that the inter-pillar distance had a significant influence on clogging in pillar arrays. When working with a C18 (octadecyldimethylchlorosilane) phase in the pillar array described in [2], clogging occurred frequently. When working in more porous arrays of inter pillar distances of about 2.5 μm, it was more straightforward to coat with a C18 phase. There is hence an indication that smaller dimensions somehow have an influence on the clogging behaviour. The C8

(octyldimethylchlorosilane) however, has been successful in the different configuration described above. It was hence decided to use the C8 phase in the chips
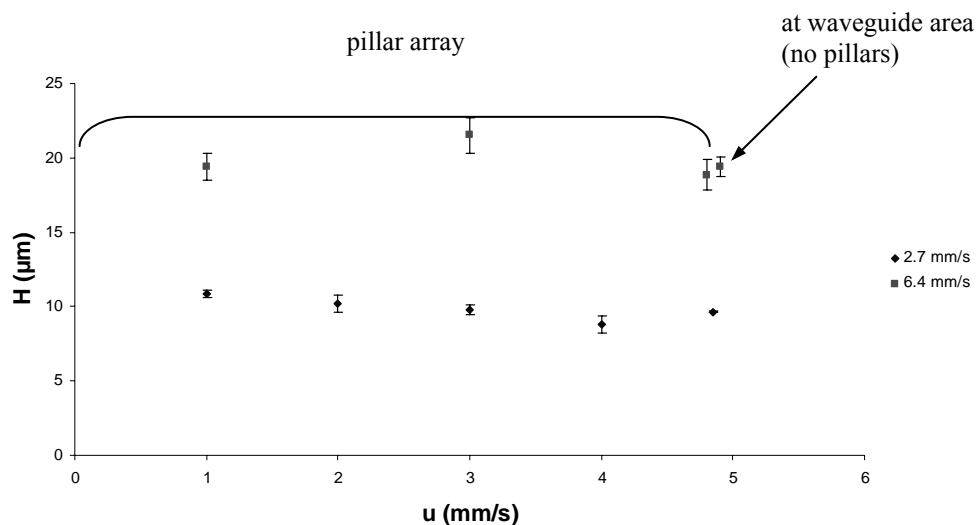
Fig. 8 Evolution of the plate height (H) during the course through the column of coumarin C480 in MeOH at 2.7 and 6.4 mm/s, as monitored with a CCD camera. The monitor plane was the size of 1 pixel, i.e. 6 μm. For the 6.4 mm/s series, the plate height was also determined just after the pillar array, where the waveguide is positioned (see arrow).

produced in the present study as well. It turned out however, that clogging was unavoidable (Fig. 10). Sometimes complete blockage of the channel occurred very fast, sometimes a flow could be generated and plugs could be injected and detected.
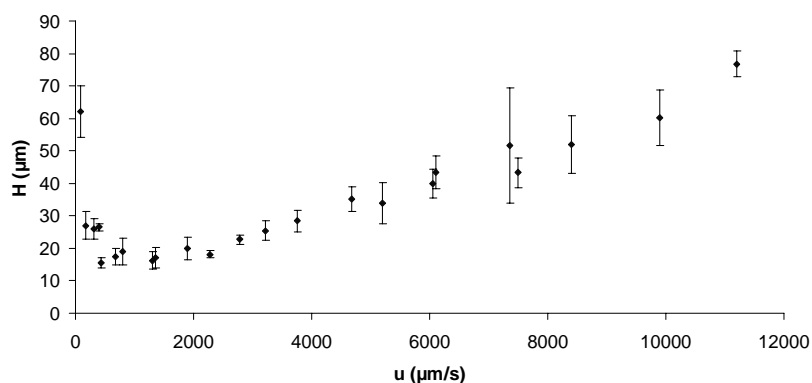
Fig. 9 Van Deemter plot of thiourea in MeOH (4 mM), obtained in a channel without stationary phase and with pillars that are not bonded with the top substrate.

In order to see what was going on with the coating in detail, the chip had to be broken and inspected with the SEM. It is not possible to remove the Borofloat lid by HF etching because then the pillars partly made of SiO_2 would also be etched. Figure 10 depicts an example of a channel after coating. After intensive clogging, also the sensitivity of the optical system was influenced due to the presence of aggregations at the waveguides (Fig. 10). A 3 component separation was performed in this channel, as depicted in Fig. 11. Even though a separation is

obtained, the plate heights as determined at the detector are more than 200 μm. This value is extremely high compared with other pillar array configurations of similar dimensions.[2]
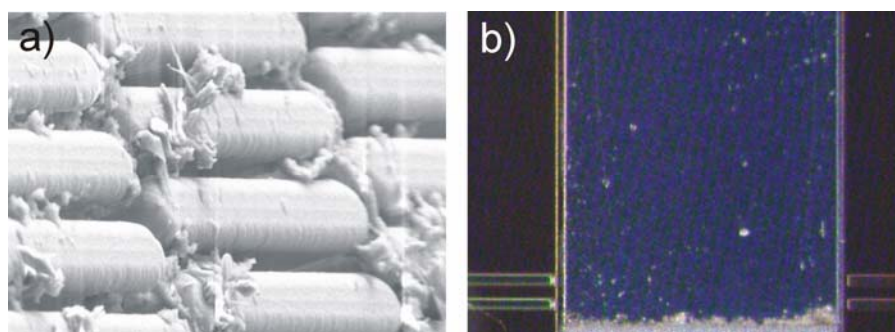
Fig. 10. a) clogging due to an unsuccessful coating **b)** Optical microscope picture of the waveguide region. Gathering of dirt at the waveguide can block the passing light completely.

Attempts were made to avoid clogging such as changing the in-line filters, performing longer flushing times with methanol and toluene (to avoid contact of the C8 and water), applying shorter coating times and reducing the concentration of the C8 from 15 % to 7.5 %, but without success.
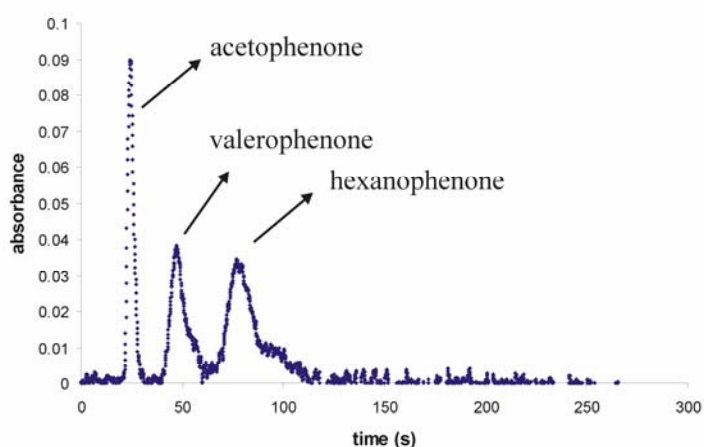
Figure 11. Separation of acetophenone (not retained), valerophenone and hexanophenone in a clogged channel with a C8 coating. The mobile phase is 30/70 (v/v) acetonitrile/tetraborate buffer (pH 9.2) and the respective concentrations are 100, 200 and 300 μg/ml.

It is expected that the geometry plays an important role in this phenomenon. When the surface to volume ratio increases (i.e. when the porosity decreases), the proportion of adsorbed water on the surface is higher. Moreover, the cavern between the top of the pillar (see fig 4b) and the top substrate can hold the water more strongly. The same holds for the side of the channel, see fig 5. In a subsequent coating experiment, care was taken to avoid water in the channel. Longer flushing times were applied (24 h methanol flushing and 24 h toluene flushing), care was taken that the toluene that was used was specified as dry by the supplier (Sigma-Aldrich,

Belgium). Apart from that, the concentration of C8 in toluene was reduced to 5% and the coating step was applied for 24 h. Performing a separation experiment in this channel with a mixture of 3 components yielded a baseline separation in 14 s within 2 mm downstream the injection zone. The peaks remained intact until the end of the channel. It is however visible that the peaks are slightly slanted, probably due to a non homogenous coating. More research needs to be done to tackle this problem.
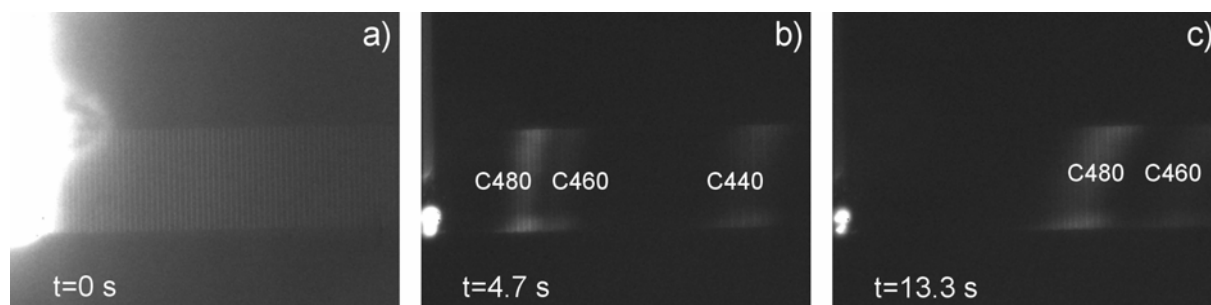
Fig. 12. A separation of C440, C460, C480 in 60/40 (v/v) water/methanol at pH 7 in a phosphate buffer, monitored with a CCD camera. The plate heights measured 2 mm downstream the injection slit are 4.8 μm, 7.9 μm and 10.3 μm, the mobile phase velocity is 0.3 mm/s.

5.5 Conclusions

A pillar array channel combining pillar support structures with an integrated waveguide was fabricated. A van Deemter curve was established for thiourea in methanol in absorbance mode, yielding a minimal plate height of 15 μm. Analysing dispersion in different zones of the channel in fluorescence mode with a CCD camera using a coumarin in methanol, the unexpectedly large dispersion appears to have a double cause, originating from the strong taper of the pillars as well as from sidewall effects. Clogging appeared to be an important issue during coating, longer flushing times seem to be beneficial but more research has to be done in this area. Nevertheless, 3 components separations in less than 15 s and within the first 2 mm of the channel were demonstrated.

Symbols

H   height of a theoretical plate (m)
σ_x spatial standard deviation (m)
M_k k^{th} order time-based moment (s^k)
C(t)   concentration at the monitor or detection plane at time t (mol/m^3)

Abbreviations

DRIE   deep reactive ion etching
PECVD   plasma enhanced chemical vapour deposition
LPCVD   low pressure chemical vapour deposition

References

1.   J.C. Giddings, Dynamics of Chromatography, Part I, Marcel Dekker, New York, 1965.
2.   De Malsche, W.; Eghbali, H.; Clicq, D.; Vangelooven, J.; Gardeniers, H.; Desmet, G. *Anal. Chem.* **2007**, *79*, 5915-5926.
3.   Effenhauser, C. S.; Manz, A.; Widmer, H. M. *Anal. Chem.* **1993**, *65*, 2637-2642.
4.   Jacobson, S. C.; Hergenröder, R.; Koutny, L. B.; Ramsey, J. M. *Anal. Chem.* **1994**, *66*, 1114-1118.
5.   Harrison, D. J.; Manz, A.; Fan, Z.; Lüdi, H.; Widmer, H. M. *Anal. Chem.* **1992**, *64*, 1926-1932.
6.   Harrison, D. J.; Fluri, K.; Seiler, K.; Fan, Z.; Effenhauser, C. S.; Manz, A. *Science* **1993**, *261*, 895-897.
7.   Mogensen, K. B.; Petersen, N. J.; Hübner, J.; Kutter, J. P. *Electrophoresis* **2001**, *22*, 3930-3938.
8.   Petersen, N. J.; Mogensen, K. B.; Kutter, J. P. *Electrophoresis* **2002**, *23*, 3528-3536.
9.   Wang, T.; J.H. Aiken, Huie, C.W.; Hartwick; R.A., *Anal. Chem.* **1991**, *63*, 1372-1376.
10. Salimi-Moosavi, H.; Jiang, Y.; Lester, L.; McKinnon, G.; Harrison, D. J. *Electrophoresis* **2000**, *21*, 1291-1299.
11. Verpoorte, E.; Manz, A.; Lu¨di, H.; Bruno, A. E.; Maystre, F.; Krattiger, B.; Widmer, H. M.; van der Schoot, B. H.; de Rooij, N. F. *Sens. Actuators, B* **1992**, *6*, 66-70.
12. Mainka, A.; Bächmann, K.J., *J. Chromatogr. A* **1997**, *767*, 241-247.
13. Liang, Z.; Chiem, N.; Ocvirk, G.; Tang, T.; Fluri, K.; Harrison, D. J. *Anal. Chem.* **1996**, *68*, 1040-1046.
14. Ro, K.K.; Lim, K.; Shim, B.C., Hahn; J. H., *Anal. Chem.* **2005**, *77*, 5160-5166.
15. J.C. Giddings, Unified Separation Science, John Wiley & Sons, New York, 1991.
16. Vervoort, N; Billen, J.; Gzil, P.; Baron, G.V.; Desmet, G; *Anal. Chem.* **2004**, *76*, 4501-4507.
17. Gzil, P.; Vervoort, N.; Baron, G.V.; Desmet, G., *Anal. Chem.* **2004**, *76*, 6707-6718.

Chapter 6: Integration of porous layers in ordered pillar arrays for liquid chromatography

This chapter has been published as:

Integration of Porous Layers in Ordered Pillars for Liquid Chromatography, De Malsche, W., Clicq, D., Verdoold, V., Gzil, P., Desmet, G. and Gardeniers, H. , Lab Chip 2007, 7, 1705-1711.

6.1 Abstract

The present paper describes a method for the production of partly porous micro-pillars in columns suitable for use in liquid chromatography. These layers increase the available surface at least two orders of magnitude without destroying the huge benefits of the ordered nature of the system. A process flow was developed that enabled to create a 550 nm thick porous layer on the pillar array in a sealed channel configuration, withstanding pressures up to at least 70 bar. Measuring band broadening under non-retained conditions, only a modest increase in plate height was observed in the porous pillar array as compared to that in a non-porous pillar array. The homogeneity of the layers was demonstrated using optical microscope and SEM pictures and by monitoring peak velocities at constant pressures. The internal porosity was determined using particles with a diameter larger than the mesopores in combination with a dye that could penetrate in the pores.

6.2 Introduction

Nearly a decade has now passed since the publication of the groundbreaking paper of the group of Regnier[1], wherein they proposed to use the micro-fabrication techniques of the microelectronics industry to produce chromatographic beds consisting of perfectly ordered arrays of micro-pillars instead of a random pack of spherical beads.

Despite the beauty and the simplicity of the concept, and despite the many attractive advantages (perfect column-to-column reproducibility, a drastic reduction or even a complete elimination of the eddy-diffusion, large freedom in pillar shape and packing density),[1-5] the field of LC is still awaiting the great breakthrough of this technology.

A number of encouraging results have been obtained under CEC conditions. He et al.[6] reported reversed-phase separations of FITC-tagged peptides in microfabricated columns in the capillary electro-chromatography (CEC) mode. In addition, Slentz et al.[7]

investigated several COMOSS (collocated monolithic support structures) columns with varying dimensions. Working in the CEC-mode as well, they were able to obtain an efficiency of 620,000 plates per meter using 10 μm deep channels filled with micromachined "particles" of 5.2 × 5.2 μm (diamond shape).

The conduction of pressure-driven LC separations however appears to be more tedious. This is certainly due to the fact that pressure-driven flows are more sensitive to slight imperfections (sealing defects, presence of dust particles, etching inaccuracies,..) than electrically-driven flows. Recently however, using channels fabricated using a state-of-the-art high aspect ratio etching Bosch[®] process, our group succeeded in performing reversed-phase LC separations with efficiencies that are, at least for weakly retained compounds, in agreement with the theoretical expectations and were significantly better than a packed bed of spheres filled with similarly sized particles.[8-9]

The separations presented in [8-9] obviously still can be further optimized, for example regarding the suppression of the side-wall effect.[9-11] The present study however addresses one of the other fundamental drawbacks of all thus far fabricated micro-pillar array columns, be it the silicon pillars used in [9] or the PDMS channels used in.[7] Being filled with pillars that are non-porous, only the outer surface is available for chromatographic exchange. As a consequence, the phase ratio in these columns is orders of magnitude smaller than in the packed bed HPLC columns filled with porous silica beads that are currently used with great satisfaction in any analytical chemistry lab.[12] The availability of a large exchange surface is an absolute prerequisite for the analysis of samples containing components that are present in a broad range of concentrations, so that the adsorption isotherms of the column can remain linear over a broad range of concentrations. To ever become competitive with the current generation of packed-bed HPLC columns, it is hence obvious that ways need to be found to improve the phase ratio of micro-pillar array columns. The production of porous pillars, besides the application of a homogenous stationary phase on pillar arrays, is currently recognized as the major hurdle towards the holy grail of liquid chromatography.[13]

Different ways of obtaining microstructured chromatographic columns with larger exchange areas have already been described in the past. A very straightforward way consists of first depositing a meso-porous material in a channel using one of the well

known sol-gel techniques.[14-15] However, during the subsequent patterning of these layers using reactive ion etching, the dimensions of the patterned features change during etching and also considerable tapering occurs.[16-17] This happens because the etching gasses diffuse into the meso-pores. Since the top of the pillars is inevitably longer subjected to the etching plasma, pillars with a smaller top than bottom cross-section are obtained, making the technique not suitable for generating the submicron-gapped pillars that are required for the most demanding chromatography applications. An appealing approach is the formation of porous glass by plasma etching of silicon, offering great perspectives for electrically driven flows.[18] Unfortunately, these chips cannot withstand the high pressures required to perform HPLC-separations.[19] Another method is the anodisation of highly doped silicon in HF studied, among others,[20-24] by Tjerkstra[25] and used by Clicq et al.[26] to perform shear-driven chromatography in nano-channels. Silicon chips have also already been anodised for a variety of other applications, such as matrix materials in DIOS-MALDI,[27] and also as a support for proteins in microreactors.[28-29] Never however, have these porous materials been fabricated in the configuration of a closed channel, through which a pressure-driven flow could be generated. In the work presented here, a process scheme has been developed to produce an array of porous silicon pillars that is integrated in a sealed channel that can at least withstand pressures of 70 bar. The latter poses a significant challenge because porous layers are rough and fragile and cannot be easily bonded with another substrate. The present paper describes the results of the probably first attempt ever to tackle the problem of the unsuficiently available surface area via electrochemical anodisation of silicon pillars used for liquid chromatography.

6.3 Experimental

6.3.1 Chip design and microfabrication procedure

The channels were filled with an array of pillars of 10 μm arranged on an equilateral triangular grid with sides selected such that the array had an external porosity of 40 %. The channels were preceded by a localized injection system, identical to the one already described in [30,8-10] and allowing to perform nanoliter sized injection volumes.[9] The microfabrication started with the deposition of a 300 nm thick LPCVD silicon nitride on a 100 mm diameter and 475 m thick (100) silicon wafer with a resistivity of 0.010-0.025 ohm cm (see Fig 1 for details of process flow). Next, the pillars were defined in the SiN

layer by reactive ion etching (RIE). Subsequently, supply channels are etched 40 μm deep with Bosch-type deep reactive ion etching. Subsequently both the supply channels and the pillar-channel were etched to a depth of 19 μm Next, a layer of 750 nm aluminium is sputtered on the backside of the wafer and annealing at 400 °C in water vapour is performed, assuring a homogenous electrical backside contact during the anodisation step.[31] During this anodisation step, the process wafer is screwed in a nylon holder and sealed by an O-ring, with a 5 cm × 5 cm wafer covered with 500 nm gold (functioning as a counter electrode) on top of it at a fixed distance of 3 mm. The system is then immersed in 5 % HF and nitrogen is blown constantly between the process wafer and the counter electrode to avoid the formation of large bubbles that can lead to non-porous regions. A copper plate attached to the backside of the process wafer functions as the working electrode, whereas a silver chloride electrode is used as reference electrode. A potentiostat was used to provide a constant voltage of 0.2 V during 200 s. Further, access holes were powder blasted from the backside and the wafer is anodically bonded with a 500 μm thick Pyrex® wafer.

6.3.2 Injection system and injection procedure

The injection is performed by means of an automated valve system, controlled with an in-house written C++ program, as already described in.[9] During the actual sample injection step, the automated valve system ensures that the inlet and the outlet of the mobile phase circuit are closed. During the subsequent sample separation, the inlet and the outlet of the sample injection circuit are diverted to a high flow resistance capillary, allowing for the existence of a small leakage flow and thus avoiding tailing. The flow driving force originates from two separate nitrogen pressurized vessels controlled by mass flow controllers (Bronkhorst), allowing to perform the injection and propagation step at different pressures at a controlled fashion without suffering from control delay problems. Interfacing the chip with the supply tubings occurs with commercially available Upchurch nanoport® connectors, that are screwed in a house-made PMMA holder.

6.3.3 Chemicals

For the determination of the band broadening, coumarin C480 (Cas no. 41267-76-9, Across Organics, Belgium) was dissolved in HPLC-grade methanol at a final

concentration of 1×10^{-3} M, after which it was filtered. For the mobile phase HPLC-grade methanol was used. As external void volume markers (excluded from the mesopores of the porous silicon), yellow green fluorescent carboxylate-modified nanoparticles of 40 nm diameter (Fluosphere F8795, Molecular Probes, 5 % solids) dissolved in a sodium tetraborate buffer (3 mM, pH 9.2) with addition of 0.5 g/l Triton X-100) were used, whereas pure FITC (0.1 mM) was used to determine the total volume (mesopores + external flow-through pores).

6.3.4 Detection and plug analysis

After the injection, a motor controlled translation stage was used to follow the injected tracer plugs at constant velocity, hence keeping the plug stationary in the microscope image and yielding the highest possible band broadening measurement accuracy. This type of experiment is also perfectly suited to investigate the stability of the applied flow velocity. A standard Hg-vapor lamp (HBO103/W2, Zeiss, Belgium) of the microscope could be used to excite the fluorescent dyes in the UV. A UV-1 filter cube set (U V-2A DM400 Nikon, Cetec N.V.) was used when working with the coumarin and a blue filter cube set (F11001, AF Analysentechnik) was used when working with the nanoparticles and the fluorescein.

The peaks were visualized using an air-cooled CCD fluorescence camera (ORCA-ERC4742, Hamamatsu Photonics, Belgium) mounted on the video adapter of the microscope.The microscope was mounted on a breadboard (M-IG 23-2, Newport, The Netherlands), together with a linear displacement stage (M-TS100DC.5, Newport) and a speed controller (MM, 4006 Newport). The peak intensity profiles were subsequently analyzed using the accompanying Simple PCI® image analysis software. For the determination of the peak widths, the peak fluorescence intensity is vertically averaged across a central zone of 150 μm (see Fig. 4) and fitted with a Gaussian function in Sigmaplot®.

6.4 Results

6.4.1 Quality of porous layers

Figure 1 depicts the developed process flow. An important point here is the deposition of a SiN layer on top of the Si used as a mask layer for the anodisation. This inhibits the

formation of a porous layer on the top surface of the pillars and the rest of the wafer. Because of its roughness, this porous layer would make the surface fragile and non-bondable. The SiN-layer is present on top of the pillars (see Fig. 2), but even though this layer was also used as the etching mask for the deep reactive ion etching of the pillars and was thereby significantly roughened, it was still flat enough for the anodic bonding step that was used to seal the channel. The bonding strength was tested up to pressures of 70 bar (certified upper limit of the employed Nanoport® connectors) using a standard HPLC pump. No leakages were observed.
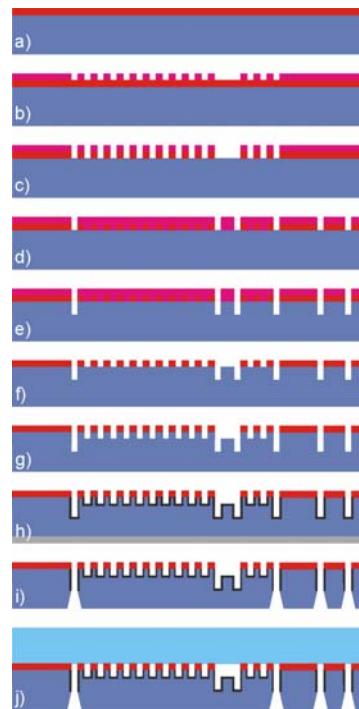
**Fig. 1** Process flow of the chip fabrication (not to scale). **(a)** 300 nm LPCVD SiN is deposited on a Si wafer, **(b)** lithography defines the pillars, **(c)** pillars are defined in the SiN by RIE etching, **(d)** the resist is stripped and a second lithography step to define the supply channels is executed, **(e)** these access channels are then RIE etched in the SiN and subsequently 50 μm Bosch etched in the silicon, **(f)** the resist is stripped, **(g)** both the supply channels and the pillar array are etched 10 μm in the silicon, **(h)** a layer of 750 nm of aluminum is deposited on the backside of the wafer, the wafer is screwed in a holder and the anodisation occurs at the top side of the wafer, **(i)** the aluminum layer is etched, a bottom side lithography defines the through-holes to interface the channels, the top side is covered with a foil to avoid particle contamination in the array and then the wafer is powderblasted, **(j)** the wafer is thoroughly cleaned with nitric acid and rinsed in deionized water and then anodically bonded on a glass wafer.

Making a series of high resolution SEM's and optical microscope pictures (Fig. 2), the produced porous layers appeared to be highly homogenous on the wafer scale, whereas on the pillar scale the surface profile varies considerably.
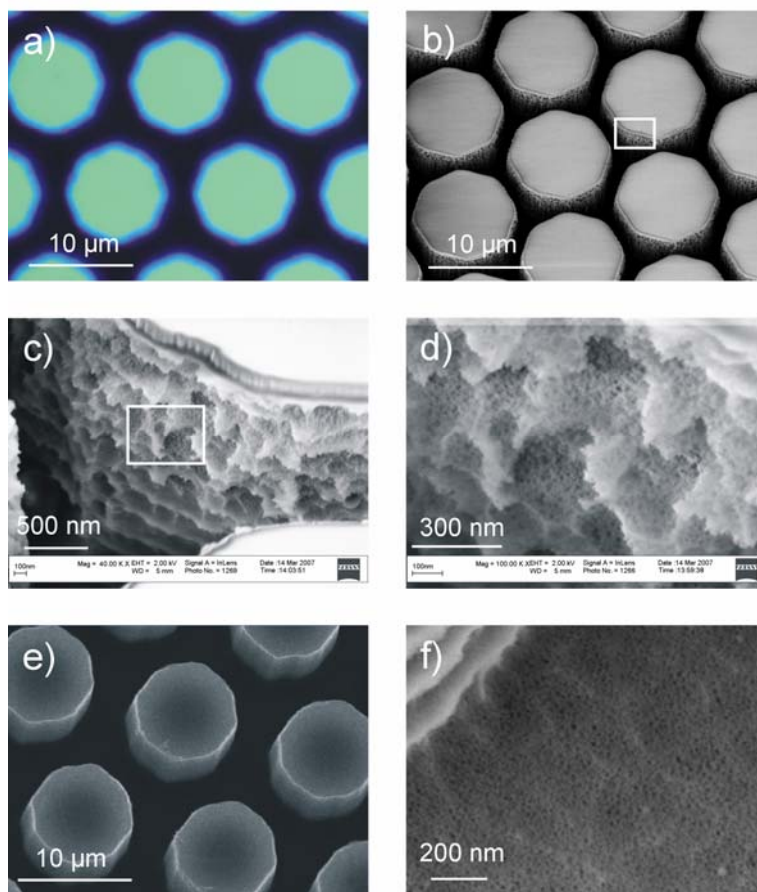
Fig.2 Caption.(a) Optical microscope picture of partly porous pillars before bonding. The core is non-porous, the outer rings are porous Si. The color difference at the side is due to the scalloping of the Bosch-etch cycles. (b-d) Scanning electron microscope (SEM) pictures of the porous layer with increasing magnification. (b) 5.000 X magnification , (c) 40.000 X magnification zoom-in of the white box in (b), (d) 100.000 X magnification of the box in (c) (e) SEM picture of the 10 µm pillars with the porous layer removed by HF etching. (f) SEM picture of the porous layer on the bottom of the channel.

The meso-pore size ranged between 5 and 15 nm. In the initial stages of the study, different thicknesses of porous layers were grown. Cleaving wafers with different anodisation times and determining the porous layer thicknesses with the SEM on the one hand, and comparing this with different distinguishable zones with the optical microscope on the other hand, demonstrated that both measurement tools give identical values. Looking at these cleaved pillars from the side, no difference in porous zone thickness was observed between the top and the bottom level of the pillar. Given the variation of the E-field density across the height of the pillar[32-33] (Fig. 3), a difference of layer thicknesses can be expected. This becomes visible and more pronounced when growing thicker layers in microreactors.[34-37] Apart from that, the porous bottom layer has been shown by these authors to become thicker and thicker in a non-lineair fashion as compared to the reactor wall. In our case, this regime was not attained, as in all our cross-sectional views of broken wafers the porous layer on the bottom had the same thickness as the pillar porous

layer. Figure 2 depicts the pillar configuration that was used in this study. In the finally tested pillar arrays, the porous layer thickness was of the order of 550 nm. This value was used as a compromise between a sufficiently high retention capability on the one hand and a limited additional band broadening due to the slow diffusion of analytes in this zone as compared to the fast diffusion outside the pillar on the other hand.

Another reason to only anodize the outer pillar layer is that completely anodized pillars were much more fragile and displayed a high tendency to break during handling.

To be able to accurately measure such a small thickness, SEM measurements were needed. Because the duration of used HF-solution during the anodisation experiment had an influence on the anodisation rate, it was preferred to determine the porous zone thickness after performing the flow experiments, given the destructive nature of the characterization with the SEM. This was easily done by immersing the chip in 50 % HF,
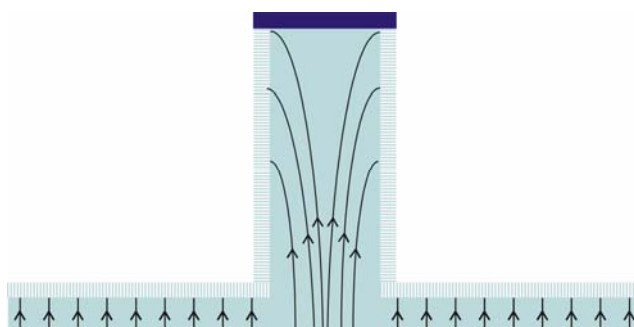
Fig. 3 Schematical representation of the electric field lines in a silicon pillar.

etching away both the top lid of Pyrex and also the porous layer. The difference in pillar diameter before and after this etching step was then a measure for the zone thickness.

6.4.2 Band broadening characteristics

In order to characterize the system in terms of chromatographic performance, sharply delimited coumarin plugs were injected and continuously monitored along their movement through the channel by translating the microscope objective table at the same velocity as the coumarin plug, hence allowing to keep the broadening tracer band continuously in the field of view of the microscope. Fig. 4 shows an example of such an experiment.

As can be seen, the tracer band indeed remains at the same position in the image. Given that the microscope table was translated at a constant velocity, this means that also the tracer plug moved at a constant velocity.

The velocity U_R of the tracer band is partly determined by the volume of the porous layer,

and can be expressed according to:

$$U_R = U_i \frac{V_{ext}}{V_{ext} + V_{pores}}$$ (1)

wherein U_i is the mean fluid velocity in the space between the pillars (interstitial velocity), V_{ext} the volume of the flow-through pore region outside the pillars, and V_{pores} the internal volume of the porous layer. This layer covers both the pillars and the bottom wall. Considering that the pillars are positioned on the grid points of an equilateral triangular grid, the external volume of the unit cell can be calculated as:

$$V_{ext} = (D/2)^2 \cot g(30°)\varepsilon h$$ (2)

with D the distance between the centre of the pillars (12.3 µm), h the height of the pillars (19 µm), ε the external porosity (0.4). Accounting for the fact that the porous layer (thickness δ) covers both the pillars and the bottom layer, the total volume of the mesopores in the layer can be calculated as:

$$V_{pores} = \frac{1}{2}\pi(R_p^2 - (R_p - \delta^2)).h.\varepsilon_{int} + \delta(D/2)^2 \cot g(30°)\varepsilon\varepsilon_{int}$$ (3)

with ε_{int} the internal porosity, R_p the radius of the whole pillar (5 µm) and δ the thickness of the porous layer. Eqs. (1-3) show that the velocity of the tracer band can only remain constant if the different volumetric fractions of the channel remain constant. As these are determined by the total pillar diameter, the porous layer thickness and the internal porosity of the layer, the highly constant migration speed of the tracer band hence allows to conclude that these different volumetric fractions remain constant on the entire wafer scale. To quantify the band broadening, only the central part of the channel is taken into account, because the side-wall effect[11] is known to strongly deform the bands on the trans-channel scale. As has been described in greater detail elsewhere[11], this side-wall effect originates from the fact that the pillar row immediately adjacent to the channel wall has a different local flow resistance. This induces a difference in fluid velocity which in turn deforms the tracer bands in a region that progressively becomes wider and wider. As a consequence, the bands become gradually more and more warped, as can also be witnessed from Figs. 4.b-d.
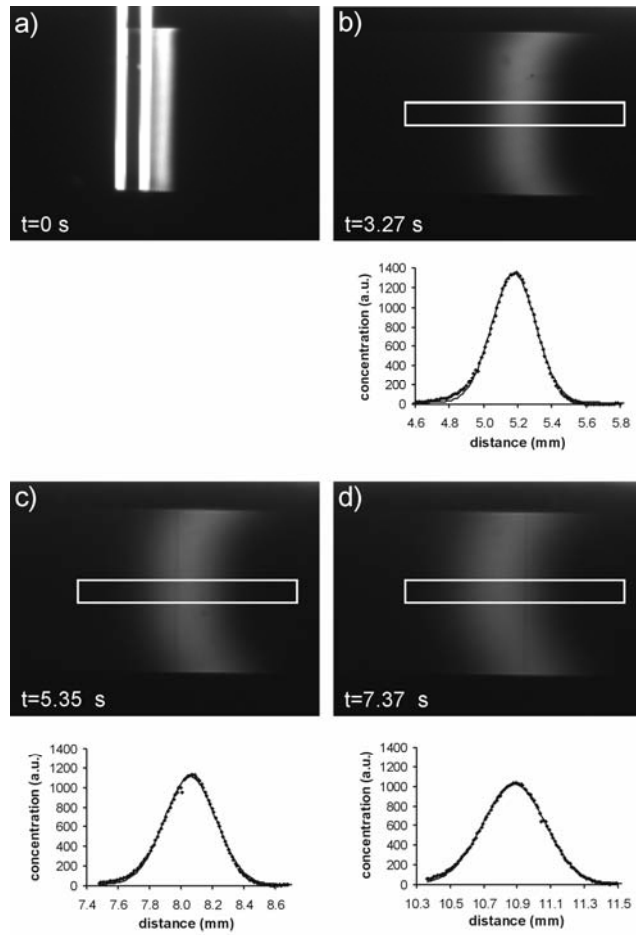
Fig. 4 Analysis procedure of the peaks. (a) A plug is injected and propagates in the channel at t=0 at a constant velocity of 1.4 mm.s^{-1} in the porous 10 μm pillar channel, (b) at t=3.27 a value of 129.62 μm is found for σ by fitting the curve with a Gaussian, (c) at t=5.35 s, σ=163.29, (d) at t=7.37 s, σ=186.57.

Fortunately, the currently employed channels are sufficiently wide to leave the central part of the band unaffected (cf. the white rectangular box added to Fig. 4 and used to read out the peak profile). Since we are essentially interested in the influence of the porous layer on the band broadening, and knowing that the side-wall effect can possibly be prevented by making much wider channels, it was decided to focus only on the band broadening in the central 100 μm of this unaffected region of the bands. Another reason to leave out the side-wall effect from the measurements is that it leads to plate heights that vary with the distance, hence making it difficult to establish general conclusions.

The theoretical plate height used to characterize the band broadening is defined as:

$$H=(\sigma_x^2-\sigma_{x,0}^2)/\Delta x \tag{4}$$

with $\sigma_{x,0}$ the inititial and σ_x the final spatial standard deviation of the gauss fit of the plug after traveling a distance Δx.

In the field of chromatography, it is often preferred to switch to dimensionless variables, wherein the plate height and the liquid velocities are made dimensionless using the pillar diameter and the molecular diffusivity:

$$v = u d_p / D_m \qquad (5)$$

$$h = H / d_p \qquad (6)$$

with d_p the pillar diameter and D_m the molecular diffusion constant. In Fig. 5, the band broadening is represented as a function of the reduced velocity for both porous and non-porous pillars (a value of $D_m = 8.6 \times 10^{-10}\,m^2/s$ is taken from ref. 38).
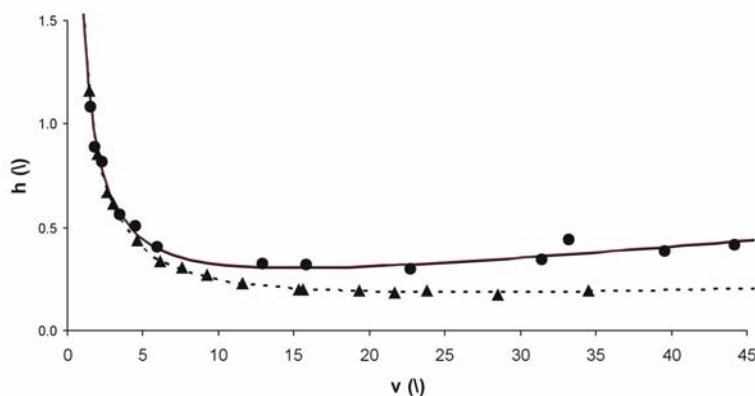
Fig.5 Van Deemter plots of the pillar array with (•) and without (▲) a porous shell and the respective fits (———) and (‐ ‐ ‐ ‐). The used dye is C480 in MeOH (1mM).

It is clear that the presence of the 550 nm porous layer has a significant effect on the plate height. At the minimum of the curve (around $v=12$) the plate height in the porous layer chip increased with some 50 % (going from h=0.2 to h= 0.3) compared to the chip without porous layer, while the difference gets more pronounced at higher velocities. This is not unexpected, because the presence of the porous layer can be expected to introduce a so-called stationary phase mass transfer resistance (C_s-term), leading to an additional plate height contribution (to be added to the plate heights obtained in the non-porous system) of the following nature: [39]

$$H_{layer} = C_s . u . \delta^2 / D_s \qquad (7)$$

wherein C_s is a dimensionless constant, δ the porous layer thickness and D_s the molecular diffusivity inside the pores of the layer. Given that this additional plate height term

increases linearly with the mobile phase velocity, it is indeed obvious to find that the difference between the porous and the non-porous case increases with the velocity. The addition of this term also explains the leftward shift of the curve minimum caused by the presence of the porous layer.

In the presented design here, the bottom of the channel is porous, wheras the top is non-porous. It is expected that this asymetry causes an additional band broadening. It seems hence worthwile to develop modified microfabrication strategies. This will be an important focus of future work.

6.4.3 Internal porosity of the porous layer

One of the difficulties of determining the internal porosity of the porous layer with the conventional adsorption methods such as the widely used BET-isotherm is the lack of a sufficient amount of test material on the chip scale. For this reason, an alternative approach has been developed. This approach was based on Eqs. (1-3) measuring difference between the migration velocity of a band of FITC dye that was able to diffuse in the porous layer on the one hand, and that of an injected band of nano-particles that were excluded from the meso-pores on the other hand. These two components can respectively be considered as being able to fully penetrate the porous layer and being totally excluded from the layer, with respective velocities U_R and U_0. The use of the size of the particles should be carefully chosen in order not to draw any false conclusions. The diameter should be larger than the pores, but small enough not to present a different velocity compared with the dye because it can not approach the pillar as close and hence follows the higher velocity streamlines. With the known layer thickness and the other geometrical parameters, the ratio of the two measured velocities U_R and U_0 can then be used to determine the internal porosity of ε_{int} as the single unknown in Eq. (3). The relation between both velocities and the corresponding volumetric fractions that are accessible to the two different markers is given by Eq. (1).

Repeating the experiment five times, the ratio between the velocities of FITC dye and the nanoparticles was found to be equal to $U_i/U_R=1.25 \pm 0.03$. Using this ratio in the left hand side of Eq. (1), the combination of Eqs. (1-3) allows to calculate that the internal porosity ε_{int} of the porous layer is equal to 0.73. This is a very high value, but such high values are not unusual for porous silicon.[40] With the measured intra-layer porosity of $\varepsilon_{int}=0.73$, and assuming a layer thickness of d= 550 nm, it can be calculated using:

$$V_{pores} = \pi[R_p{}^2 - (R_p - \delta)^2]h\varepsilon_{int} \tag{8}$$

that the volume of pores in the porous layer is for each pillar equal to 3.018×10^{-16} m^3. Subsequently assuming a cylindrical pore shape for which the specific surface is given by:

$$\frac{S_{exch}}{V_{pores}} = \frac{4}{d_{por}} \tag{9}$$

and assuming a mean pore diameter of 10 nm (estimated from SEM-pictures), it can be estimated that the presently applied porous silicon layer offered an exchange surface per pillar of 1.2072×10^{-7} m^2.

Comparing this surface with the external pillar surface, it can hence be concluded that the porous silicon method yielded approximately a 200-fold increase of the exchange surface.

6.5 Conclusions

In this work, a new method for producing porous layer coated pillar arrays in a closed channel configuration is presented. The device was able to withstand pressures up to at least 70 bar, without leakage or loss in performance when injecting plugs and measuring plate heights. Increments on the plate heights were small, whereas the increase of available surface was in the order of approximately 200 times. Future work should aim at coating procedures of these porous pillars. Layers of the order of some 500 nm were found to give a compromise between mechanical stability, band broadening and increased chromatographic exchange surface. The thickness of the layers was very uniform on the whole-wafer scale, as could be seen from the fact that the migrating species displayed a constant velocity across the entire channel length of 5 cm.

Symbols

U_R velocity of a component that can enter the porous zone (m/s)
U_i interstitial velocity (m/s)
V_{ext} volume flow-through pore region (m^3)
V_{pores} internal volume of the porous layer (m^3)
D domain size (m)
h pillar height (m)

ε	external porosity (/)
ε_{int}	internal porosity (/)
R_p	pillar radius (m)
δ	porous layer thickness (m)
H	height of a theoretical plate (m)
σ_x	spatial peak standard deviation at position x (m)
$\sigma_{x,0}$	initial spatial peak standard deviation (m)
h	reduced plate height (/)
ν	reduced mobile phase velocity (/)
C_s	stationary phase mass transfer resistance constant (/)
d_p	pillar diameter (m)
D_m	molecular diffusion coefficient (m^2/s)
D_s	molecular diffusivity inside the pores of the porous layer (m^2/s)
u	mobile phase velocity (m/s)
H_{layer}	plate height contribution of the porous layer (m)
C_s	component concentration in the stationary phase (mol/m^3)
S_{exch}	exchange surface inside the pores (m^2)
V_{pores}	internal volume of the pores (m^3)
d_{pores}	pore diameter (m)

Abbreviations

LC	liquid chromatography
CEC	capillary electro-chromatography
COMOSS	collocated monolithic support structure
DIOS	desorption-ionization on silicon
MALDI	matrix-assisted laser desorption and ionization
LPCVD	low pressure chemical vapour deposition
SEM	scanning electron microscope

References

1. He, B.; Tait, N.; Regnier, F.E. *Anal. Chem.* **1998**, *70*, 3790-3797.
2. Knox, J.H. *J. Chromatogr. A* **2002**, *960*, 7-18.
3. De Smet, J.; Gzil, P.; Vervoort, N.; Verelst, H.; Baron, G.V. Desmet, G. *Anal. Chem.* **2004**, *76*, 3716-3726.
4. Gzil, P.; Vervoort, N.; Baron G.V.; Desmet, G. *Anal. Chem.* **2004**, *76*, 6707-6718.
5. Peterson, D.S. *Lab Chip* **2005**, *5*, 132–139.
6. He, B.; Ji, J.; Regnier, F. *J. Chromatogr. A.* **1999**, *853*, 257-262.
7. Slentz, B.E.; Penner, N.A.; Lugowska E.; Regnier, F. *Electrophoresis* **2001**, *22*, 3736-3743.
8. Eghbali, H.; De Malsche, W.; Clicq, D.; Gardeniers H.; Desmet, G. *LCGC-Europe* **2007**, *20*, 208-222.
9. De Malsche, W.; Eghbali, H.; Clicq, D.; Vangelooven, J.; Gardeniers, H.; Desmet, G. *Anal. Chem.* **2007**, *79*, 5915-5926.

10. De Pra, M.; Kok, W.T.; Gardeniers, J.G.E.; Desmet, G.; Eeltink, S.; van Nieuwekasteele, J.W Schoenmakers, .P.J. *Anal.Chem.* **2006**, *78*, 6519-6525.

11. Vervoort, N.; Billen, J.; Gzil, P.; Baron, G.V.; Desmet, G. *Anal. Chem.* **2004**, *76*, 4501-4507.

12. Unger, K.K.; Kumar, D.; Grun, M.; Buchel, G.; Ludtke, S.; Adam, T.; Schumacher, K.; Renker, S. *J. Chromatogr. A* **2000**, *892*, 47-55.

13. Eijkel, J. *Lab Chip* **2007**, *7*, 815.

14. Nakanishi, K. *Journal of the Ceramic Society of Japan* **2007**, *115*, 169-175.

15. Mezza, P.; Phallippou, J.; Sempere, R. *j. non-cryst. solids* **1999**, *243*, 75-79.

16. Standaert, T.E.F.M.; Joseph, E.A.; Oehrlein, G.S.; Jain, A.; Gill, W.N.; Wayner, P.C.; Plawsky, J.L. *J. Vac. Sci. Technol. A*, 2000, **18**, 2742-2748.

17. Sankaran, A.; Kushner, M.J. *J. Appl. Phys.* **2005**, *97*, 1-10.

18. de Andrade Costa, R.C.; Mogensen, K.B. Kutter, J.P. *Lab Chip* **2005**, *5*, 1310.

19. K.B. Mogensen, personal communication

20. Zhang, X.G. *J. Electrochem. Soc.*, 2004, **151**, 69-74.

21. Kim, D.-A.; Im, S.-I.; Whang, C.M.; Cho, W.-S.; Yoo, Y.-C.; Cho, N.-H.; Kim, J.-G.; Kwon, Y.-J. *Appl.Surf. Sci.* **2004**, *230*, 125-130.

22. Bomchil, G.; Herino, R.; Barla, K. Pfister, J.C. *J. Electrochem. Soc.* **1983**, *130*, 1611-1614.

23. Arita, Y. *J. Cryst. Growth* **1978**, *45*, 383-392.

24. Lehmann, V. *Thin solid films* **1995**, *255*, 1-4.

25. Tjerkstra, R.W.; De Boer, M.; Berenschot, E.; Gardeniers, J.G.E.; van den Berg, A. Elwenspoek, M.C. *Electrochim. Act*. **1997**, *42* 3399-3406.

26. Clicq, D.; Tjerkstra, R.W.; Gardeniers, J.G.E.; van den Berg, A.; Baron; G.V.; Desmet, G. *J. of Chromatogr. A* **2004**, *1032*, 185-191.

27. Górecka-Drzazga, A.; Bargiel, S.; Walczak, R.; Dziuban, J.A.; Kraj, A.; Dylag, T.; Silberring, J. *Sensor Actuat B 2004*, *103*, 206-212**.**

28. Laurell, T.; Drott, J.; Rosengren, L.; Lindström, K. *Sensor Actuat B* **1996**, *31*, 161-166.

29. Lendl, B.; Schindler, R.; Kellner, R.; Drott, J. Laurell, T. *Anal. Chem.* **1997**, *69*, 2877-2881.

30. Blom, M.T.; Chmela, E.; Oosterbroek, R.E., van den Berg, A. *Anal. Chem.* **2003**, *75*, 6761-6768.

31. Raz, O.; Starosvetsky, D.; Tsuda, T.; Nohira, T.; Hagiwara, R.; Ein-Eli, Y. *Electrochem. Solid St.* **2007**, *10*, 25-28.

32. John Newton, Elecrochemical Systems part 1, Prentice hall, New York, 1991.

33. Zaban, A.; Meier, A. Nozik, A.J.; Gregg, B.A. *Proceedings of Electrochemical Society* **1997**, 97, 13.

34. Bengtsson, M.; Drott, J. ; Laurell, T. *phys. stat. sol.* **2000**, *182*, 533-539.

35. Bengtsson, M.; Ekström, S.; Marko-Varga, G.; Laurell, T. *Talanta* **2002**, *56*, 341-353.

36. Drott, J.; Lindstrom, K.; Rosengren, L.; Laurell, T. *J. Micromech. and Microeng.* **1997**, *7*, 14-23.

37. Ressine, A.; Ekström, S.; Marko-Varga, G.; Laurell, T. *Anal. Chem.* **2003**, *75*, 6968-6974.

38. Pappaert, K.; Biesemans, J.; Clicq, D.; Vankrunkelsven, S.;

Desmet, G. *Lab Chip* **2005**, *5*, 1104-1110.

39.   J.C. Giddings, *Dynamics of Chromatography-Part I*, 1965, Marcel Dekker, New York.

40.   Canhan, L.; Malvern, D. *Properties of Porous Si*, Inspec, London, 1997.

Chapter 7: Experimental study of porous silicon shell pillars under retentive conditions

This chapter will be published as:

Experimental Study of Porous Silicon Shell Pillars under Retentive Conditions, De Malsche, W., Gardeniers, H., Desmet, G, Anal. Chem. 2008, accepted for publication.

7.1 Abstract

Experimental measurements of the retention capacity and the band broadening in perfectly ordered porous shell pillar array columns are presented for a wide range of retention conditions and layer thickness. The porous silicon shells were obtained using electrochemical anodization of the solid silicon pillars obtained using deep reactive ion etching.

Using 10 μm wide pillars, minimal reduced plate height values of the order of h_{min}=0.4 to 0.5 were obtained under non-retained conditions, even in cases were the outer shell made up 20% of the total diameter. Under retained conditions, minimal plate heights around h_{min}=0.9 were obtained, even at retention factors up to k'=12.

Using a model based on Giddings non-equilibrium theory, and using a newly calculated value for the stationary zone configuration factor for the case of porous shell cylinders, a plate height model describing the band broadening in porous shell pillar arrays has been established. The validity of this model is demonstrated by showing that the geometrical parameters appearing in the model and fitted using band broadening measurements under non-retained conditions can be used to relatively accurately predict the band broadening under retained component conditions. Using this model, some speculations on the ultimate performance of porous pillar array columns could be made.

7.2 Introduction

After Regnier and co-workers[1-3] introduced the pillar array concept around 1998 as a groundbreaking alternative for the traditionally employed packed bed columns, relatively little progress has been made to turn the concept in practically useful and superior performing separation columns. After a few theoretical studies,[4-5] the first experimental Van Deemter

curves and chromatograms were only published in the past year.[6-11] It was found that reduced plate heights as small as h_{min}=0.2 could be obtained under non-retained conditions and with pillars of 5 and 10 μm. Under retained conditions, reduced plate heights of the order of h_{min}=1 could be obtained. In both cases, the band broadening contribution originating from the side-wall region had to be omitted because the employed etching method could not prevent a machining tolerance on the distance between the closest row of pillars and the side-wall. Several potential solutions to this problem (amongst which the use of deep-UV technology) are currently under development.

Other recent developments related to interfacing microfabricated chromatographic columns with on-chip UV-Vis detection [12-13] and to the combination of microfluidic channels and electrospray-tips for MS detection.[14-15]

An important deficiency of the pillar array columns reported on in [6-11] is that they only consisted of non-porous pillars. The lack of retention surface of these columns is hence obvious. It was only very recently that the first dispersion measurements were made in an array of partially porous pillars.[16] These pillars were obtained via electrochemical anodization,[17-18] using the silicon pillars and the silicon channel substrate as the conductive medium for the anodization current. The feasibility of the integration of porous silicon in chips has been clearly demonstrated by Tjerkstra et al.[19] The devices they fabricated included multi-walled micro- channels useful for size exclusion separations and also 1-D open-tubular nanochannels having a porous bottom wall for use in shear-driven chromatography.[20] Other important contributions to the use of porous silicon in lab-on-a-chip devices were made, amongst others, by Laurell and co-workers, using for example the porous silicon matrix as a support for proteins in microreactors.[17-18]

As schematically depicted in Figure 1, the first phase of the anodization process creates a thin layer of porous silicon on the outer surface of the pillars. As shown in,[16] the thickness of these layers was quite uniform along the height of the pillars. A major advantage of stopping the anodization process shortly after this first phase is that the formed mesopores are running perpendicular to the side-walls of the pillars, hence providing a maximal pore diffusion rate.
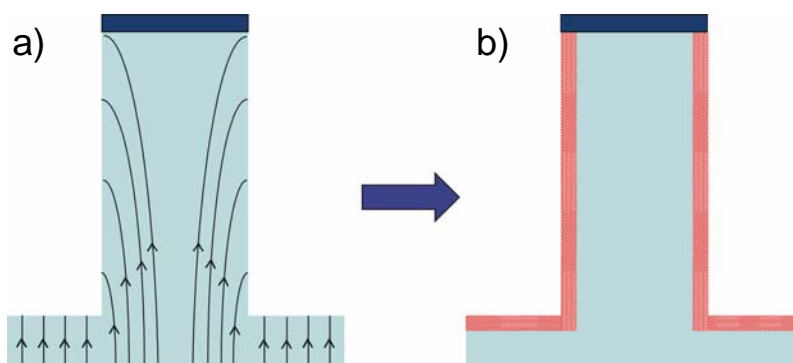
Fig. 1 (a) Schematic representation of the electric field lines during the anodization procedure at the silicon pillar surface and **(b)** a porous shell layer obtained after the electrochemical etching step.

The produced porous shell pillars can be considered as the cylindrical equivalent of the porous shell halo-sphere particles that are currently being introduced with great success in wide-bore packed columns.[21-22]

Attempts were also made to obtain fully porous pillars, but these turned out to be much too fragile. Even the application of a 1 μm thick layer on a 5 μm diameter pillar makes the pillars too fragile to survive the currently applied cleaning and handling procedure. Nearly all produced 5 μm pillar arrays therefore contained several small regions of collapsed pillars severely disturbing the eluting bands. More work is obviously needed to solve this mechanical stability problem.

The present paper relates to a study investigating the chromatographic properties of the produced porous shell layers. To avoid any influence of the damaged pillar areas observed in the 5 μm pillar arrays, the present study is limited to 10 μm pillars only. Fitting the obtained plate height data with a physically sound plate height model, the study also aimed at determining the different magnitudes of the mobile and stationary zone mass transfer, hence allowing the optimization of the thickness of the shell layers. Being widely applicable (different materials will only lead to different layer diffusion parameters), the model will also be useful to predict the optimal layer thickness of a different coating material (for example a polymeric layer).

The study also pursues a more fundamental outcome, because the high degree of uniformity, and the concomitantly low A-term dispersion, makes pillar array columns with both non-porous and thin shell-porous pillars ideally suited to make experimental investigations of how the C_m- and C_s-band broadening terms depend upon the different system variables such as the

velocity, the retention factor, the diffusion coefficient etc… With packed bed columns, the C_m and C_s-band broadening is always partly masked by the relatively strong eddy-dispersion, typically making up about one half of the plate heights around the optimum of the van Deemter curve.[4-5]

7.3 Experimental

7.3.1 Microfabrication

The channels were filled with an array of 10 μm cylindrical pillars having their centre point arranged on an equilateral triangular grid with sides selected such that the array had an external porosity of 40 %. The channels were preceded by a localized injection system, identical to the one already described in [23-24, 9] and allowing to perform nanoliter sized injection volumes. The microfabrication has already been described elsewhere.[16] In short, a highly doped p-type (100) Si wafer of 475 μm thickness and 10 cm diameter was patterned to define the pillars (19 μm deep) and the supply channels (60 μm deep) for injection and mobile phase flow. The substrate was then screwed into a holder and immersed in 5 % HF, while applying a constant current of 20 mA across the wafer for 5 and 6.5 min to respectively obtain a 1 μm and a 1.4 μm porous layer thickness. Finally, the silicon wafers were powderblasted to generate the connection holes and the channels were sealed by anodic bonding them to a 500 μm thick Pyrex[®] substrate.

7.3.2 Injection and detection

The sample injection was performed using an automated valve system, controlled with an in-house written C++ program, as already described in.[9] During the actual sample injection step, the automated valve system ensures that the inlet and the outlet of the mobile phase circuit were closed. During the subsequent sample separation, the inlet and the outlet of the sample injection circuit were diverted to a high flow resistance capillary, allowing for the existence of a small leakage flow and thus avoiding tailing.

To follow the injected plugs during their passage through the pillar array, a motor controlled translation stage was used to keep the plug stationary underneath the lens of a fluorescence microscope image. In this way, the highest possible band broadening measurement accuracy can be obtained. This type of experiment is also perfectly suited to investigate the stability of the applied flow velocity. A Hg-vapour lamp was used to excite the fluorescent dyes in the

UV. The peaks were visualized using an air-cooled CCD fluorescence camera. The peak intensity profiles were subsequently analyzed using the accompanying Simple PCI® image analysis software. For the determination of the peak widths, the peak fluorescence intensity is vertically averaged across a central zone of 150 μm. For more details on the applied procedures and the used hardware the reader is referred to De Malsche et al.[9]

Given the good symmetry of the peaks, all plate height values were obtained by fitting the obtained concentration profiles with a Gaussian function using Sigmaplot®. The concentration profiles and the accompanying moments were calculated in the space domain, because the bands remain stationary with respect to the microscope lens. The best fitted variance values were used to calculate the plate height according to the following expression:

$$H = \frac{\sigma_{x,e}^2 - \sigma_{x,0}^2}{\Delta x} \tag{1}$$

wherein $\sigma_{x,e}$ and $\sigma_{x,0}$ are the variance of the injected band at the end and the initial position and wherein Δx is the distance between both positions (0.5 cm). Retention factors were calculated by comparing the measured mean velocity of the bands with that of a non-retained band.

7.3.3 Chemicals and coating procedure

For the establishment of the van Deemter curves and for the study of the retention behaviour as a function of the methanol concentration, coumarin C480 (Cas no. 41267-76-9, Across Organics, Belgium) was dissolved in HPLC-grade methanol at a final concentration of 1×10^{-3} M, after which it was filtered. For the mobile phase, HPLC-grade methanol and a phosphate buffer (0.1 mM at pH3) were used. For the separation also C440 (CAS No. 26093-31-2), C450 (CAS no. 26078-25-1) and C460 (CAS no. 91-44-1) were used, again filtered and the mother solutions were prepared at a final concentration of 1×10^{-3} M in methanol. For the coating procedure, the channels were first flushed with methanol for 3 h and then overnight with water-free toluene. Then a solution of 5 % octyldimethylchlorosilane in toluene (Sigma-Aldrich, Belgium) was pumped through the pillar array for 24 h. Finally, the pillars were flushed with dry toluene (Sigma-Aldrich, Belgium) for 3 h and with methanol for 2 h.

7.3.4 Safety

Hydrofluoric acid and nitric acid have been used during the chip production in the clean-room. Inhalation and contact with skin and eyes has to be avoided. The pressurized vessels

and their tubing to the nitrogen bottle should be fixed conform the rules for working with pressurized gases. During depressurization, solvent vapour is released from the vessels through separate tubing. This should occur in a well ventilated environment. Given their toxicity, the coumarin dyes must be handled with care.

7.4 Results

7.4.1 Visual inspection of produced pillar arrays

Figure 2 shows an optical microscope picture (magnification 1,500) and a high-resolution scanning electron microscope (SEM) picture (magnification 579,000). The porous zone can be seen through the transparent silicon nitride layer having a thickness of 300 nm and which is resting on top of the pillar (Fig 2a). The outer shell has a different colour due to different light reflection behaviour at the porous silicon interface as compared to the massive silicon interface in the core zone.
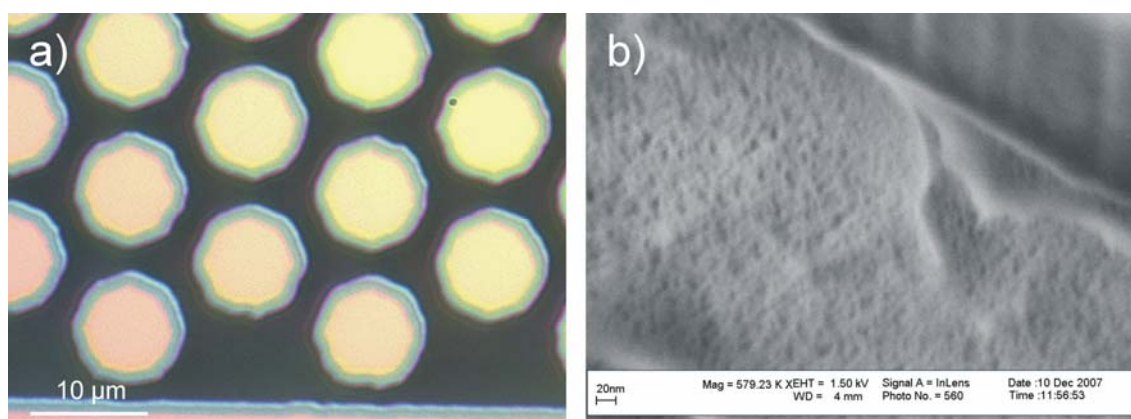
Fig. 2 (a) Optical microscope picture of a group of porous shell pillars with a shell layer of 1 μm and **(b)** high resolution scanning electron microscope picture of the top area of a porous pillar. The top part consists of (non-porous) SiN, that serves as the bonding surface for subsequent anodic bonding to a glass substrate.

The thickness of the differently coloured zone agrees perfectly with the porous zone thickness. This could be demonstrated by etching away the porous zone with hydrogen fluoride and measuring the pillar dimension with a SEM.[16] The meso-pores covering the side-wall of the pillars become distinguishable in the SEM-image (Fig 2b) and the diameters can be estimated to be of the order of 10 nm and smaller. 7.4.2 Retention properties

To assess the increase in retention surface offered by the formation of the porous silicon shells, the retention of C480 was measured for various mobile phase compositions. The results are shown in Figure 3. The black data points are for the highest retention case,

obtained after having coated the pillars for a maximal number of days, i.e., a number of days above which the retention strength no longer depended on the coating duration (i.e. 4 days for a shell thickness of δ=1.0 and δ=1.4 μm and 1 day for the non-porous pillar array). Comparing the two δ=1 μm cases (grey data points=1 day of coating, black data points=4 days of coating) shows the importance of a sufficiently long duration of the coating protocol.
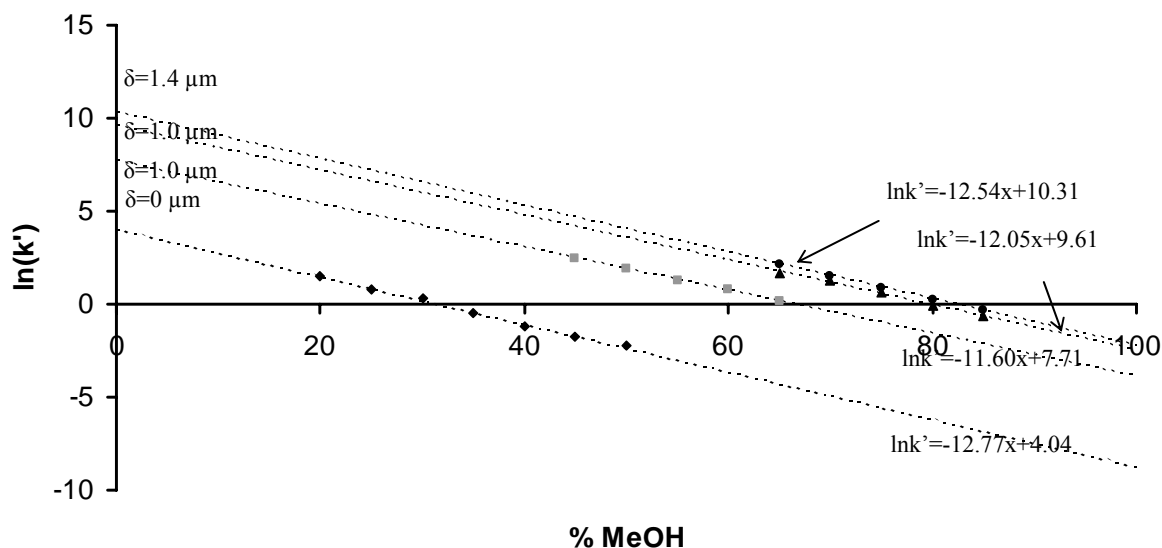
Fig. 3 Relation between the retention factors of the studied channels and the methanol content. From bottom to top, the curves respectively represent the following cases: non-porous pillars, 1 μm shell pillars (1 day coated, grey symbols), 1 μm shell pillars (4 days coated) and the 1.4 μm shell pillars (4 days coated). It was checked that the retention no longer increased after an additional day of coating procedure.

In each case, the obtained retention factors display a straight line relationship between ln k' and the fraction of organic modifier, as is typically observed for reversed-phase supports. As a consequence, the obtained retention factor data could be well fitted using:

$$\ln k' = \ln k'_0 - S\phi \qquad (2)$$

The obtained best fit expressions have been added to Figure 3. As can be noted, the slope values (=solvent strength S) all lie around S=12, for both the shell layer and the non-porous pillars (δ=0). This value is comparable, yet slightly larger than the solvent strength value of S=7-10 typically cited for reversed phase coatings and methanol as the organic modifier.[25]

Considering now the black data only, and comparing (Table 1) the extrapolated retention factors in pure water (lnk'_0), it follows that the effective retention surface increases with a factor of ~260 if going from a non-porous pillar to a pillar with layer thickness δ=1 μm and to a factor of ~525 for the layer with δ=1.4 μm. With the external surface of one pillar exactly known, these factors allow to calculate the total effective retention surface (S_eff) available in

each porous shell pillars (Table 1). The increase that is noted by going from $\delta=1$ μm to $\delta=1.4$ μm (nearly a doubling of the retention surface) does not correspond to the increased volume of the layer (which only gives a 33% increase if assuming the same internal porosity in both cases). To explain the more than proportional increase of effective exchange surface, one hence needs to assume that the internal porosity of the thicker layer is larger than that of the thinner layer (for which it was assumed that $\varepsilon_{int}=0.73$).[16] This assumption could be valid, since it is in agreement with the general observation that the internal porosity of porous silicon layers tends to increase with the anodization time.[26]

Table 1. Estimation of the pore size using the (known) surface for the non-porous pillar and the retention factors of the three considered porous layer thicknesses (pillar height is 19 μm).

	$\delta=0$ μm	$\delta=1.0$ μm	$\delta=1.4$ μm
lnk'_0	4.0	9.6	10.3
k'_0	57	15,000	30,000
S_{eff} (based on non-porous pillar)	597 μm^2	160,000 μm^2	310,000 μm^2
V (porous zone)		540 μm^3	720 μm^3
V (pores)		320 μm^3	430 μm^3
d (pore)		8.3 nm	5.5 nm

Making the (probably incorrect) assumption that the internal surface of the meso-pores has the same retention properties as the surface on the pillar mantle, and roughly estimating that the porous layers after coating have an internal porosity of $\varepsilon_{int}=0.6$, it can be calculated that the mean pore diameter after coating is about 5 to 8 nm (circular pore assumption, see Table 1). This is in qualitative agreement with the pore sizes that can be estimated from the HR-SEMs.

A moderating remark about the above calculated data for the pore volume and the pore radius is that part of the retention surface originates from the fact that the currently applied anodization method cannot prevent the formation of a porous layer on the bottom substrate as well, while the above calculations were made by attributing the entire surface to the pillars. However, HR-SEMs of the bottom layer showed that it had very wide pores, so that the total retention surface originating from the bottom layer can anyhow be assumed to be small.

7.4.3 Band broadening properties

7.4.3.1 Qualitative observations

A first series of band broadening experiments was performed using pure methanol as the mobile phase. The results (Figure 4) show a clear influence of the porous shell layer thickness. The fact that the minimal plate height and the slope of the C-term dominated part of the van Deemter-curve both increase with increasing layer thickness is in agreement with one's intuition. The same holds for the observation that the optimal reduced velocity decreases with increasing δ. Minimal reduced plate height values are of the order of $h_{min}=0.4$ to 0.5.
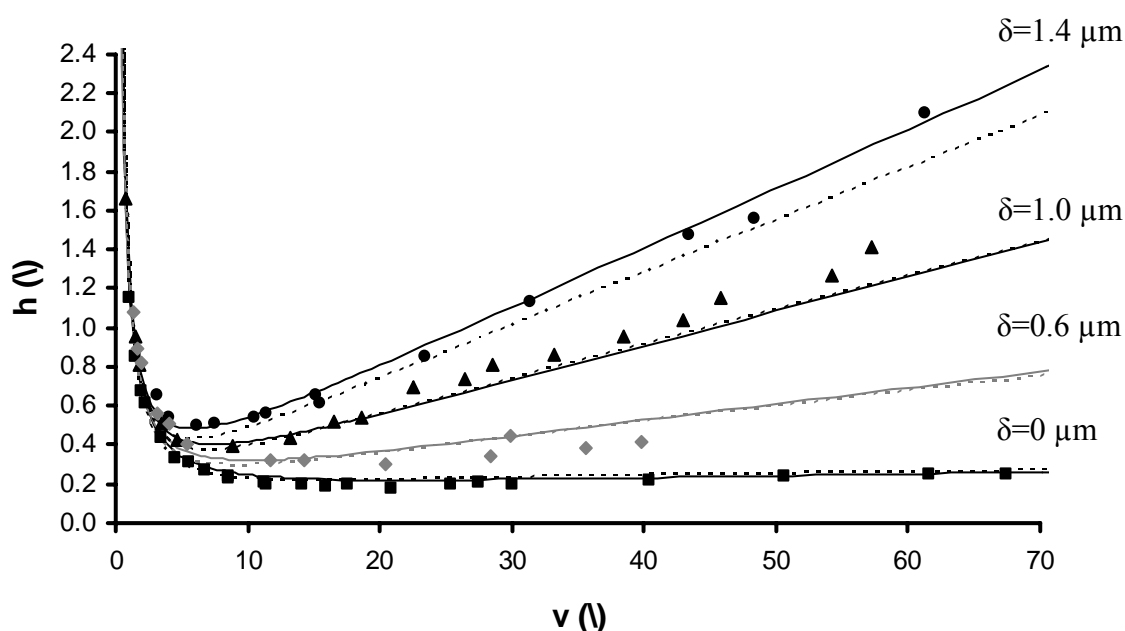
Fig. 4 Reduced van Deemter curves (normalized to the pillar diameter) established for coumarin C480 in MeOH in pillar beds with increasing porous shell layer thicknesses (uncoated pillar case). The respective thicknesses are 0, 0.6, 1.0 and 1.4 μm. The 0.6 μm value was taken from [14] to check the fitting quality and to confirm that the internal porosity value of 0.73 (as measured in ref [16]) is valid for the other shell layer thickness cases. Solid lines based upon Eq. (5a), dashed lines are based upon Eq. (5b).

Also added to Figure 4 is the non-retained component van Deemter curve (circular symbols) measured in a recent study[16] conducted in an array of porous shell pillars with a diameter of 10 μm and with a layer of thickness $\delta=0.6$ μm and produced with the same anodization procedure as in the current study. As can be noted, these data fit nicely in between the data sets of the present study (black symbols). Going up to reduced velocities of $v=70$, nearly no curvature of the C-term range of the van Deemter-curve is observed. This obviously is in agreement with the traditional notion that a curved C-term regime points at a strong eddy-

diffusion and hence at a large bed heterogeneity. In agreement with earlier computational fluid dynamics simulations,[27-28] the curvature that can be expected in perfectly ordered pillar array columns is very small.

Whereas all measurements shown in Figure 4 relate to a mobile phase consisting of pure methanol, we also conducted a series of experiments using increased volumetric fractions of aqueous phosphate buffer at pH=3. The obtained results are shown in Figure 5.
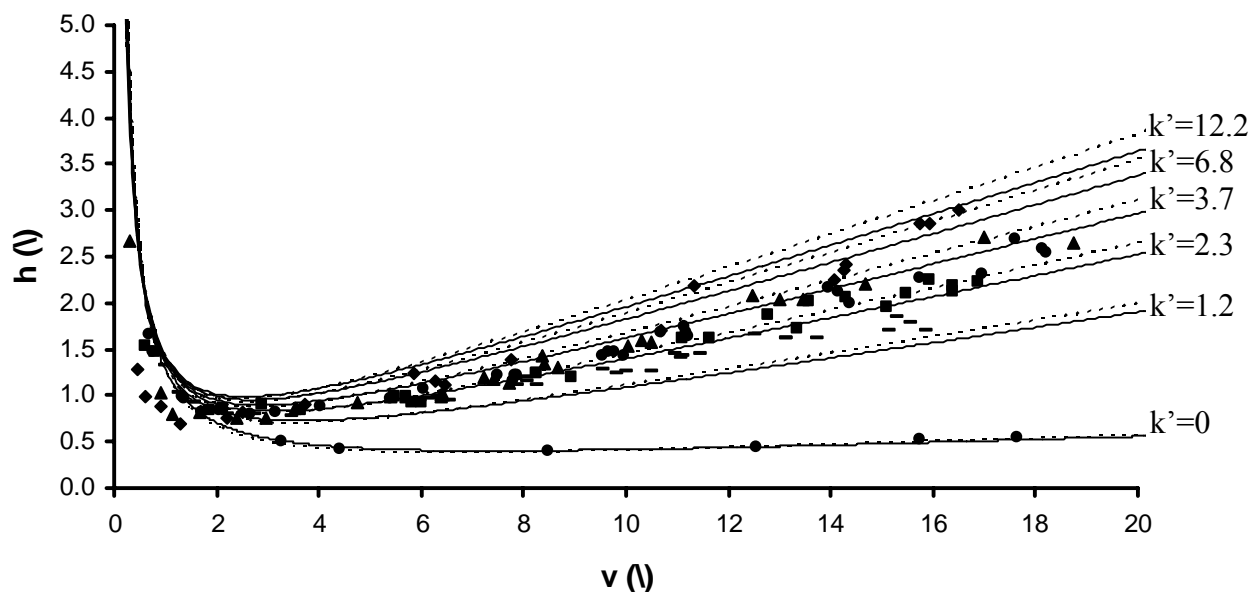
Fig. 5 Reduced van Deemter plots for C480 in different water-methanol compositions in a pillar array with a shell thickness of 1 μm after a 24 h coating procedure (see text for details). The volumetric methanol fractions in the employed mobile phase was respectively equal to 100 %, 65%, 60 %, 55 %, 50 % and 45 % from bottom to top. Solid lines based upon Eq. (5a), dashed lines are based upon Eq. (5b).

Plotting the data versus the reduced velocity, the effect of the changing molecular diffusion coefficient (D_{mol} roughly decreases from $1.2 \ 10^{-9}$ m^2/s to $4.0 \ 10^{-10}$ m^2/s if going from pure methanol to a 50 %/50% MeOH/water) is cancelled out. As can be noted, the reduced plate heights in the C-term dominated part of the curve increase with increasing retention factor, with the largest increase observed for the initial increase, i.e. if going from a zone retention coefficient k"=0.4 (k'=0) to k"=2.0 (k'=1.2). Further increases in k" lead to a less strong increase of the C-term dominated part of the curve. In agreement with the steeper C-term part of the curve, the increased retention also shifts the optimal velocity to lower values while the plate height minimum is shifted to higher values, although the latter is only really significant for the initial increase of k". Further increases in zone retention factor apparently only have a minimal effect on the plate height minimum. Even under the most strongly retained component conditions (k'=12), the minimal plate heights remain around h_{min}=0.9, i.e.,

significantly smaller than in packed bed columns, for which it is generally assumed that $h_{min}=2$.[29-30]

7.4.3.2 Establishment of a theoretical plate height model

To better understand the obtained data, they were interpreted by fitting them to a theoretical model based on Giddings' non-equilibrium theory[31] and the general rate model.[32-33]

Assuming that the different mass transfer processes occurring in a chromatographic column occur independently of each other,[31] analytical expressions can be established to link the mobile and stationary zone mass transfer contributions to the different system parameters such as mobile zone velocity, particle diameter, phase or zone retention factor (resp. k' and k") and mobile and stationary zone diffusion coefficient. Introducing the symbols C_m and C_s as the proportionality constants between the interstitial velocity and H, it is a well-established fact that, under the above assumptions, the band broadening in a chromatographic column can always be written as:[29, 32-35]

$$H=2D_{ax}/u_i+ C_m\, u_i + C_s\, u_i \qquad (3)$$

For a correct use of below expressions, it is crucial to recognize that the u_i-velocity appearing in Eq. (3) is the interstitial velocity.

Usually, D_{ax} is written as the sum of a molecular diffusion and a convection-based dispersion term:[32,35-36]

$$D_{ax} =\gamma_1 D_{mol}+ \gamma_2 u_i\, d_p \qquad (4)$$

More complex expressions for the velocity-dependent part of D_{ax} are however conceivable.[33] In the present study, two types of D_{ax}-models have been compared. The first expression is given by :

$$D_{ax} = D_{mol}\, (\gamma_1+\gamma_2 v^n) \qquad (5a)$$

wherein v_i is the reduced velocity $v=u_i d_p/D_{mol}$. If used with n=4/3, this expression reduces to the empirical Knox-Parcher expression.[41] Although the latter is purely empirical, it has been used by many authors to investigate the packing homogeneity of packed bed columns. It is therefore instructive to compare the A-term values found in the presently studied perfectly ordered pillar array with that obtained in typical packed bed column.

A second D_{ax}-expression that has been considered is that obtained by Giddings via his coupling theory:[31]

$$D_{ax} = D_{mol} \left[\gamma_1 + \left(\frac{1}{\gamma_3} + \frac{1}{\gamma_4 . \nu} \right)^{-1} . \nu \right] \qquad (5b)$$

More complex expressions for D_{ax}, such as the one proposed by Gritti and Guiochon[33] have not been considered in the present study because they involve short-range and long-range inter-channel coupling effects[31] which are anyhow absent in perfectly ordered pillar array columns.

To fill in the second term of Eq. (3), it can be established from the general theory of chromatography that:[29, 31, 34, 35, 37]

$$C_m = \gamma_m \frac{k''^2}{(1+k'')^2} \frac{d_p^2}{D_{mol}} \qquad (6)$$

Wherein γ_m is a proportionality constant, mainly related to the geometry of the system, and depending on the dimensionless film mass transfer coefficient Sh (Sh=Sherwood-number=$k_f d_p / D_{mol}$) via:[34]

$$\gamma_m = \gamma_m' / Sh \qquad (7)$$

In its general form, Sh can be expressed as:[40]

$$Sh = \gamma_d + \gamma_c \nu^m \qquad (8)$$

with the exponent m usually varying between 0 and 1. The combination of Eqs. (6) and (7) leads to a C_m-term that is for example identical to the term with $1/k_{ext}$ in Eq. (29) of Kaczmarski and Guiochon.[22] When the velocity-dependent term in Eq. (8) is cancelled, the C_m-term is a linear function of u_i. When putting m=1/3 and γ_d=0 and γ_c=1.09/ε in Eq. (8), the C_m-expression in Eq. (6) becomes proportional to $u^{2/3}$ and is equal to the H_{kf}-expression in Eq. (60A) of Guichon and Gritti for packed beds.[33] In the present study (see further on), a model wherein only the first term of Eq. (8) is used appears to be sufficient, because the plate height data obtained in the presently investigated pillar array column do not show a $u^{2/3}$-dependency but rather a purely linear dependency with u (see further on).

As can be noted, the intrinsic retention parameter appearing in the expressions for C_m is the zone retention factor k'', i.e., the retention factor with respect to the interstitial velocity. This retention factor is different from the phase retention factor k'. The latter is directly measurable from the retention time of an unretained t_0-marker, and is hence more often used in the field

of chromatography than the zone retention factor. Fortunately, the zone and phase retention factor can be freely interchanged starting from the two following identities:

$$u_i\varepsilon= u_0\ \varepsilon_T \tag{9}$$

$$t_R=L/u_i(1+ k'') = L/u_0(1+ k') \tag{10}$$

from which:

$$k''=(1+ k')\ \varepsilon_T/\varepsilon-1 \tag{11}$$

$$\varepsilon_T=\varepsilon+(1-\varepsilon)\varepsilon_{int}(1-\rho^2) \tag{12}$$

with ε_T defined as the total porosity and ρ the ratio of the internal and the external shell diameter. As can be noted from Eq. (11), the zone retention factor k'' retains a non-zero value in the case of a component with $k'=0$. This non-zero value simply reflects the fact that species that are not retained are still temporarily arrested with respect to the interstitial flow each time they enter the part of the mobile phase held stagnant in the mesopores of the particles. Defining the zone retention factor for the $k'=0$-case as k''_0, we obtain by putting $k'=0$ in Eq. (11):

$$k''=k''_0=\varepsilon_T/\varepsilon-1 \tag{13}$$

Which, using Eq. (12), can be conveniently rewritten as:

$$k''_0=[(1-\varepsilon)/\varepsilon]\varepsilon_{int}(1-\rho^2) \tag{14}$$

As shown in [39-40], the relation between the zone and phase retention factors given in Eq. (11) can also be rewritten as:

$$k''= k'+(1+k')k_0'' \tag{15}$$

To calculate the C_s-constant appearing in Eq. (3), the non-equilibrium theory established by Giddings[31] offers an analytical expression describing the dependency on the pillar diameter and the zone retention factor:

$$C_s=\frac{q_f}{4}\frac{k''}{(1+k'')^2}\frac{d_p^{\ 2}}{D_{part}} \tag{16}$$

as well as a method to calculate the configuration factor q_f. Applying this method for the particular case of a porous shell pillar, the following expression is obtained (see Appendix):

$$q_f=2\theta_m=\frac{\dfrac{1}{4}-\rho^2+\dfrac{3}{4}\rho^4-\rho^4\ln\rho}{1-\rho^2} \tag{17}$$

The assumption underlying Eq. (16) is that the porous shell layer can be considered as a homogeneous material with a uniform intra-particle diffusion coefficient D_{part}.[31] This implies that D_{part} is the diffusion coefficient expressing the species diffusion rate in a black-box control volume fitting completely into the porous layer zone (cf. Eq. (A-38b) of [40]). D_{part} is hence also equal to the D_s-parameter in Giddings' original C_s-term expression for a spherical particle (cf. Eq. (4.4-44) in [31]). It is also equal to the D_{sz}-coefficient used in the classical paper on the B- and C-term dispersion by Knox and Scott.[39] D_{part} however differs, by a factor K_p (K_p=whole-particle based retention equilibrium constant), from the effective diffusion constant D_e systematically used in the literature based on the general rate model.[32-33] In [40], it was shown that $D_{part}=D_e/K_P$.

Making the (highly probable) assumption that the diffusion of the species in the mobile phase filling the mesopores (during which they are subjected to a diffusion coefficient $\gamma_{ms}D_m$) occurs in parallel with the diffusion of the species being in a retained state at or near the pore walls (during which they are subjected to a diffusion coefficient $\gamma_s D_s$), D_{part} can be expressed in terms of these two independent diffusion rates. As already shown in,[39] the correct expression for D_{part} under the above assumptions is given by (see also [40]):

$$D_{part} = \frac{\psi\gamma_{ms}D_m + k'\gamma_s D_s}{\psi + k'} \quad \text{with} \quad \psi = k''_0 /(1 + k''_0) \qquad (18)$$

The non-retained component zone retention factor k''_0 appearing in Eq. (18) can be directly calculated from Eq. (14).

7.4.3.3 Fitting strategy and results

The fitting of the plate height data proceeded in two subsequent steps. In the first step, the D_{ax}-term of Eq. (3) is fitted to the non-porous, non-retained plate height data, because in this case the C_m- and C_s-terms are still zero (because k''=0). In the second step, the porous pillar plate height data (for which k''>0) are used to fit the C_m-term contribution, retaining the fitting of the D_{ax}-term obtained in the first step. This approach is consistent with the general rate model, where the D_{ax}-band broadening (only source of band broadening if k''=0) and the C_m- and C_s-terms (only active if k''>0) are assumed to be independent and can be simply added.[22,32,33,35]

First, however, all parameters appearing in Eqs. (4)-(18) for which a good *a priori* estimate exists were fixed (see Table 2). The value of the external porosity was estimated from optical

microscopy images of the channels. The value of ρ follows in a straightforward manner from the measurement of δ and from the definition of ρ (cf. Eq. A-4 in the appendix). The value of ε_{int} (ε_{int}=0.73) was taken from a previous paper wherein the same anodization method was used. This type of high internal porosity values is typical for porous silicon.[28] The value of γ_1 was kept close to the value of γ_1=0.62 that was obtained in a numerical computation study of the B-term dispersion in cylindrical arrays[40] for the case of non-porous cylinders packed with an external porosity of ε=0.4.

The value of the exponent n appearing in Eq. (5a) was fixed at n=1.33. Fits with other values of n lead to nearly indistinguishable results, but knowing from previous fitting experiences that the band broadening in pillar array columns with low external porosity can be relatively closely fitted using an A-term with a velocity exponent 0.33, as is the case in the empirical Parcher and Knox-correlation,[41] n was put at 1.33 (an exponent n=1.33 in the D_{ax}-expression yields an exponent 0.33 in the H-expression). For the second considered expression for D_{ax} (Eq. 5b), no good a priori values for the two parameters appearing in it were available. Hence, they both needed to be determined in the first fitting step (see further on).

The molecular diffusion coefficients of coumarin 480 for the different mobile phase compositions were estimated using the value (see Table 2) measured in pure methanol in an open-tubular shear-driven flow channel,[40] and subsequently using the Wilke-Chang correlation[33, 43] to estimate the molecular diffusion coefficients for the other mobile phases:

$$D_m = \frac{D_{m,100\%}\eta_{100\%}\sqrt{M_{MeOH}\phi_{MeOH}}}{\eta\sqrt{\chi_{H_2O}M_{H_2O}\phi_{H_2O} + \chi_{MeOH}M_{MeOH}\phi_{MeOH}}} \tag{19}$$

The values for the viscosity needed in Eq. (19) were taken from[44]. Other parameters appearing in Eq. (19) are the molecular weight M, the association factor ϕ (2.6 and 1.9 for water and methanol, respectively) and the molar fraction χ.

The two parameters appearing in the expression for D_{part} were respectively put at γ_{ms}=0.75 (estimated from Figure 7 of [45] for a system with internal porosity of ε_{int}=0.7 and larger) and at $\gamma_s D_s/D_m$=0.1.[39] Although these are only crude estimates, the plate height data are so weakly influenced by the C_s-term contribution (see Section 3.2.4) that a more accurate estimate was not needed to significantly improve the fitting.

In the first actual fitting step (see Table 2), the plate height curve of the unretained, non-porous pillar case (bottom solid line curve in Figure 4) was first fitted to determine the value of γ_2 appearing in Eq. (5a) This yielded a best fit value of $\gamma_2=0.06$. After inserting Eq. (5a) into Eq. (3), an expression is obtained that is identical to the frequently employed, yet physically unsound Knox-Parcher correlation:[41]

$$h = A'\nu^{1/3} + B'/\nu + C'\nu \tag{20}$$

It can be verified that the A'-factor appearing in this expression is equal to the γ_2-constant. From its best fitted value, it can hence be concluded that the obtained A'-value is much smaller (A'= γ_2=0.06) than in a traditional packed bed (for which typically A'≥0.5). This is of course in agreement with the generally accepted notion that the A-term is a measure for the bed heterogeneity (see also [27-28]).

Table 2. Employed model parameters used to fit the plate height data shown in Figs. 4 and 5.

A priori fixed			
R	10 μm	$\gamma_s D_s/D_m$	0.1
δ	0;0.6;1.0;1.4 μm	ρ	see Eq. (A-4)
$\varepsilon_{int,bef.\ coat.}$ (\)	0.73	q_f	see Eq. (A-10)
$\varepsilon_{int,after\ coat.}$ (\)	0.6	Fitting step 1	
ε (\)	0.42	γ_2	0.060 (± 0.002)
γ_1	0.6	γ_3	0.32 (± 0.02)
n	0.33	γ_4	0.016 (± 0.002)
$D_{m,100\%\ MeOH}$	1.2 10^{-9} m^{2}s^{-1}	Fitting step 2	
γ_{ms}	0.75	γ_m	0.20 (± 0.02)

As an alternative for the expression in Eq. (5a), we have also considered the physically more sound Giddings-expression to model D_{ax} (see Eq. 5b). With one additional fitting parameter, the Giddings model clearly gives a better fitting of the data (see bottom dashed line curve).

In the second fitting step, the three other non-retained component curves appearing in Figure 4, i.e., those relating to the porous shell pillar arrays with respectively δ=0.6; 1.0 and 1.4 μm, were used to find a best fitting value for γ_m, i.e., the proportionality constant appearing in the

expression for C_m and the only model parameter that is still freely variable at this stage (the parameters appearing in the expression for C_s are already all fixed at this stage). As can be noted (see solid line curves), the three experimental curves can all be reasonably well fitted using the same value for γ_m ($\gamma_m = 0.20$), a strong indication of the general validity of the model established in Section 3.2. This value did not change significantly if modelling D_{ax} using Eq. (5b) with the fitted parameters γ_3 and γ_4 given in Table 2. Over-all, the quality of this second approach is slightly better (see dashed line curves). This slightly better fit does however not significantly alter the value for γ_m, because both fitting approaches (using either Eq. (5a) or (5b) to model the k''=0-part of the band broadening) yield within the error margin an identical γ_m –value ($\gamma_m = 0.20$) if fitting the k''>0-part of the band broadening. This finding is in agreement with the additive rule underlying the general rate model, wherein it is assumed that the D_{ax}-band broadening and the C_m- and C_s-terms are independent and can therefore be simply added. Hence, when the D_{ax}-band broadening is sufficiently well-fitted, the choice of the mathematical expression used to make this fitting should have no effect on the parameter values appearing in the other terms (C_m and C_s) of Eq. (3).

The validity of the adopted modelling approach is further emphasized in Figure 5, where it can clearly be noted that the model parameter values obtained in the different fitting steps performed in Figure 4 still hold under retained component conditions and allow to relatively accurately predict the plate height values under these conditions. To calculate the model curves appearing in Fig. 5, the only change that was made to the model parameters was a change of the intra-particle porosity from 0.73 to 0.6 to account for the change in intra-particle porosity after the C8-coating.

To assess the uncertainty on the fitted model parameters, a parameter sensitivity study has been made. The values given between the brackets in Table 2 correspond to the variation of the investigated parameter in response to a change of 5% of the fitting residuals.

*7.4.3.4 Relative importance of C_m- and C_s-term band broadening in porous shell pillar arrays*
Noting that in reduced plate height and velocity coordinates the C_m- and C_s-factors appearing respectively in Eqs. (6) and (16) translate into:

$$C_m' = \gamma_m \frac{k''^2}{(1+k'')^2} \qquad (21)$$

$$C_s' = \frac{q_f}{4} \frac{k''}{(1+k'')^2} \frac{1}{D_{part}/D_{mol}} ,$$

(22)

we can now use the values of the fitted constants to calculate how large the values for C_m' and C_s' can typically be expected to be in a cylindrical pillar array column and how they can be expected to vary with the retention factors k' and k''. The result is shown in Fig. 6. The most important observation that can be made from this figure obviously is that the values for C_m' are significantly larger (about one order of magnitude) than those for C_s', even for the case with the largest shell layer (ρ=0.72).
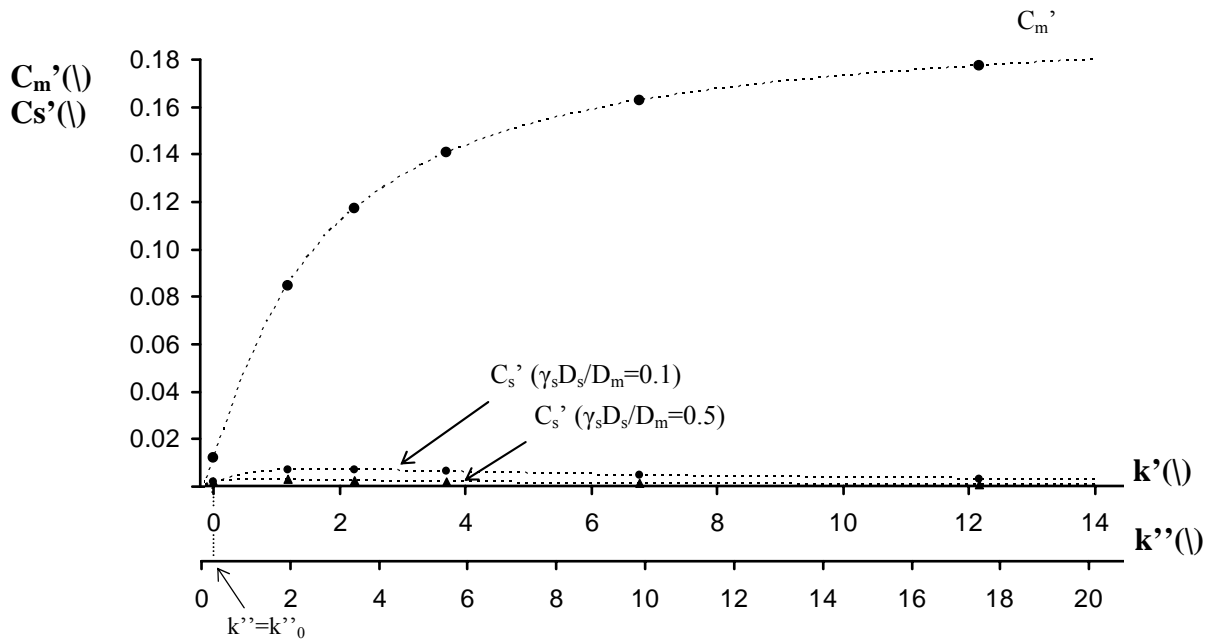
Fig. 6 Theoretical values of C_m' and C_s' as a function of the phase and zone retention factor k' and k'' (see Eq. 15 for relation between both factors) for a porous shell pillar with layer thickness δ=1 μm.

This very large C_m' is most probably due to the fact that the anodization method used for the creation of the porous shell layers cannot prevent that a layer with similar depth is also formed on the bottom of the channels (cf. Figure 1b). The presence of the bottom porous layer can be expected to induce a band broadening having a pure linear velocity dependence.[46] Knowing that the presence of this layer requires a velocity equilibration along the depth-coordinate of the pillar arrays, its presence can be expected to lead to relatively large contribution to the C-term band broadening, in any case significantly larger than the value of C_m'=0.003 that can be estimated from Figure 5 of [47] for the case of a non-porous top and bottom wall. The (currently) inevitable presence of the porous bottom layer hence also

explains why the combined Cs'- and C_m'-value is significantly larger than in a packed column, for which it is typically assumed that C'=0.05 to 0.1.[48, 30]

Reflecting the k"-dependency of Eq. (22), the C_s'-values go through a maximum around k"=1, and then slowly decrease again. Fig. 6 shows two C_s'-curves, one for $\gamma_s D_s/D_m$=0.5 and one for $\gamma_s D_s/D_m$=0.1. As can be noted, the difference between the absolute values is small (maximum a h-contribution of 7 % of the total h at ν=14). This difference is so small that an experimental determination of the value of $\gamma_s D_s/D_m$ via a fitting procedure would anyhow only have lead to a value with a very poor significance, hence the use of the present literature data estimation. Given that the top wall and the porous layer at the bottom of the pillar arrays can be assumed to have a relatively large contribution to the total C_m'-contribution, and given that the C_s'-value is relatively small, even for fully porous pillars (for which q_f=1/4), it can be assumed that if a method could be found to prevent the formation of the porous bottom layer, the pillar arrays would have a minimal plate height around h_{min}=0.7 as predicted in [49] for the case of fully porous cylinders with a zone retention factor of k"=2 (or if one would also include the effect of the top and bottom layer $h_{min}\cong$0.75, see [47]. Switching then to diamond shaped pillars or to elongated rectangular pillar structures, plate heights in the range of h_{min}=0.5 to 0.65 should be possible.[49]

7.4.3.5 Multi-component sample separation

In a final series of experiments, separations of a 4-component mixture of coumarin dyes were performed.
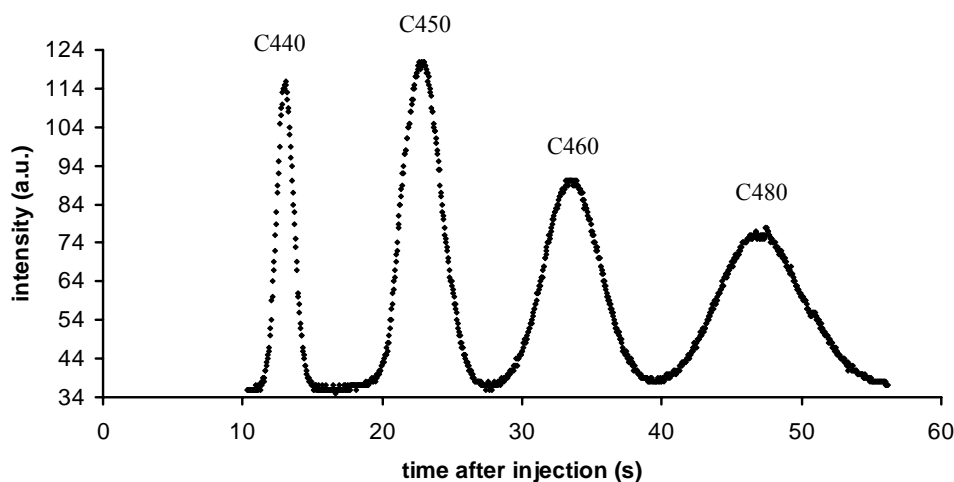
Fig. 7 Chromatogram of C440, C450, C460 and C480 in 40/60 (v/v) water/methanol (pH 3) monitored at 3.3 mm downstream the injection slit. The mobile phase velocity was 0.24 mm/s.

As can be noted, the four components are base-line separated after about 3 mm of channel length and in less than one minute, despite the use of 10 micrometer sized pillars. As can be noted, the bands clearly show a good symmetry.

7.4 Conclusions

Electrochemical anodization is a good technique to obtain (partially) porous micro-pillar array columns. Pore sizes are in the order of 5-10 nm and the internal porosity can be assumed to be very high (order of 75%). The lack of mechanical stability of smaller sized pillars (i.e. <5 μm) currently is a concern and needs further development work.

The band broadening in silicon porous shell pillar arrays can be accurately predicted using a theoretical plate height model based on Giddings' non-equilibrium theory. The obtained h_{min}-values are very low ($h_{min}=0.4$ to 0.5 under non-retained conditions and $h_{min}\cong0.9$ under retained conditions, even at retention factors up to k'=12), as a reflection of the perfect homogeneity of the pillar beds. It can be assumed that, if the formation of a porous layer at the bottom of the channels could be prevented, the minimal plate height would even be smaller.

In fact, the present study provides the first experimental indication that the theoretical potential of perfectly ordered and fully porous pillar array columns calculated by means of computational fluid dynamics[4-5] could indeed be achieved in practice. According to these calculations, and depending on the shape of the pillars, minimal plate heights of the order of $h_{min}\cong0.55$ to 0.75 should be possible under retained component conditions.

Of course, a number of major hurdles still need to be crossed. Good solutions for the mechanical stability of the pillars, as well as a method to prevent that the layers are also formed on the bottom layer need to be developed. Also the possibility to fabricate pure silica-based pillars needs to be investigated.

7.5 Appendix

According to Giddings non-equilibrium theory, [31] the configuration factor appearing in the expression for the stationary zone mass transfer contribution can be calculated from a function dimensionless function θ, respecting the following differential equation and set of boundary conditions:

$$\nabla^2\theta = -1 \tag{A-1}$$

with $\dfrac{d\theta}{dr} = 0$ at the symmetry planes or closed internal surfaces (A-2a)

and $\theta = 0$ at the outer surfaces. (A-2b)

In Eq. (A-1), is the Laplacian operator expressed in dimensionless units.

For the presently considered cylindrical geometry, the Laplacian operator can be written in terms of the dimensionless radius r' (r'= r/R), so that Eq. (A-1) becomes:

$$\frac{1}{r'}\frac{d}{dr}(r'\frac{d\theta}{dr'}) = -1 \tag{A-3}$$

defining the position of the porous shell/solid pillar interfaces as:

$$\rho = \frac{R-\delta}{R} = \frac{R_i}{R} \tag{A-4}$$

the boundary conditions in Eq. (A-2) can be written as:

$$\theta = 0 \ \text{at} \ r'=1 \tag{A-5a}$$

$$\frac{d\theta}{dr'} = 0 \ \text{at} \ r'=\rho \tag{A-5b}$$

After a first integration with respect to r, Eq. (A-3) becomes

$$\frac{d\theta}{dr'} = -\frac{r'}{2} + \frac{\rho^2}{2}\ln r' + \text{constant} \tag{A-6}$$

Using the boundary condition in Eq. (A-5b), this gives:

$$\theta = \frac{1}{4}(1-r'^2) + \rho^2 \ln r' \ \text{with} \ \rho \le r' \le 1 \tag{A-7}$$

In the second step in the calculation of the configuration factor, the q-function needs to be averaged over the volume of the stationary zone. In the case of a cylindrical geometry, the averaging procedure corresponds to calculating below ratio of integrals:

$$\overline{\theta} = \frac{2\int_\rho^1 \theta r' dr}{2\int_\rho^1 r' dr} \tag{A-8}$$

yielding:

$$\overline{\theta} = \frac{\dfrac{1}{8} - \dfrac{1}{2}\rho^2 + \dfrac{3}{8}\rho^4 - \dfrac{\rho^4}{2}\ln\rho}{1-\rho^2} \tag{A-9}$$

In the final step of Giddings' procedure, the configuration factor is obtained by calculating:

$$q_f = 2\bar{\theta} \qquad (A\text{-}10)$$

As a validation check, it can be verified that if ρ tens to zero (case of fully porous pillars), the configuration factor takes the value of $q_f=1/4$, in agreement with the value obtained by Giddings for a fully porous cylinder (cf. Eq. (4.4-38) of [31]. At the other extreme, i.e., for ρ tending to unity (case of no shell layer), it can be verified that the expression in Eq. (A-9) yields a configuration factor of zero, in agreement with the physical meaning of q_f and C_s.

Symbols

H	height of a theoretical plate (m)
$\sigma_{x,0}$	initial spatial peak standard deviation (m)
$\sigma_{x,e}$	final spatial peak standard deviation (m)
δ	porous shell thickness (m)
k'	phase retention coefficient (/)
k''	zone retention coefficient (/)
k''_0	zone retention coefficient when $k'=0$ (/)
S	solvent strength (/)
Φ	volumetric fraction of organic modifier (/)
ε_{int}	internal porosity (/)
h	reduced plate height (/)
h_{min}	minimal reduced plate height (/)
D_m	molecular diffusion coefficient (m^2/s)
C_m	see Eq. 3 (s)
C_s	see Eq. 3 (s)
D_{ax}	axial dispersion coefficient (m^2/s)
u_i	interstitial velocity (m/s)
γ_1	geometrical factor, see Eq. 4 (/)
γ_2	geometrical factor, see Eq. 4 (/)
γ_3	geometrical factor, see Eq. 5b (/)
γ_4	geometrical factor, see Eq. 5b (/)
γ_m	proportionality constant of the C_m term, see Eq. 6 (/)
$\gamma_{m'}$	geometrical factor, see Eq. 7 (/)
γ_d	geometrical factor, see Eq. 8 (/)
γ_c	geometrical factor, see Eq. 8 (/)
γ_{ms}	geometrical factor, see Eq. 18 (/)
γ_s	geometrical factor, see Eq. 18 (/)
ε_T	total porosity (/)
ε	external porosity (/)
ρ	ratio of the internal and the external pore shell diameter (/)
C_m'	see Eq. 21 (/)
C_s'	see Eq. 22 (/)
q_f	Giddings' configuration factor (/)
D_{part}	intra-particle diffusion coefficient (m^2/s)
θ_m	Giddings' dimensionless function, see Eq. A-1 (/)

Φ   association factor (/)
M   molecular weight (g/mol)
χ   molar fraction (/)
η   viscosity (m^2/s)

References

1. He, B.; Tait, N.; Regnier , F.E. *Anal. Chem*. **1998**, *70*, 3790-3797.
2. Regnier, F.E., *J. High Resol. Chromatogr*. **2000**, *23*, 19-26.
3. Slentz, B.E.; Penner, N.A.; Regnier, F., *J. Sep. Sci*. **2002**, *25*, 1011-1018.
4. Gzil, P.; Vervoort, N.; Baron G.V.; Gert Desmet, *Anal. Chem.* **2004**, *76*, 6707-6718.
5. De Smet, J.; Gzil, P.; Vervoort, N.; Verelst, H.; Baron, G. V.; Desmet G. *Anal. Chem.* **2004,** *76*, 3716-3726.
6. De Pra, M.; Kok, W.Th.; Gardeniers, J.G.E.; Desmet, G.; Eeltink, S.; van Nieuwekasteele, J.W.; Schoenmakers, P.J., *Anal.Chem*. **2006**, *78*, 6519-6525.
7. Eghbali, H.; De Malsche, W.; De Smet, J.; Billen, J.; De Pra, M.; Kok, W.T.; Schoenmakers, P.J.; Gardeniers, H.; Desmet, G**.** *J. Sep. Sci.* **2007**, *30*, 2605-2613.
8. De Pra , M.; De Malsche, W.; Desmet , G.; Schoenmakers, P.J.; Kok W. T. *J. Sep. Sci.* **2007**, *60*, 1453-1460.
9. De Malsche, W.; Eghbali, H.; Clicq, D.; Vangelooven, J.; Gardeniers, H.; Desmet, G. *Anal. Chem.* **2007**, *79*, 5915-5926.
10. Eghbali, H.; De Malsche; W., Clicq; D., Gardeniers; H., Desmet, G. *LCGC Europe*, **2007**, *4*, 208-222.
11. De Pra, M; Kok, W.T.; Schoenmakers,P.W. *J. Chromatogr. A* **2007**, doi.org/10.1016/j.chroma.2007.09.086
12. Mogensen, K. B.; Petersen, N. J.; Hübner, J.; Kutter, J. P. *Electrophoresis* **2001**, *22*, 3930-3938.
13. Petersen, N. J.; Mogensen, K. B.; Kutter, J. P. *Electrophoresis* **2002**, *23*, 3528-3536.
14. Lindberg, P.; Dahlin, A.P.; Bergstrom; S.K.; Thorslund, S.; Andren, P.E.; Nikolajeff, F.; Bergquist *J.Electrophoresis* **2006**, *27*, 2075-2082.
15. Thorslund, S.; Lindberg, P.; Andrén, Nikolajeff, P.E.F.; Bergquist, *J. Electrophoresis* **2005** *26*, 4674-4683.
16. De Malsche, W.; Clicq, D.; Verdoold, V.; Gzil, P.; Desmet, G.; Gardeniers, H. *Lab Chip* **2007**, *7*, 1705-1711
17. Laurell, T.; Drott, J.; Rosengren, L.; Lindström, K. *Sensor Actuat B* **1996**, *31*, 161-166.
18. Lendl, B.; Schindler, R.; Kellner, R.; Drott, J.; Laurell, T. *Anal. Chem.* **1997**, *69*, 2877-2881.
19. Tjerkstra, R.W.; De Boer, M.; Berenschot, E.; Gardeniers, J.G.E.; van den Berg, A.; Elwenspoek, M.C. *Electrochim. Act*. **1997**, *42***,** 3399-3406.
20. Clicq, D.; Tjerkstra, R.W., Gardeniers, J.G.E.; van den Berg, A.; Baron, G.V.; Desmet, G. *J. of Chromatogr. A* **2004**, *1032*, 185-191.
21. Cavazzini, A.; Gritti, F.; Kaczmarski, K.; Marchetti, N.; Guiochon, G. *Anal. Chem.* **2007**, *79*, 5972-5979.
22. Kaczmarski, K.; Guiochon, G. Anal. Chem. **2007**, *79*, 4648-4656.
23. Blom, M.T.; Chmela, E.; Oosterbroek, R.E.; van den Berg A. *Anal. Chem.* **2003**, *75*, 6761-6768.
24. Chmela, E.; Tijssen, R.; Blom, M.T.; Gardeniers H.J.G.E.; van den Berg, A. *Anal. Chem.* **2002**, *74*, 3470-3475.

25. Neue, U.D., *HPLC columns: theory, technology and practice*, Wiley-VCH: New York, 1997.
26. Canhan, L.; Malvern, D., *Properties of Porous Si*, Inspec, London, 1997.
27. Billen, J. Gzil, P.; Vervoort, N.; Baron, G. V.; Desmet, G., *J. Chromatogr. A*, **2005**, *1073*, 53-61.
28. Billen, J.; Gzil, P.; Baron, G.V.; Desmet, G. *J. Chromatogr. A*, **2005**, *1077*, 28-36.
29. Knox, J.H. *J. Chromatogr. A* **1999**, *831*, 3-15.
30. Poppe, H. *J. Chromatogr. A* **1997**, *778*, 3-21
31. Giddings, J.C., Dynamics of Chromatography Part 1, Marcel Dekker, New York, 1965.
32. Ruthven, D.M., *Principles of adsorption and adsorption processes*, John Wiley and sons, New York, 1984.
33. Gritti, F.; Guiochon, G., *Anal. Chem.* **2006**, *78*, 5329-5347.
34. Huber, J., *J. Chromatogr. Sci.* **1969**, *7*, 85-90.
35. Guiochon, G.; Golshan-Shirazi, S.; Katti, A. M., *Fundamentals of Preparative and Nonlinear Chromatography*, Academic Press, Boston, 1994.
36. Miyabe, K. *J. Chromatogr. A* **2008**, *1183*, 49-64.
37. Knox, J. H. *Ann. Rev. Phys. Chem.* **1973**, *24*, 29-49.
38. Dykaar, B.B.; Katinidis, P.K. *Water Resources Research* **1996**, *32*, 307-320.
39. Knox, J.H.; Scott, H.P. *J. Chromatogr. A* **1983**, 282, 297-313.
40. Desmet, G.; Broeckhoven, K.; De Smet, J.; Deridder, S.; Baron G.V.; Gzil, P. *J.Chromatogr. A* **2008**, doi:10.1016/j.chroma.2008.02.018
41. Knox, J.H.; Parcher, J.F., *Anal. Chem.* **1969**, *41*, 1599-1606.
42. Pappaert, K.; Biesemans, J.; Clicq, D.; Vankrunkelsven S.; Desmet, G. *Lab Chip* **2005**, *5*, 1104-1110.
43. Wilke, C. R.; Chang, P. *AIChE J.* **1955**, *1*, 264.
44. Li, J; Carr, P.W. Anal. Chem. **1997**, *69*, 2530-2536.
45. Gritti, F.; Guiochon, G. *Chem. Eng. Sci.* **2006**, *61*, 7636-7650.
46. Desmet, G.; Baron, G. V. *J. Chromatogr. A* **2002**, *946*, 51-58.
47. De Smet, J.; Gzil, P.; Baron, G.V.; Desmet,G. *J. Chromatogr. A*, **2007**, *1154*, 189-197.
48. Knox, J. H. *Journal of Chromatography A* **2002**, *960*, 7-18.
49. De Smet, J.; Gzil, P.; Vervoort, N.; Verelst, H. Baron, G.V.; Desmet; G. *J. Chromatogr. A*, **2005**, *1073*, 43-51.

Chapter 8: Conclusions and future perspectives

8.1 Conclusions

As was shown in this thesis, the pillar array column has a tremendous potential for application in LC. It was demonstrated that the separation impedances can be as small as E=150, which is of the same order as the best currently existing monoliths. When comparing with the packed bed format, generally exhibiting higher separation impedances but lower plate heights, the plate heights that can be achieved using the pillar array are less than half of those in a packed bed column in both the porous and the non-porous pillar or particle case, see Fig. 1.
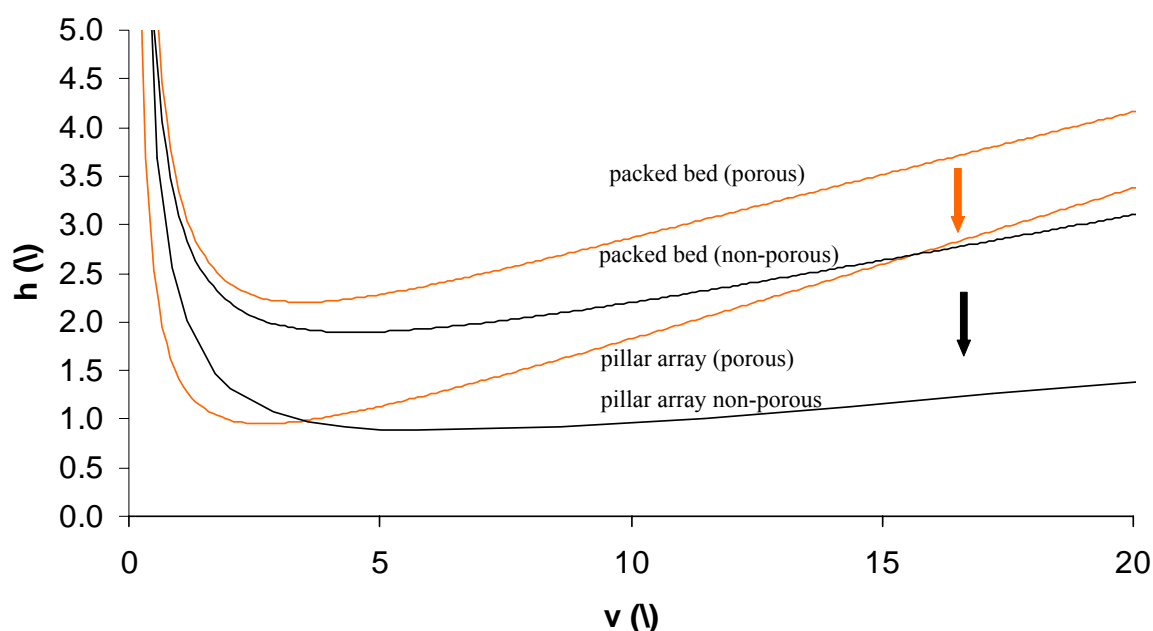
Fig. 1 Comparison between porous (k'=6.8, k''=9.8) and non-porous (k'=1.2) pillar array columns and a very good packed bed of porous particles (h=A'$v^{1/3}$+B'/v+C'v; A'=0.75, B'=2.5, C'=0.1) and non-porous particles (h=A'+B'/v+C'v; A'=1, B'=2, C'=0.1) in reduced coordinates. The external porosities are in all cases of the order of 0.4.

In order to allow a discussion on the best pillar dimensions, both the plate height and the separation impedance are processed in an (N-t_0/N^2) plot, see Fig. 2. In this Figure, the y-axis value is a direct measure for the time needed to reach a certain amount of theoretical plates. If a specific number of plates is required, the most time-economical solution is one for which the (N-t_0/N^2)-curve has its minimum at this specific N value. The plotted pillar array curve (black bold curve, pillar diameter=4.4 μm) has its minimum at around 400,000 plates. When comparing its kinetic performance curve to (the best possible) case of a 5 μm particle packed bed, the E values differ by more than a factor of 10 when assuming an identical pressure for

both formats (for example 60 bar). This means that when for both cases (pillar array and packed bed) the channel lengths have the exact length to still allow the working speed to be at the optimum of the van Deemter curve (see Fig. 1), the time needed to achieve 400,000 plates is 10 times less in the case of the pillar array when applying the same pressure. Even when a maximum pressure of 60 bar is assumed for the pillar array and 400 bar for the particle columns, a gain of a factor 2 is achieved.

There are two arguments to decrease the pillar size. First, to work with the current 4.4 μm pillars at the optimal plate generation velocity, a channel length of 1.6 m is required. As the maximum available wafer size is 30 cm, this would imply that turns have to be included in the channel. This would inevitably lead to additional dispersion, causing a partial loss of the separation power of the system. A second and probably more important reason, is that the established pillar curve has an optimum value at around 400,000 plates. A typical required value is actually smaller, i.e. 50,000 plates. The optimal N value scales according to $\sim d_p^2$. For this end, pillars on the order of 1 μm with an inter-pillar distance on the order of 250 nm should be fabricated (keeping the same external porosity). This would result in a shift of the curve towards lower N values (see red curve depicted in Fig. 2).
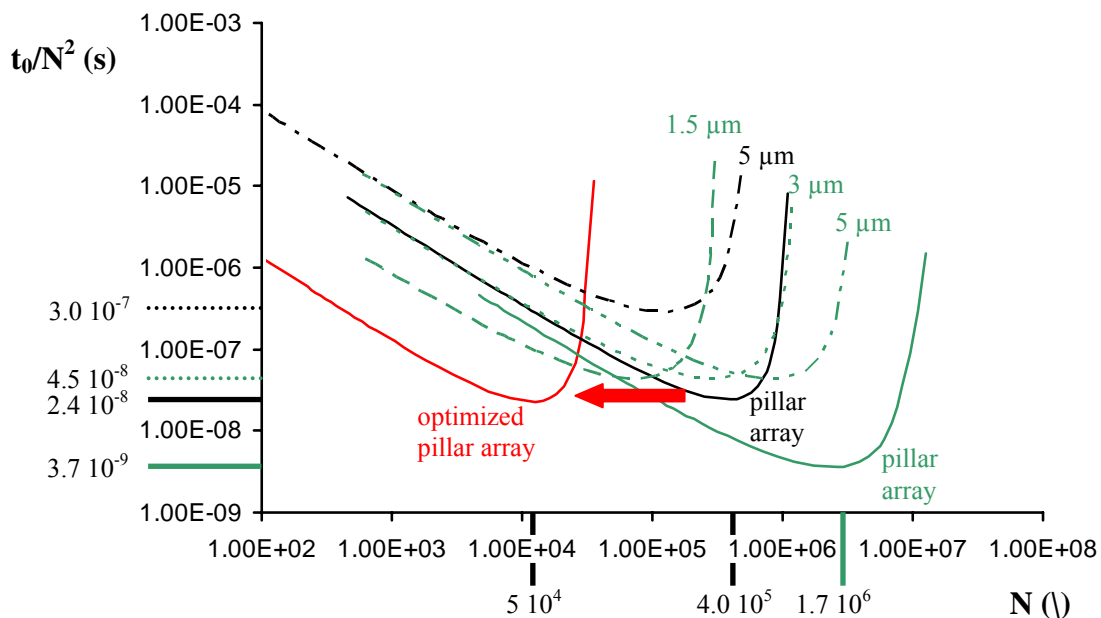
Fig. 2 Kinetic plot (separation impedance t_0/N^2 versus the number of theoretical plates N) comparing a non-porous pillar array column (d_p=4.4 μm, non-porous) with packed beds containing non-porous particles with different particle diameters (5, 3 and 1.5 μm). The parameters to establish the packed bed are A=1, B=2, C=0.1 (h=A+B/v+ Cv). The maximum allowable pressure for the packed bed and the pillar array column is compared between 60 bar (black curves) and 400 bar (green curves). The solid curves depict the pillar array. The red curve depicts the pillar array column operated at 60 bar when the pillar size would be reduced 3-fold.

Apart from its truly dramatic performance barrier shift, the chip format of the pillar array columns also brings along some benefits connected to the miniaturized format. A detector can be integrated in the channel itself (see chapter 5), in this way avoiding the typical performance losses due to external couplings. Apart from that, only very small volumes are needed for the analysis (order of nl), which is of great value for the different –omics fields where usually only limited sample volumes are available.

8.2 Future research

As has been pointed out repeatedly throughout this thesis, the sidewall effect is an effect that can completely destroy the excellent separation performance of the ordered pillar array. Because of a difference in local flow resistance between the sidewall region and the central part of the channel, a peak travelling through the channel suffers additional dispersion. In the case of channels with an external porosity of 0.4 and filled with 5 μm pillars, this distance is exactly known from CFD simulations and is 750 nm (and scales with the pillar size when keeping the same porosity).[1] Apart from the fact that this dimension is not achievable with the mid UV-lithography equipment typically available (at least in research institutes), this distance should be exact and repeatable. This requires exact control of the photoresist thickness and ambient factors but also preferably a projection lithography method (or a very low particle abundance in the case of contact lithography) should be used to allow uniformity. Another reason to lower the achievable dimension limit of the patterned and etched structures is that also a size reduction of the pillar itself (in the case of the absence of any sidewall effects), goes hand in hand with a decrease in plate height.

To address the above mentioned issues, two lithography methods are proposed (and have been shortly investigated experimentally in parallel) and will be discussed below: step-and-flash-imprint-lithography and deep-UV-lithography.

8.2.1 Step-and-flash-imprint-lithography

The very lowest critical dimensions that have been described in the literature were established by e-beam- lithography (EBL). This technique (with a resolution on the order 10 nm) can be interesting for use in proof-of principle devices.[2] It is however not feasible to use this technique to produce many devices given the high cost (a nano-patterned 4 inch wafer can easily cost 50,000 €). Another issue is that the resist and the applied thickness used in e-beam (EBL) is not sufficient to be used as a mask in a subsequent etching step, especially when

depths of the order of μm's are required.

During the last decade, a lot of research has been carried out on imprint technology. First hot-embossing emerged, requiring high temperatures as well as high pressures. Even though this is a powerful technique and the resolution is basically the resolution of the template (also very close to the resolution of EBL), an important drawback is that the pattern density should be quite homogenous over the substrate to avoid large variations in the residual layer thickness. This layer has to be etched after the imprint step. If at a given spot on the substrate this thickness is larger than the feature thickness on another spot, the feature will be completely removed and a defect occurs.

This issue can be overcome using a UV-curing based imprint technique, i.e. step-and-flash-imprint-lithography (SFIL). The most interesting type is the reverse tone process, that minimizes defects due to uneven substrates. The mask selectivity for subsequent etching is increased by using a stack of silicon containing and non-silicon containing material (that have to be etched by a halogen etch and an oxygen plasma etch, respectively). The process flow for the imprint and polymer etch process is depicted in Fig. 3. In order to maintain the dimensions and to provide a batch-to-batch reproducibility, it is however crucial that the etching steps are tuned with high precision.[3]
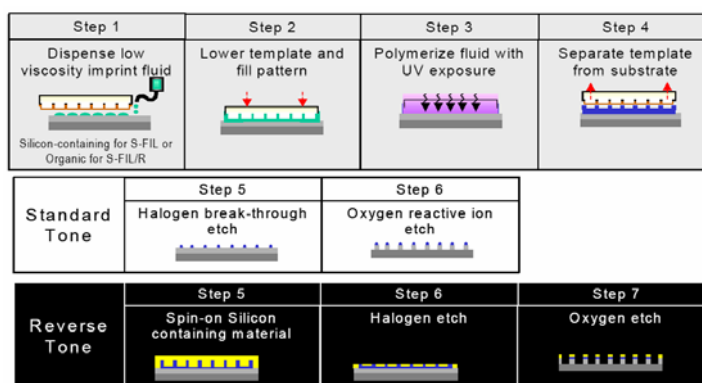
Fig. 3 Process flow for the standard tone and reverse tone SFIL[TM] process (taken from the Molecular Imprints Inc. manual)

During the present PhD, the potential of this technique was shortly assessed through some preliminary experiments. After a short determination of the etch rates for the polymers, the patterns were easily generated on the substrate (see Fig. 4). The underetch was kept to a minimum by optimizing the etching parameters (see Fig. 4 c). For detection purposes, the pillars in a chromatographic application should have a height of at least a couple of μm. To accomplish this, the polymer itself is not sufficient as a mask and an additional mask with a higher etch selectivity should be used. This can be for example a SiO_2 layer, as is the case in
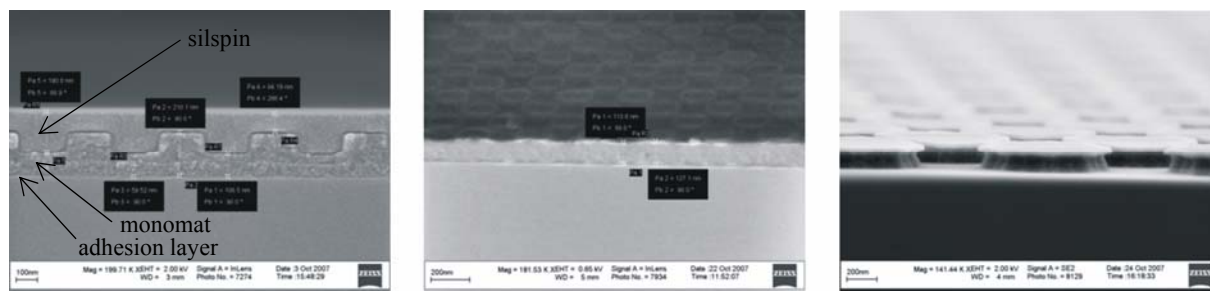
Fig. 4 Some intermediate states in the imprint and polymer etch process. **a)** A layer of silspin polymer is spin-coated on top of the imprinted monomat polymer material **b)** The silspin is etched away with a halogen etch until it is completely removed at the top of the features **c)** An oxygen etch removes the monomat and the underlying adhesion layer between the features, so that the substrate surface is exposed for subsequent etching.

Fig 5. In Fig 5b, the underlying silicon is also etched using a Bosch process with small cycles and using an optimized process to minimize the underetch. The feature depth that can be achieved with such an oxide layer (in this case of 100 nm thickness) is at least 5 μm (see Fig 6a), which is sufficient to provide the necessary sensitivity.
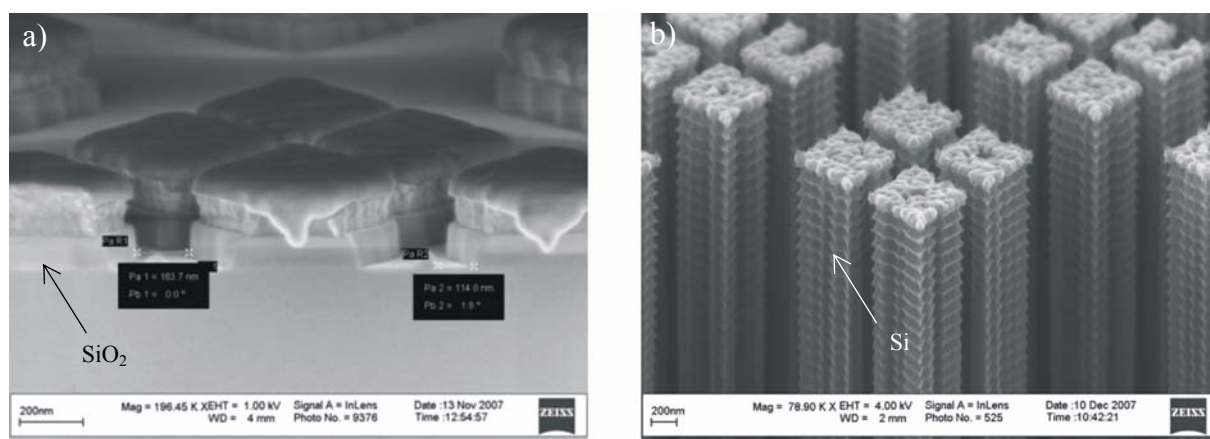

Fig. 5 a) The underlying oxide layer is etched through until the silicon surface. The smallest distance between two pillars is on the order of 100-150 nm **b)** The silicon is Bosch® etched

One of the interesting aspects of decreasing the pillar sizes is that also the surface in the channel becomes larger. If no fabrication limits would exist, the ideal column format would replace the 10 nm mesopores of the porous particles used by 5 or 10 nm pillars. The analogue of the particle would then be a cluster of pillars and the flow in the channel would occur in between these clusters. Looking at Fig. 6 b, an interesting limitation of this idea arises because of the so-called RIE-lag.[4] This loading-dependent etching effect occurs when the areas to be etched vary strongly, giving rise to serious differences in etch-rates. This effect will be detrimental for the quality of the separation, as the top area of the clusters presents a higher surface and will withhold the analytes more strongly than the bottom area. This will give rise to a strong C-term influence in the band broadening. A possible solution for this

issue could be the use of an etch-stop, that can be created by having a material (such as SiO_2 as in a silicon-on-insulator system), so that the etching stops at the interface.
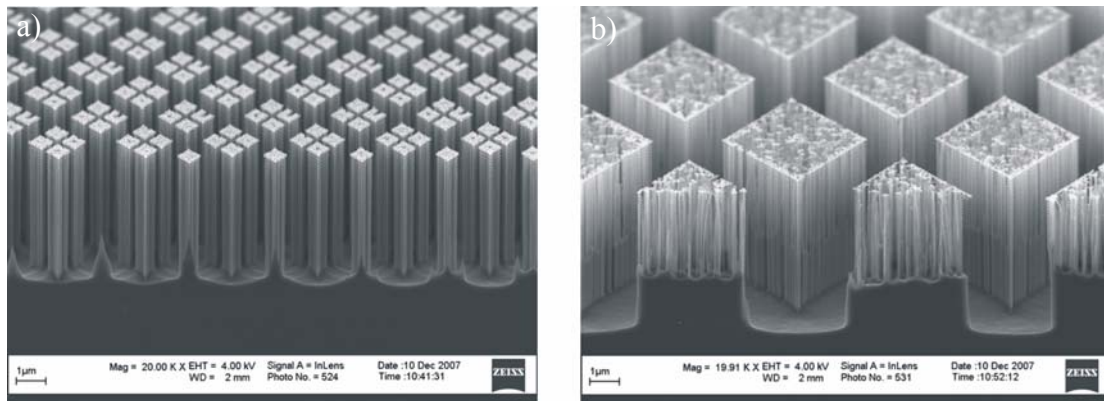
Fig. 6 a) A zoom-out of Fig. 5b. The pillars are about 5 μm high. **b)** A design with 30 % closer positioned pillars than in Fig 5b. The depth of the gaps in between the pillars is considerably smaller as between the pillar clusters due to a RIE-lag effect.

8.2.2 Deep-UV Lithography

Even though the SFIL technology is very promising, it is, due to its contact nature, prone to wafer scale defects. When even in a small part of the channel the slightest defect occurs, a tiny passing plug will lose its consistency. It is of course possible to inspect the fabricated devices and reject those that do not meet a certain defect-level criterion. This then becomes an issue of a more economical nature, and then perhaps the (very expensive) deep-UV technology could also play an interesting role. Not only are the defect levels lower, the throughput is also considerably higher. To investigate this, a number of channels with varying dimension were fabricated by Deniz Tezcan under supervision of Piet De Moor at Imec in Belgium. Figure 7 depicts a channel filled with 5 μm pillars with a side-wall zone distance of about 825 nm.[5]
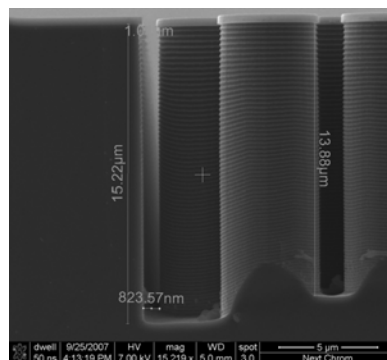
Fig. 7 Side-wall region of an etched pillar array. On top of the pillar the SiO_2 layer that functioned as a hard mask is still visible. A deep-UV lithography stepper (λ=193 nm) was used to define the pillars in photoresist, exposing the SiO_2 for subsequent etching.

On the lithography mask this so called 'magical distance' was set as 750 nm that was found in the literature and that was obtained by the authors using computational fluid dynamics (CFD). The final value after etching was slightly larger due to the underetch of the Bosch® process. In previously performed experiments on chips with equally sized pillars but large deviations of this magical distance (on the order of 0.5 μm), plate heights monitored with the sidewall-zone included were typically a factor of 10 larger than the plate height determined in the central part of the channel. The same kind of experiment was then performed on the deep-UV channels. A van Deemter curve established with the dye C440 dissolved in methanol is depicted in Fig 8.
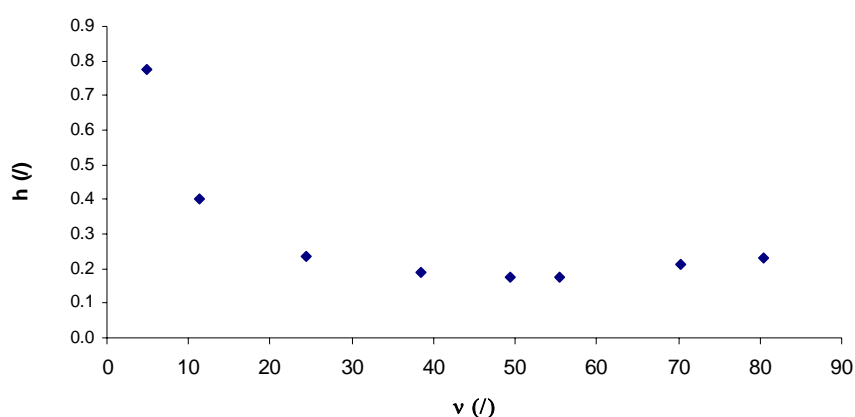
Fig. 8 A van Deemter curve established in the array depicted in Fig 7 with coumarin C440 in methanol in reduced coordinates. The channel width was 150 μm and the band broadening was monitored over the entire width of the channel.

The minimal plate height h is about 0.2, which is equal to what was predicted via CFD simulations for a sidewall-less system in 12 μm deep channels with the same pillar width and bed porosity.[6] Furthermore, no defects were observed in these channels. In Fig 7, the gap depth is slightly different but it does not compromise the band dispersion behaviour for this gap depth. The slight deviation of the magical distance is probably even balanced by this effect in this channel. For smaller pillars however, strategies similar to those discussed in section 8.2.1 should be considered. It should also be noted that under retentive conditions, the magical distance will no longer be valid. This is because a peak is influenced not only by the fluidic field lines but also by the retention and hence the available surface. This implies that a compromise distance will have to be selected to minimize the overall dispersion among the different analytes in a sample.

8.2.3 High pressure chip connections

As is explained in section 8.1, even when only 60 bar is applied to generate a mobile phase flow in the pillar array, benefits already occur compared to packed beds when using the appropriate column length. When seeking the performance limits, an increase in pressure would theoretically be even more beneficial. The mechanical stability of the (porous) pillars could present an important limitation. Very little research has been carried out on high-pressure couplings with respect to chips, but some interesting results were obtained very recently by Tiggelaar et al. By isotropically etching a groove at the side of a glass chip, fibres were inserted and fixed by applying an epoxy glue. The chips could withstand pressures up to 690 bar, depending on the glass type, the bonding method and the shape of the zone where the capillary is inserted.
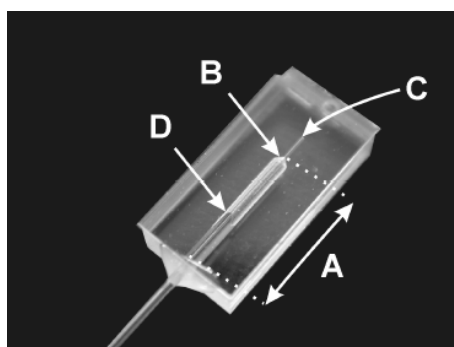
Fig 9. Glass chip to examine the maximum working pressure: A inlet/outlet geometry, B transition area towards microchannel, C microchannel, D glue front (meniscus).[7]

To avoid the use of glue, soldering can also be an interesting technique.[7-8] Trachsel et al. evaporated metallic layers on a silicon substrate in order to provide a wettable surface for the metallic solder, allowing operating conditions of with a temperature of 80 °C and a pressure of 140 bar.[9] When increasing the pressure from 60 bar to 400 bar in the pillar array, a factor of 10 in separation speed can be gained (compare the black curves with the green curves in Fig. 2). These emerging techniques have a great potential to be used in LC on-a-chip.

References

1. Vervoort, N.; Billen, J.; Gzil, P.; Baron, G.V.; Desmet, G. Anal. Chem. **2004**, *76*, 4501-4507.
2. Hattori, W.; Someya, H.; Baba, M.; Kawaura, H. *J. Chromatogr. A* **2004**, *1051*, 141–146.
3. C.M.S. Torres, *Alternative Lithography-Unleashing the Potentials of Nanotechnology*, Kluwer Academic, New York.

4.   M. Elwenspoek and H. Jansen, *Silicon Micromachining*, University Press, Cambridge, 1998.

5.   Tezcan, D.S., Verbist, A., De Malsche, W., Vangelooven, J., Eghbali, H., Clicq, D., Desmet, G., De Moor, P.**,** *Improved Liquid Phase Chromatography Separation using Sub-micron Micromachining Technology*, International Electron Devices Meeting (IEDM), *IEEE International* **2007**, Washington pp. 839-842, December 10-12, United States.

6.   De Smet, J.; Gzil, P.; Baron, G.V.; Desmet,G. *J. Chromatogr. A*, **2007**, *1154*, 189-197.

7.   Tiggelaar, R.M; ., Benito-López, F.; Hermes, D.C.; Rathgen, H.; Egberink , R.J.M.; Mugele, F.G.; Reinhoudt, D.N., van den Berg, A.; Verboom, W.; Gardeniers, J.G.E. *Chemical Engineering Journal* **2007**, *131*, 163–170.

8.   Benito López, Fernando High Pressure: a Challenge for Lab-on-a-Chip Technology, Ph.D. thesis, University of Twente, Enschede, The Netherlands ISBN 978-90-365-2482-7.

9.   Trachsel, F.; Hutter, C.; von Rohr, P.R. Chemical Engineering Journal **2008**, *135*, 309-316.

Publications

Journals with peer reviewing

De Malsche, W., Clicq, D., Eghbali, H., Fekete, V. Gardeniers, H. and Desmet, G. (2006), *An Automated Injection System for Sub-micron Sized Channels Used in Shear-driven-chromatography*, Lab Chip, 6, pp. 1322-1327

De Malsche, W., Eghbali, H., Clicq, D., Vangelooven, J., Gardeniers, H. and Desmet, G (2007), *Pressure-Driven Reverse-Phase Liquid Chromatography Separations in Ordered Nonporous Pillar Array Columns*, Anal. Chem., 79, pp. 5915-5926

De Malsche, W., Clicq, D., Verdoold, V., Gzil, P., Desmet, G. and Gardeniers, H. (2007), *Integration of Porous Layers in Ordered Pillars for Liquid Chromatography*, Lab Chip, 7, pp. 1705-1711

De Malsche, W., Gardeniers, H., Desmet, G. (2008), *Experimental Study of Porous Silicon Shell Pillars under Retentive Conditions. *, Anal. Chem., accepted for publication

Eghbali, H., De Malsche, W., De Smet, J., Billen, J., De Pra, M., Kok, W.T., Schoenmakers, P.J., Gardeniers, H. and Desmet, G**.** (2007)**,** *Experimental investigation of the band broadening originating from the top and bottom walls in micromachined nonporous pillar array columns*, Journal of Separation Science, 30, pp. 2605-2613

De Pra , M., De Malsche, W., Desmet , G., Schoenmakers, P.J., Kok , W. T. (2007), *Pillar-structured microchannels for on-chip liquid chromatography: Evaluation of the permeability and separation performance***,** Journal of Separation Science, 60, pp. 1453-1460

Vankrunkelsven, S., Clicq, D., Fekete, V., Cabooter, D., De Malsche, W., Gardeniers J. G. E. and Desmet, G (2006), *Ultra-rapid Separation of an Angiotensin Mixture in Nanochannels using Shear-driven Chromatography*, Journal of Chromatography A, 1102, pp. 96-103

Fekete, V., Clicq, V., De Malsche, W., Gardeniers, H. and Desmet, G. (2006), *Detection Enhancement For On-Chip Nano-Channel Chromatography*, Journal of Chromatography A, 1130, pp. 151-157

Fekete, V., Clicq, D., De Malsche, W., Gardeniers, J.P.G and Desmet, G., *State of the art of shear driven chromatography. Advantages and limitations*, Journal of Chromatography A, 1149, pp.2-11

Fekete, V., Clicq, D., De Malsche, W., Gardeniers, H. and Desmet, G. (2007), *Use of 120 nm-deep Channels for Liquid Chromatographic Separations*, Journal of Chromatography A, accepted for publication

Conference proceedings with peer reviewing

De Malsche, W., Clicq D., Eghbali, D., Vervoort N., Gardeniers H., van den Berg A. and Desmet, G. (2005), *Extending The Functionalities of Shear-Driven Chromatography Nano-Channels Using High Aspect Ratio Etching*, Proceedings of µTAS 2005, Boston, USA, ISBN 0-9743611-1-9, pp. 106-108

De Malsche, W., Eghbali, H., De Smet, J., Gardeniers, H., and Desmet, G. (2006), *An Optical Injection System Used for Optimalization Studies of High Aspect Ratio LC Pillar Array Columns*, Proceedings of µTAS 2006, Tokyo, Japan. ISBN 4-9903269-0-3-C3043, pp. 564-566

De Malsche, W., Eghbali, H., Clicq, D., Vangelooven, J., Tezcan, D., De Moor, P., Verdoold, V., Gardeniers, H. and Desmet, G. (2007), *Use of Micro- and Nanofabricated Pillar Arrays for Pressure-Driven Reversed Phase Liquid Chromatography Separations*, Proceedings of µTAS 2007, Paris, France, ISBN 978-0-9798064-0-7, October 7-12, pp. 248-251

Eghbali, H., De Malsche, W., Clicq, D., Vangelooven, J., Gardeniers, H. and Desmet, G. (2007), *High performance reversed-phase separations using micro-fabricated columns with perfectly ordered support structures,* HPLC conference, Gent, Belgium

Fekete, V., Clicq, D., De Malsche,W., Gardeniers, H. and Desmet, G. (2006), *Detection enhancement for on-chip nano-channel chromatography.* International symposium of Hyphenated Techniques in Chromatography and Hyphenated Chromatographic Analyzers & Eight International Symposium on Advances in Extraction Techniques , pp. 63-63. HTC. Royal Society of Chemistry. ISBN 90-74870-08-2, February 8-10, York, UK

Vangelooven, J, De Malsche, W., Pappaert, K., Clicq, D., Gardeniers, H. and Desmet, G. (2007), *High Speed Shear-Driven Flows Through Micro-structured 1D-nanochannels*, Proceedings of µTAS 2007, ISBN 978-0-9798064-0-7, pp. 383-385, Paris, France

Detobel, F., Fekete, V., De Malsche, W., Gardeniers, H. and Desmet, G. (2007), Fast Shear-driven Oligonucleaotide Separation in 1D-nanochannels (2007), Proceedings of µTAS 2007, ISBN 978-0-9798064-0-7, pp 1414-1416, Paris, France

Verdoold, V., De Malsche, W., Desmet, G and Gardeniers, H. (2007), Fabrication of Microchannels with Porous Silicon Pillars for On-chip Liquid Chromatography and Microreactors, Proceedings of µTAS 2007, ISBN 978-0-9798064-0-7, pp. 1646-1648, Paris, France

Tezcan, D.S., Verbist, A., De Malsche, W., Vangelooven, J., Eghbali, H., Clicq, D., Desmet, G., De Moor, P. (2007), *Improved Liquid Phase Chromatography Separation using Sub-micron Micromachining Technology*, International Electron Devices Meeting (IEDM), IEEE International, Washington pp. 839-842, December 10-12, United States

Presentations

De Malsche, W., Eghbali, H., Vangelooven, J., Clicq, D., Gardeniers, H. and Desmet, G. (2007), *Microfabricated Porous and Non-Porous Pillar Arrays to Boost the Efficiency and Separation Speed of HPLC*, International Symposium on Capillary Chromatography and Electrophoresis (ISCCE), November 28-30, Albuquerque, United States

De Malsche, W., Mogensen, K.B., Desmet, G., Gardeniers, H. and Kutter J.P. (2008), *Pressure-driven Reversed-phase Chromatography in Microstructured Pillars with UV-VIS Absorbance Detection Using Microfabricated Waveguides*, Symposium on Microscale Bioseparations (MSB), March 9-13, Berlin, Germany

De Pra, M., De Malsche, W., Kok, W.T., Schoenmakers, P.J. (2006), *Pressure Driven Separations in Pillar-Structured Microchannels,* International Symposium on Capillary Chromatography and Electrophoresis (ISCCE), May 29-June 2, Riva del Garda, Italy

De Malsche, W., Mogensen, K.B., Desmet, G., Gardeniers, H. and Kutter J.P. (2008), *Pressure-driven Reversed-phase Chromatography in Microstructured Pillars with UV-VIS Absorbance Detection Using Microfabricated Waveguides*, HPLC 2008, May 10-16, Baltimore, United States

Desmet, G., S. Vankrunkelsven, V. Fekete, F. Detobel, D. Cabooter, W. De Malsche, H. Gardeniers and David Clicq, Miniaturization of Analytical Separations using the Shear-Driven Flow Principle: Challenges and Opportunities, International Symposium on High Performance Liquid Phase Separations and Related techniques (HPLC 2005), June 26-30 2005, Stockholm, Sweden (invited keynote lecture)

De Pra, M., De Malsche, W., Kok, W.T., Schoenmakers, P. J., Desmet, G. (2006), *Pressure driven separations in channels structured with micropillars*, Symposium on Microscale Bioseparations (MSB), March 22-26, Amsterdam, The Netherlands

Desmet, G., De Malsche, W., Eghbali, H., Vangelooven, J., Clicq, D. and Gardeniers, H. (2006), *Shifting the Performance Barriers of HPLC Using Micro-fabricated Chromatographic Columns*, NanoTech-Annual European Conference on Micro & Nanoscale Technologies for the Biosciences, September 14-16, Montreux, Switzerland (invited closing lecture)

G. Desmet, W. De Malsche, H. Eghbali, J. Vangelooven, H. Gardeniers and D. Clicq (2008), Liquid Phase Chromatography Separations in Micro- and Nano-pillar Columns (2008), 22nd International Symposium on Microscale Bioseparations (MSB 2008), March 9-13, 2008, Berlin, Germany (invited plenary lecture)

Eghbali, H., De Malsche, W., Vangelooven, J., Clicq, D., Gardeniers, H. and Desmet, G. (2007), *Using Microfabricated Perfectly Ordered Pillar Array columns as an Alternative for the Conventional Packed Bed in HPLC*, NanoTech-Annual European Conference on Micro & Nanoscale Technologies for the Biosciences, November 14-16, Montreux, Switzerland

Tezcan, D.S., Verbist, A., De Malsche, W., Vangelooven, J., Eghbali, H., Clicq, D., Desmet, G., De Moor, P. (2007*), Improved Liquid Phase Chromatography Separation using Sub-*

micron Micromachining Technology, International Electron Devices Meeting (IEDM), IEEE International, Washington pp. 839-842, December 10-12, United States.

Clicq, D., Vangelooven, J., De Malsche, W., Gardeniers, H. and Desmet, G. (2007), Shear-driven Flows through Nano-channels Uniformly Packed with a Micro-structured Pillar Region, SPIE conference, August, 26-31, San Diego, United States.

Vangelooven, J., De Malsche, W., Eghbali, H., Sabuncuoglu Tezcan, D., De Moor, P., Verbist, A., Clicq, D. and Desmet, G.. Improved liquid phase chromatography separation using sub-micron micromachining technology. HTC, Januari 2008, Bruges, Belgium.

Summary

High-performance liquid chromatography (HPLC) is one of the most versatile separation techniques available for the analysis of complex samples that are typically encountered in fields such as environmental monitoring, biology, pharmacy, biochemistry, etc. A distinction between different HPLC formats can occur in the shape of the stationary phase, which necessarily displays a selective interaction with the present analytes in order to establish a separation. The most prevailing format is the packed particulate bed, which generally consists of functionalized porous spherical particles that are randomly packed in a capillary. Monolithic media (polymeric or silica) have recently become popular because of the high permeability combined with reasonable mass transfer characteristics. In this frame it is important to stress that it is theoretically expected that disorder restrains the performance of a column. When conceiving the ideal chromatographic format, the achievement of more order is therefore an interesting route to pursue. A practical realization of this approach was first put forward in 1998 by prof. Fred Regnier, making use of a microfabricated array of pillars in glass in capillary electro-chromatography mode, replacing the random particles by very accurately positioned pillars. Recognizing the potential of the technique, Desmet and co-workers performed a number of computational fluid dynamics (CFD) to study the fluidic behaviour of such a pillar array in pressure-driven mode. As the flow-through pores can be chosen independently of the pillar diameter, optimal designs can be tailored to provide the optimal combination of flow resistance and plate height. A first device containing non-porous silicon pillars was then characterized by De Pra et al. in 2005 under non-retaining conditions, achieving a minimal reduced plate height of 0.2 in a 40 % porosity pillar bed consisting of 10 µm pillars, in agreement with the CFD predictions. Even though this work was an important trigger in generating interest in this novel format, no separations were demonstrated, hence keeping the more relevant fluidic behaviour under retentive conditions in the dark.

In the present thesis, microfabrication technologies have been employed to solve a number of stringent issues in liquid chromatography. In the first part of this thesis (chapter 3), an automated injection system was developed for shear-driven chromatography (SDC). This chromatographic technique was proposed by Desmet and co-workers in 1999 and is based on the use of two axially sliding flat substrates. As the average velocity is independent of the channel dimensions (i.e. half the velocity of the moving substrate), pressure drop limitations are no longer relevant. The developed injection system allowed for controlled and reproducible injections in a 300 nm deep SDC channel (6 % relative standard deviation for the peak area). With this developed injection system, a lower limit for the injected peak width of 120 µm was established. This limit could be qualitatively predicted and explained as a consequence of diffusion during the finite duration of the filling and flushing steps in the injection procedure.

The second part of this thesis concerns the development of a pillar array prototype. First, non-porous silicon pillar arrays have been studied (chapter 4). For this purpose, non-porous pillars with an external porosity of 55 % and a diameter a 4.3 µm were coated with a C8 phase. This yielded minimal plate heights of H_{min}=4 µm (or about h_{min}=1 in reduced coordinates) at a retention value of k'=1.2, when excluding the side-wall region and following a coumarin plug in the central part of the channel using a fluorescence microscope. The separation impedance of the array appeared to be as small as 150, i.e. on the same order as the best currently existing monoliths. Next, a waveguide was integrated to allow for in-situ UV-Vis detection in a (non-porous) SiO_2 pillar array channel (chapter 5). A van Deemter curve for thiourea in methanol was established in absorbance-mode in a channel with inter-pillar distances of the

order of 2 μm, yielding a minimal plate height of 15 μm. Analysing dispersion in different zones of the channel in fluorescence mode with a CCD camera using a coumarin in methanol, the unexpectedly large dispersion appeared to have a double cause, originating from the strong taper of the pillars as well as from sidewall effects.

To provide these non-porous pillars with specific surface levels as typically available in HPLC, a fabrication scheme was developed that enabled to create porous shells on highly doped p-type silicon pillars having a diameter of 10 μm (chapter 6). This closed channel configuration was tested up to 70 bar without observing leakages or losses in consistency. The homogeneity of these layers was confirmed by optical microscopy pictures from one hand and by following moving peaks at constant velocity on the other hand. Monitoring van Deemter curves of pillar arrays with different porous shell thicknesses, minimal reduced plate heights of about 0.5 were obtained under non-retaining conditions. The obtained results were in excellent agreement with Giddings' non-equilibrium theory. Coating these layers with a C8 phase, an enormous increase in retention behaviour was observed. The minimal plate heights using a 1 μm porous layer and a retention coefficient as high as k'=12 was only h_{min}= 0.9, whereas the increase in k' value was 260 times as compared to the non-porous pillar array. Using the same model parameters as found in the non-coated system, the predicted h values obtained when inserting the appropriate retention coefficients and shape factors qualitatively comply with the model.

Interpreting these results in a more general framework, the future of the pillar array column concept seems bright. It appears that it should be possible to reduce the analysis time to achieve a given number of plates (using an identical pressure limitation) by at least a factor of 10, when comparing the pillar array with the packed bed (chapter 8). A potential bottleneck could be the high-pressure connection between the pump and the chip.

Samenvatting

Vloeistofchromatografie is een van de meest veelzijdige scheidingstechnieken die momenteel voorhanden is voor de analyse van complexe mengsels die typisch worden aangetroffen in velden als milieuwetenschappen, biologie, farmacie, biochemie.

Een onderscheid tussen verschillende *formats* van vloeistofchromatografie kan gebeuren op basis van de vorm van de stationaire fase, die noodzakelijkerwijs een selectieve interactie met de aanwezige analyten moet vertonen om een scheiding te verwezenlijken.

Het meest voorkomende *format* is het gepakte bed, dat is opgebouwd uit gefunctionaliseerde poreuze sferische partikels die willekeurig in een capillair gepakt zijn.

Monolitische media (polymerisch of uit silica) zijn recent populair geworden vanwege de hoge permeabiliteit van deze kolommen, gepaard gaande met vrij goede massaoverdrachtseigenschappen. In dit kader is het van belang te vermelden dat theoretisch voorspeld wordt dat de wanorde van deze systemen de performantie limiteren. Bij het concipiëren van een ideaal chromatografiesysteem is het nastreven van orde dan ook een interessante denkpiste. De eerste praktische benadering van deze aanpak werd voorgesteld in 1998 door Prof. Fred Regnier (Perdue University) die de partikels verving door een microgefabriceerde reeks van glazen paaltjes die zeer nauwkeurig gepositioneerd waren.

In het aldus gevormde pillarenbed werd dan aan capillaire electrochromatografie gedaan. Geïnspireerd door deze resulaten deden Prof. Gert Desmet (Vrije Universiteit Brussel) en medewerkers daaropvolgend een reeks vloeistofsimulaties om het fluidisch gedrag in de paaltjeskolom te bestuderen in drukgedreven mobiele fase aansturing.

Doordat de dimensies van de doorstroomporiën nu onafhankelijk gekozen kunnen worden van de paaltjesdiameter, konden deze karakteristieke dimensies nu zo gekozen worden dat een ideale combinatie van stromingsweerstand en plaathoogte bereikt werd.

De eerste experimentele resultaten van een drukgedreven stroming in een niet-poreuze paaltjeskolom werden voorgesteld door De Pra et al. (Universiteit van Amsterdam) in 2005.

Gereduceerde plaathoogtes van h=0.2 bij niet-geretenteerde condities werden aangetoond in een 40 % poreus bed opgebouwd uit paaltjes met een diameter van 10 µm, wat in overeenstemming was met de simulaties van Desmet et al. Dit werk heeft veel interesse opgewekt voor de paaltjeskolom, maar er werd alleen gewerkt bij niet-geretenteerde condities waardoor het belangrijkere aspect van retentie volledig onbelicht bleef.

In deze scriptie worden microfabricatietechnologieën aangewend om een aantal dwingende vragen in de vloeistofchromatografie te behandelen en op te lossen.

In het eerste gedeelte van deze scriptie (hoofdstuk 3) werd een automatisch injectiesysteem ontwikkeld voor schuifkrachtgedreven chromatografie (SGC). Deze chromatografische techniek werd in 1999 ontwikkeld door Desmet et al. en is gebaseerd op het gebruik van 2 axiaal schuivende vlakke substraten.

Doordat de gemiddelde snelheid onafhankelijk is van de dimensies van het aldus gevormde kanaal, zijn er geen limitaties meer betreffende de aan te wenden druk. Het ontwikkelde injectiesysteem liet een gecontroleerde en reproduceerbare injectie toe in een 300 nm diep SGC-kanaal (6 % relatieve standaardafwijking op het piekoppervlak). De breedte van de geïnjecteerde pieken had een ondergrens van 120 µm. Deze limiet kon kwalitatief voorspeld en gerationaliseerd worden aan de hand van diffusie gedurende de eindige duur van de vul- en spoelstap van de injectieprocedure.

Het tweede gedeelte van deze scriptie betreft de ontwikkeling van een paaltjeskolom prototype. Eerst werd een niet-poreuze paaltjeskolom bestaande uit silicium bestudeerd (hoofdstuk 4).

Hiertoe werden paaltjes met een diameter van 4.3 μm en een externe porositeit van 55 % geproduceerd door droog etsen en nadien gefunctionaliseerd met een C8-fase. De laagste opgemeten plaathoogtes bedroegen H_{min}=4 μm (of ongeveer h_{min}=1 in gereduceerde coördinaten) bij een retentiecoëfficient k'=1.2, waarbij een coumarine werd gevolgd door middel van een fluorescentiemicroscoop bij een constante bewegingssnelheid en waarbij de zijwandzone niet in rekening werd gebracht. De scheidingsimpedantie was ongeveer E=150, wat van dezelfde orde is als de best presterende monolieten.

Vervolgens werd een lichtgeleider geïntegreerd om met UV-Vis absorptie te kunnen decteren, waarbij de (niet-poreuze) paaltjes uit SiO_2 waren vervaardigd (hoofdstuk 5). Een van Deemter curve voor thiourea in methanol werd opgemeten in absorptiemode in een kanaal met interpillaar afstanden van ongeveer 2 μm, waarbij minimale plaathoogtes van H_{min}=15 μm werden opgemeten.

Door ook met de CCD camera en de fluorescentiemicroscoop de dispersie te bekijken in enerzijds het centrale gedeelte van het pillarenbed en anderzijds de zijwandzone, bleek de hoge H_{min}-waarde een tweeledige oorsprong te hebben. Zowel de niet-verticaliteit van de paaltjes (*taper*) als een verschil in stromingsweerstand tussen de zijwandzone en het centrale gedeelte van het bed bleken een belangrijke bijdrage in de plaathoogte te leveren.

Deze niet-poreuze paaltjes hebben een lage specifieke oppervlakte vergeleken met de poreuze partikels uit de klassieke gepakte bedden. Omdat voor typische scheidingen hogere specifieke oppervlakken nodig zijn, werd een processchema ontwikkeld om poreuze lagen te genereren door anodisatie van hoog gedopeerd p-type Si met als dragerstructuren paaltjes van 10 μm diameter (hoofdstuk 6). Deze poreuze structuren werden geproduceerd in een gesloten kanaal-configuratie, waarbij geen lekken of verlies in consistentie werd waargenomen tot de geteste drukwaarde van 70 bar. De homogeniteit van deze lagen werd bevestigd door optische microscoopfoto's enerzijds en door geïnjecteerde pieken te volgen bij een constante bewegingssnelheid anderzijds. Van Deemter curves opgemeten bij niet-geretenteerde condities in paaltjeskolommen met verschillende laagdiktes vertoonden een minimum beneden h_{min}=0.5 (laagdikte 1.4 μm).

Deze resultaten waren in goede overeenstemming met Giddings' onevenwichtstheorie.

Vervolgens werden deze poreuze lagen gefunctionaliseerd met een C8-fase, wat een enorme toename aan retentiecapaciteit opleverde.

De minimale plaathoogte die werd opgemeten bij een 1 μm poreuze laag en een retentiecoefficiënt van k'=12 was slechts h_{min}=0.9.

De k'-waarde van deze poreuze paaltjeskolom, vergeleken met een niet-poreuze paaltjeskolom, was 260 maal toegenomen.

Via de gevonden modelparameters uit het niet-gefunctionaliseerde systeem konden ook de plaathoogtes van de retenterende lagen kwalitatief voorspeld worden door de retentie- en vormfactoren in rekening te brengen.

Deze resultaten bieden een zeer gunstig toekomstperspectief voor het paaltjeskolomconcept. De vereiste analysetijd om een bepaald aantal platen te genereren (bij een identieke limitatie op de opgelegde druk aan de inlaat) kan een factor 10 lager liggen voor het paaltjesbed dan voor het gepakte bed (hoofdstuk 8). De vereiste hogedrukverbinding met de chip kan evenwel nog een mogelijk knelpunt zijn.

Acknowledgements

Als je aan een doctoraat begint, kan je maar beter een goede promotor hebben. Ik had het geluk er zo twee te hebben.

De eerste twee jaren van mijn onderzoek heb ik grotendeels doorgebracht in Enschede, waar Han mijn begeleider was. Door zijn Zuid-Nederlandse mentaliteit kon ik het meteen met hem vinden. Als expert in microtechnologie en chemie heeft hij me zeer veel bijgebracht over de lab-on-a-chip wereld. Zijn aanstekelijk enthousiasme zorgde er soms voor dat ik er geen idee meer van had wanneer de kantooruren begonnen of eindigden. Om als promovendus interessant onderzoek te doen, heb je vrijheid nodig om nieuwe ideeën uit te werken, en hiervoor ben ik Han heel dankbaar. Wat ik evenzeer waardeer, is dat hij me -wanneer nodig- terug naar de orde van de dag bracht zonder veel omwegen en me dan met weinig woorden zei hoe het nu eigenlijk echt in elkaar zat.

De laatste twee jaar bracht ik veel tijd door in Brussel, waar ik op Gert kon rekenen. Toen ik met mijn eerste chips naar Brussel kwam en de eerste scheidingen werden verwezenlijkt, was zijn enthousiasme niet te stoppen. Gert heeft me toen ingewijd in vele (veelal ongepubliceerde) aspecten van de chromatografie, wat een nieuwe wereld voor me opende. Het gemak waarmee Gert formules uit de losse pols tovert, is hallucinant. Maar ook op vele andere terreinen was hij een schitterende begeleider.

Ik wil beide heren promotoren hartelijk bedanken voor de fijne en leerrijke voorbije vier jaar.

Toen ik aan mijn promotie begon, was dit nog bij Bios, waar excentrieke figuren als Jurjen, Egbert, Jan Eijkel, Séverine, Albert, Ton, Ad, Ana en Patrick heel wat leven in de brouwerij brachten, zowel op de universiteit als op de internationale congressen. Jan Eijkel bedank ik in het bijzonder voor de boeiende wetenschappelijke discussies en input. Ook de rest van de groep dank ik voor de mooie tijd.

Jan van Nieuwkasteele en Johan Bomer hebben me mijn eerste passen in de cleanroom leren zetten. Zonder Johan had dit proefschrift er heel anders uitgezien. Ook Ton, Daniël, Arjen, Victor, Selm, Vincent, Roald, Jacob en vele anderen droegen ertoe bij dat het een gezellige bende was in de cleanroom, ze maakten de lucht er iets minder droog. Dat brengt me dan bij de heren en dames van de cleanroom staff. Ik wil hen bedanken voor de goed geoliede cleanroom. Zonder hun zorgen had ik dit doctoraat nooit kunnen verwezenlijken. Sorry dat ik af en toe op een verkeerd knopje drukte.

During some of the nano-imprint activities I had the opportunity to work with Boris Vratzov. He taught me many secrets of the nano-world, for which I am very indebted to him. Also outside of the cleanroom he's a nice guy, I enjoyed particularly the many lunches we had together. I hope our cooperation will not end at this point.

Het laatste jaar van mijn doctoraat is Han zijn eigen groep begonnen en zijn we met een tiental personen overgegaan naar de nieuwe Mesoscale Chemical Systems (MCS) groep. Deze kleine groep was een sterk team, zowel binnen als buiten de kantooruren. Han zou Vigor Wuitens Hamme zo Belgisch landskampioen kunnen maken. Ik vermoed dat de balans van de Faculty Club serieus uit evenwicht is sinds MCS werd opgericht. I would like to thank Jacqueline, Regina, Han, Stefan, Anil, Jacob, Selm, Wojtek, Nikolay, Maciek, David, Kevin, Sertan, Vincent, Roald, Manon, Elizaveta and Dawid for the great time and atmosphere.

A substantial part of my stay in Enschede I spent in the bar 'Jansen and Jansen'. There was one particular person that knew what would follow if I sent a text message saying 'Quedamos en el Jansen?'. She would pick up her jacket and some time later we would be drinking 'Grimbergen van het vat' at a high pace. Ana, thanks a lot for everything! I hope we keep in touch. I wish you good luck in Lausanne and at your future destinations.

Een aanzienlijk deel van de laatste twee jaar van het onderzoek gebeurde op de VUB in Brussel. Het goede verloop van de experimenten was in grote mate te danken aan David, die met zijn programmeerkunsten zowat alles kon automatiseren waar ik alleen maar van kon dromen. Ook Piotr, Hamed, Joris, Selm en Kris hebben bijgedragen aan de experimenten en de wetenschappelijke discussies, waarvoor dank. Ook Mark en Tom speelden een belangrijke rol in het verzamelen en fabriceren van de verschillende opstellingen. Hamed was ongeveer de enige die dapper genoeg was om telkens weer mee te gaan lunchen in het nogal marginale 'La Terasse' in Etterbeek. Ook mijn buddy's Eileen en Adinda zorgden voor de nodige verstrooiing buiten de labo's. Piotr was inspirerend zowel binnen als buiten de wereld van de chromatografie. Ik wens de hele groep in zijn geheel te bedanken voor de aangename tijd.

Part of my work occurred in cooperation with Piet De Moor and Deniz Tezcan from Imec Institute in Belgium, which led to a smoothly running and very successful cooperation. I thank both of them for the given trust and the efforts. I hope our cooperation will last longer and I am confident that our future plans will be successful.

I also want to express my gratitude to Mauro De Pra from the Vrije Universiteit of Amsterdam for the interesting collaboration we had during the first year of my PhD work.

I had the opportunity to spend two months in the lab of Prof. Kutter at the Technical University of Denmark. I am very indebted to Prof. Kutter for this opportunity. This was one of the scientific and social highlights of my PhD. I had the unique chance to be personally instructed by Klaus Mogensen, who did pioneering work on integrated detection systems on-a-chip and learned me everything I wanted to know but was too afraid to ask. Also Detlef's help in bringing my setup to work is greatly appreciated. In my free time there was Massimo and Pedro, who very much appreciated an efficient text message with the name of a bar and a time. Of course I will never forget about these good times, guys. For sure! Monica, thanks for the good times. I also want to thank the other group members for providing a nice atmosphere.

The last year I shared a house with Wojtek and Selm. This was definitely one of the highlights of my stay in the Netherlands. There was always a lot of activity in the house. In the evenings we often cooked, had a beer, an espresso and then back to work to finish the urgent stuff we had to do. It was all pretty hectic. A vodka (or 2) in the late evening would often close the session of the day. Guys, thanks for providing such a nice living and working environment.

A number of people had no professional involvement but paid a very important contribution to this work by just being themselves, my friends. I would even say that at first sight many of these guys were not really helping me forward with this PhD. I had Vagelis, Tolis, Julio and other malakas that came to delight me with a visit in my flat in Copenhagen, which resulted in me having to find a new apartment the day after. My Belgian ever lasting friends Biegel, Brutus, Puco, Furiose, Ariane and Gert are the best to go out with, but you can forget about working the day after! But these guys refreshed my mind at times when it was really necessary. Otherwise this thesis would not have been written. Highly appreciated! Ook mijn

vriendinnen Annelies en Joyce wil ik even bedanken voor hun aanwezigheid, sorry dat ik zelf meestal niet te bespeuren was.

Mijn familie wil ik bedanken voor de steun en het begrip. Ook mijn schoonfamilie bij wie ik veel tijd (vooral werkend) heb doorgebracht en bij wie de deur steeds open stond, wil ik zeker bedanken. Frederik heeft bovendien voor de schitterende cover gezorgd en dankzij An is het aantal schrijffouten serieus gereduceerd.

Nu we toch in de familiale sfeer beland zijn, wil ik nog even een paar woorden zeggen over mijn moeder, Betsy. Buiten de moederlijke taken die ze vervult, zoals overheerlijke biefstukken bakken, is ze ook nog eens een van mijn beste buddy's. Ik herinner me nog goed dat ik na mijn eerste congres met haar had afgesproken in Boston en dat ze daar vrolijk kwam afgewandeld en zei: 'How are you my son?'. Doorheen de jaren heeft ze me altijd onvoorwaardelijk gesteund en ze was meestal enthousiaster dan ikzelf over de dingen die ik doe.

De laatste en belangrijkste paragraaf van deze thesis wil ik aan Sofie wijden. Ze heeft meer op de Nederlandse treinen gezeten dan de doorsnee Nederlander en is gedurende de laatste jaren zowat een expert geworden in het begrip 'wachten op iemand'. Bedankt Bushki, voor alles! Jij bent het suikerklontje in mijn tasje thee. En nu moet ik er snel vandoor naar mijn liefje.

Wim